High Repetition Rate Temperature and Velocity Imaging in Turbulent Flows using Thermographic Phosphors

Christopher Abram

September 2014

Department of Mechanical Engineering
Imperial College London

Submitted in part fulfilment of the requirements for the degree of Doctor of Philosophy in Mechanical Engineering of Imperial College London and the Diploma of Imperial College London.

I certify that all material in this thesis which is not my own work has been properly acknowledged and referenced.

Christopher Abram

September 2014

The copyright of this thesis rests with the author and is made available under a Creative Commons Attribution Non-Commercial No Derivatives licence. Researchers are free to copy, distribute or transmit the thesis on the condition that they attribute it, that they do not use it for commercial purposes and that they do not alter, transform or build upon it. For any reuse or redistribution, researchers must make clear to others the licence terms of this work.

© Christopher Abram 2014

Abstract

Turbulent flows involving heat transfer and chemical reactions are prevalent in a huge range of applications such as combustors and engines, boilers, and heating and cooling devices. Directly measuring important variables using laser-based techniques has significantly contributed to our understanding of the underlying flow physics. However, many flows of interest exhibit infrequent or oscillatory behaviour, such as flame extinction or instabilities in thermal boundary layers. Capturing the flow dynamics requires simultaneous, two-dimensional temperature and velocity measurements at sampling rates commensurate with turbulent timescales. Typically this means measuring many thousands of temperature and velocity fields per second, yet there are no high repetition rate diagnostics for temperature imaging in practical, oxygen-containing systems, with the essential capability of simultaneous velocity measurements.

This thesis presents a novel laser-based imaging technique based on thermographic phosphor particles. There are a huge variety of thermographic phosphors, which are solid materials with luminescence properties that can be exploited for remote thermometry. Here, phosphor particles are seeded into the flow as a tracer. An appropriate phosphor must be selected, and the particle size chosen so that the particle temperature and velocity rapidly assume that of the surrounding fluid. The particles are probed using high-speed lasers and their luminescence and scattering signals are detected using high-speed cameras to measure the flow temperature and velocity at kHz repetition rates. The development of this method is described in detail. Using the thermographic phosphor BAM:Eu^{2+}, examples of simultaneous time-resolved measurements are presented in turbulent air flows between 300 and 500 K, consisting of a heated jet ($Re \sim 10,000$) and also a flow behind a heated cylinder ($Re \sim 700$). The technique permits kHz-rate temperature imaging in oxygen-containing environments. These combined diagnostics currently provide a unique capability for the investigation of transient, coupled heat and mass transfer phenomena in turbulent flows of practical engineering importance.

A second objective of this work is to improve the precision of the temperature measurement. The characterisation of a different thermographic phosphor with a high temperature sensitivity, zinc oxide (ZnO), is also reported. Temperature imaging using these tracer particles is demonstrated in a jet ($Re \sim 2,000$) heated to 363 K, with a temperature precision of 1%. This extends the capabilities of this versatile technique toward the study of flows with small temperature variations. Also, unlike the majority of phosphors previously investigated for thermometry, this phosphor is a semiconductor. Exploiting the temperature-dependent luminescence of this class of materials presents interesting new opportunities for remote temperature sensing.

Acknowledgements

Thanks to: Frank Beyrau, supervisor of this work, for sharing his limitless enthusiasm for this topic, deep understanding of physics and engineering relevant to laser diagnostics, and professional approach to research; for fostering the fruitful atmosphere of collaboration amongst he, Benoit Fond and I (long may it continue); for the opportunity to work on other exciting projects; and now for the chance to further pursue the development and application of this measurement technique; my examiners, Bruno Renou and Guillermo Rein, for the insightful and inspiring discussion; the Engineering and Physical Sciences Research Council for financial support; all those at college - our group: Johannes Kerl, Thomas Sponfeldner, Sebastian Henkel, Alexandros Charogiannis, Michalis Hadjipanayis, Meor Zulfikli, Alvaro Yañez Gonzalez, Tony Ojo, and Carlos Garcia Gonzalez (for the SEM images !), my fellow researchers in the Thermofluids divison (particularly Nikos Soulopoulos, Georgios Charalampous, Guru Ramaswamy and most especially Fabian Hampp), our secretary Serena Dalrymple, the 362 crew (including Mr. Michael Mace), and the technicians Eddie Benbow, Guljar Singh, and Asanka Munasinghe; family and friends - bless you Jen Morone, for the fun had carefully removing your boisterous & juvenile remarks from this report; new colleagues at LTT, Otto-von-Guericke Universität Magdeburg; Stockwell, home for four years; and Benoit Fond: a brilliant scientist, and a brilliant friend.

Contents

List of Tables

List of Figures

1 Introduction

Optical diagnostic techniques have significantly contributed to our understanding of turbulent fluid flows. Such flows are prevalent in a huge range of applications that use, convert or generate thermal energy, such as combustors and engines, boilers, and heating and cooling devices. Therefore, the development of these experimental methods will continue to be a crucial area of research.

Laser-based imaging techniques have long been at the forefront of this effort since they allow the instantaneous measurement of specific flow variables with a high spatial resolution [1]. Instantaneous two-dimensional measurements covering a range of spatial scales provide fundamental insight into previously unobserved flow structures and gradients. The data provide valuable statistics to validate numerical models [2,3], which are needed to predict flow behaviour and therefore improve the design of devices in which these flows govern performance and safe operation. In fact, much of this vital technology and also many naturally occurring flows are much older than our ability to measure or model them. Applied in existing practical devices, laser-based imaging techniques have improved our basic understanding of their operation, such as the in-cylinder processes in Diesel engines [4].

In 1986 Ron Hanson gave a paper at the Twenty-first International Symposium on Combustion, stating that "progress in the development of flowfield imaging is tightly coupled to advances in laser sources and, particularly, in array detector technology" [5]. Indeed it was these instrumentation developments (and their intelligent application) that expanded diagnostic capabilities from point and line measurements to imaging techniques. However, these techniques are still restricted to low sampling rates of 1-10 Hz, which means that imaging data is temporally uncorrelated for most turbulent flows of practical interest.

Recent advances in high repetition rate laser systems and high-speed cameras have increased sampling rates to the kHz regime and even higher [6–8]. Such measurements are providing unprecedented insight into transient turbulent flow phenomena. Extended time-resolved imaging sequences allows the rapid accumulation of statistics in fast non-stationary processes, and the capture of rare occurrences that might dominate overall system performance such as global extinction and engine misfire. Data extracted from these sequences can be then be conditioned in time (on these specific events) and space (location of the relevant flow feature), to statistically analyse particular flow behaviour. From recording sequences that cover a wide range of turbulent timescales, dominating frequencies of coherent flow structures can be identified, such as those caused by thermoacoustic oscillations. As mentioned previously, it is also important to provide datasets for the validation of new numerical models. Large eddy simulations are established as the most feasible tool for predicting transient behaviour in turbulent flows, and require imaging time-series recorded at high repetition rates (and data derived from these) for comprehensive comparison and validation [9].

The capabilities of time-resolved planar measurements are therefore indispensable. Measured variables would ideally include the velocity, pressure, the degree of mixing, temperature and in the case of combustion, the most critical chemical species. Acquisition of all these quantities is normally not possible, and the experimentalist must rely on a subset of measured variables. Temperature is of fundamental thermodynamic importance, and its measurement is required for all flows involving heat transfer and/or chemical reactions. Velocity measurements are mandatory for the study of the turbulence, and from these quantities such as strain rate and vorticity can be derived which aid in the characterisation of the flow field. An important point is that measurements of either temperature or velocity are extremely useful, but the value of simultaneous measurements cannot be understated and are essential when some coupling mechanism between the fluid temperature and the flow field exists.

For example, the accurate prediction of convective heat transfer relies on the temperature and velocity fluctuations near the surface, and to some degree large-scale buoyant flow structures may be coupled with the boundary layer [10]. In the case of natural convection the flow is actually driven in part by the exchange of warmer, buoyant fluid and colder, denser fluid, caused by small temperature differences within the boundary layer in which interfacial fluid is heated or cooled. Coherent flow motions interact with the boundary layer [11] which locally may be intermittently laminar or turbulent [12]. Density fluctuations can introduce anisotropy in the intensity of velocity fluctuations in jet flows with significant density differences [13]. In the same way, the flow dynamics of turbulent flames may be affected by heat release [3], and due to the extreme sensitivity of reaction rates to temperature, even small temperature differences can dramatically alter the flame behaviour. This interaction between turbulence and chemistry strongly affects ignition and extinction [14], and is of particular significance as these processes can govern the stable operation of devices involving turbulent reacting flows. The ignition and extinction of flames are dynamic phenomena, and flow temperature and velocity fields leading up to and during the event must be measured to understand how these events occur. In fact, in all these examples both simultaneous and time-resolved measurements are of critical importance to identify the relationships between the flow and the temperature field, and how they evolve in time.

This thesis presents the development of a new laser-based measurement technique based on thermographic phosphor particles, which are seeded into fluid flows as a tracer. The particles are probed using lasers and their luminescence and scattering signals are detected using cameras to image the flow temperature and velocity. The basic principle of this technique was validated at low repetition rates in work carried out by our research group at Imperial College since 2010 [15, 16]

The specific objective of this work is the extension and demonstration of the method at kHz repetition rates. Demonstration experiments at a repetition rate of 3 kHz in turbulent air flows between 300 and 500 K, consisting of a heated jet ($Re \sim 10,000$) and also a flow behind a heated cylinder ($Re \sim 700$), show that the technique allows simultaneous time-resolved planar measurements of temperature and velocity in oxygen-containing environments. At the time of writing, the diagnostics provide a unique capability for kHz-rate temperature imaging, permitting the investigation of transient behaviour occurring in a range of turbulent flows of practical engineering importance.

Besides this objective, some of the applications in the preceding discussion involve subtle temperature differences, therefore demanding precise temperature measurements. To meet this aim a different thermographic phosphor with improved temperature sensitivity is identified and characterised, in the temperature range 300 - 500 K. Planar temperature measurements with a precision of 4 K are successfully demonstrated in a turbulent ($Re \sim 2,000$) heated jet of air.

The utility of the basic concept of flow temperature and velocity imaging using phosphor particles is confirmed by these two advances, which significantly extend the range of applications of the technique and provide new possibilities for future development.

2 Temperature and Velocity Imaging Techniques

Remarkable advances in laser measurements have enabled the detection of many different variables, and each technique or combination of techniques has their own advantages and disadvantages. The discussion here is restricted to methods for planar imaging of temperature and velocity to identify current diagnostic capabilities for simultaneous measurement of these variables. The first part of this chapter provides a brief overview of the well-established velocity measurement technique particle image velocimetry (PIV). Time-resolved ('high-speed', sampling rate typically $>$ kHz) PIV and scalar imaging techniques are then reviewed. Drawing from laser-induced fluorescence thermometry methods that can currently be applied at low repetition rates (1-10 Hz), possibilities for kHz rate temperature imaging are considered.

2.1 Particle Image Velocimetry

For PIV, tracer particles must be added to the flow, typically in the form of oil droplets or solid particles (e.g. aluminium oxide Al_2O_3). These particles should be chosen with a size that is in principle small enough so they follow the flow motion. To obtain a single velocity field, the particles are illuminated twice separated by a short time delay with a thin (typically 100's μm) sheet of light, typically using a pulsed laser (e.g. frequency-doubled Nd:YAG laser at 532 nm). Mie scattering from the particles is imaged. For this, a dual-frame CCD is normally used. Each exposure, separated by a short time delay, contains an image of the particles when illuminated by one of the two laser pulses. In the resulting pair of images the particles have moved from one image to the next due to the flow motion. The images are divided into interrogation windows, and a cross-correlation algorithm is then used to determine the displacement of groups of particles in each window. Since the time delay between the laser pulses is precisely known, the velocity field can be determined.

PIV is a well-established and experimentally simple technique that is widely applied for flow measurements. Its versatility is clear from the numerous extensions of the method. Using two cameras that observe the measurement plane at different angles, the displacement of particles in the out-of-plane direction can be determined to measure all three velocity components (stereo PIV). High repetition rate lasers and cameras can be used for time-resolved measurements (high-speed PIV). Using a light sheet several millimetres thick and multiple cameras all three velocity components throughout the volume can be determined (tomographic PIV). Microscope objectives can also be used for measuring the velocity field in very small measurement domains (micro PIV).

While PIV is relatively simple to apply, one disadvantage is that the particles would interfere with Rayleigh scattering thermometry that is commonly used for temperature measurements in combustion research. The particle Mie scattering is several orders of magnitude stronger than the scattering from the gas molecules, but is at the same wavelength, so no separation between the detected signals can be achieved. This interference can be reduced by imaging through a spectrally sharp molecular or atomic filter which blocks the narrowband Mie scattering, but transmits the wings of the temperature-broadened Rayleigh scattering signal. This principle has been applied to perform Rayleigh thermometry simultaneously with PIV [17]. This is associated with considerable experimental complexity and requires that the gas composition, which determines the overall scattering cross-section, is either constant or a known function of temperature.

2.2 Time-Resolved Imaging Diagnostics

Advances in time-resolved planar measurements have been been enabled by the development of both high repetition rate diode-pumped solid-state (DPSS) lasers and high framing rate complimentary metal-oxide semiconductor (CMOS) cameras [6, 7], alongside more specialised ‘pulse-burst’ laser systems [8]. Like an ordinary low-speed laser, DPSS lasers run continuously and are used for long-duration ‘sustained’ measurements. However, the critical difference is that the pulse energy of these laser systems is very limited, with the indirect consequence that there is little flexibility in the available laser wavelengths. While pulse-burst systems have a much higher pulse energy, they cannot be run continuously, which limits their utility. Furthermore, in the context of quantitative measurements high-speed camera (and particularly high-speed intensifier) technology is not as mature. These limitations are discussed in detail in sections 4.2 and 4.3. In light of these restrictions, the current state of time-resolved PIV and scalar imaging techniques is briefly reviewed.

High-Speed PIV

At 532 nm DPSS lasers produce $\sim$ 10 mJ/pulse at repetition rates in the range 1-10 kHz. Because PIV relies on a strong Mie scattering process it has been successfully performed at kHz repetition rates in a number of applications (see below) despite the two orders of magnitude lower pulse energy.

High-Speed Scalar Imaging

For scalar imaging, such a drop in pulse energy is far more prohibitive and has restricted the adaptation of existing low repetition rate techniques for time-resolved measurements. Rayleigh scattering thermometry, for example, cannot be used for planar measurements with pulse energies of 10 mJ. At UV wavelengths DPSS laser pulse energies are around 1-10 mJ (355 nm) and $\sim$ 1 mJ (266 nm) at rates of 1-10 kHz. Most importantly, continuously operating high repetition rate pulsed laser sources at other wavelengths are not available. If a tunable laser source is required, DPSS lasers can be used to pump dye lasers at high repetition rates, but the resulting pulse energies very low (10-100 μJ).

Therefore time-resolved scalar imaging diagnostics are generally limited to laser induced fluorescence (LIF) of high quantum yield species, which are either naturally-occuring or deliberately added as a tracer. LIF techniques involve the electronic excitation of an atom or molecule by the absorption of laser light. The fast (ns) radiative decay to the ground state, termed fluorescence, depends on the species concentration, and possibly the temperature, pressure, and/or gas composition, permitting simple detection or quantitative measurement of some or several of these quantities.

Several studies employed LIF of flame radicals (e.g. OH, CH) combined with stereoscopic PIV for time-resolved investigations of turbulent flame phenomena [18–21]. LIF of biacetyl [22–24], acetone [25] and toluene [26,27] has also been used for quantitative mixing measurements in free jets and internal combustion engines, sometimes in combination with PIV. Laser-induced incandescence imaging of soot was recently demonstrated in Diesel engines [28].

Sustained, temporally-resolved combined vector-scalar measurements have provided insight into the reignition [29], propagation [21], and extinction [30] of flames; ignition and flame development [31] as well as misfire [32] in spark ignition engines; and thermoacoustic oscillations [33] and global extinction [19] in gas turbine combustors. The cited experiments demonstrate that simultaneous access to scalar and velocity fields is essential for the proper interpretation of high repetition rate imaging data.

These examples all include reacting flows, which highlights both the close link between flow diagnostic development and combustion research, but also that these experiments, where temperature is such an important variable, lack temperature measurements. There is only a single technique that has been used for planar temperature measurements at sustained kHz repetition rates, which is based on toluene LIF. This technique is discussed separately below.

Specialised ‘pulse-burst’ laser systems permit measurements approaching MHz rates with pulse energies of hundreds of mJ, but are limited in the number of pulses so only short recording times of around 1-10 ms can be achieved [8]. These systems have been used, for example, for flow visualisation in shock-boundary layer interactions [8] and mixing studies [34] in free jets. Because these systems are more flexible in generating specific wavelengths with sufficient peak powers at these repetition rates, LIF imaging of species e.g. CH [35] and CH_2O [36] have also been reported. For temperature, Rayleigh scattering can be achieved since the pulse energy is comparable to a low repetition rate system, and has been used to obtain short image sequences at 10 kHz in a turbulent jet flame [37, 38].

2.3 Possibilities for kHz-rate Temperature Imaging

This section looks at state of the art temperature measurement techniques, to consider their application at higher repetition rates. The discussion covers LIF thermometry, since such techniques satisfy the requirement that the signal can be separated from the excitation wavelength in some way. Therefore, they can be simultaneously applied with PIV.

There are a number of different tracers for LIF thermometry, some of which were mentioned above. Organic tracers are seeded into the flow by directing all or a part of the gas stream through the liquid tracer to generate vapour. The temperature of some species, e.g. hydroxyl (OH) radicals, can be probed where they are naturally generated by the flame. Other tracers such as nitric oxide (NO) or indium atoms can be added to the flow. First, thermometry based on LIF of toluene is discussed since it has already been demonstrated for time-resolved measurements under certain conditions.

2.3.1 High-Speed Toluene LIF Thermometry

Generally, the implementation of toluene LIF thermometry involves a single-wavelength excitation, dual-colour detection scheme. At high repetition rates a frequency-quadrupled DPSS laser at 266 nm is used for excitation (< 1 mJ/pulse) and two high-speed intensifiers coupled to high-speed CMOS cameras detect the UV fluorescence emission (peak 280 nm at room temperature) in two spectrally-filtered bands. The filters are chosen to exploit the redshift of the emission with temperature using a ratio-based technique.

In nitrogen at 293 K the quantum yield of toluene is 17%, but the overall signal decreases with temperature by two orders of magnitude between 300 and 700 K [39, 40]. Most importantly toluene is strongly quenched by oxygen where, using 266 nm excitation, at room temperature in air the emission intensity is reduced by a factor of 60 [41].

Therefore, for applications in oxygen-containing environments, the technique is limited to low repetition rates where the laser energy can compensate for the strong oxygen quenching. For example, two-colour toluene LIF has been used to image the temperature distribution in a motored spark-ignition engine run with air [42], using a KrF excimer laser at 248 nm for excitation. Laser fluences close to 100 mJ/cm^2 were used, which cannot be achieved using frequency-quadrupled DPSS lasers ($<$ 1 mJ/pulse). At high repetition rates measurements have to be performed in nitrogen.

This technique was first applied at a 10 kHz repetition rate in a heated jet of nitrogen impinging on a plate [43], where measurements up to 773 K were presented. It was later applied in combination with PIV at 6 kHz to investigate the evolution of temperature stratification due to compression [44] and fuel injection [45] in a motored spark ignition engine run entirely with nitrogen. The temperature precision of these measurements is 3% at 550 K, at a spatial resolution of $\sim$ 800 μm [44].

The sensitivity of the intensity ratio is an order of magnitude lower than the sensitivity of the overall signal to temperature (see above), prompting the investigation of single-colour detection strategies. In this case the temperature measurement is based on the temperature dependence of the fluorescence emission and the decrease in tracer number density due to gas expansion. Therefore, the measurement requires that the absolute concentration of the tracer must be held constant because unlike the two-color technique, this method cannot distinguish between temperature and concentration variations (and also variations in oxygen concentration). The approach has been used to measure temporally uncorrelated phase-locked temperature fluctuation fields in the compression stroke of a motored optical engine [46]. Sources of error due to tracer inhomogeneities when using a one-colour approach in engine applications have been analysed using high repetition rate imaging data [47]. Tracer condensation was found to cause large deviations from temperature fields measured using a two-colour method. Therefore in all but the most basic experiments, this approach is not considered favourable and the two-colour, ratio-based method is normally used.

There are two main disadvantages of using toluene LIF for thermometry. First, the UV emission of toluene requires the use of high-speed intensifiers, which suffer from nonlinearities and charge depletion effects [48]. This greatly complicates the LIF signal interpretation. Second, the measurements cannot be performed in air at kHz rates, due to the low pulse energy of high-speed lasers. Therefore studies must be restricted to pure inert gas environments, e.g. nitrogen, which prevents the use of the technique in reacting environments and large facilities e.g. wind tunnels, and limits the running time of engine studies.

2.3.2 Other LIF Thermometry Techniques

Here, other tracers currently used for LIF thermometry at low repetition rates are explored, to see if they can realistically be used for high-speed temperature measurements. As discussed, if the homogeneity of the tracer concentration can be assured, a simple single-wavelength excitation, single-colour detection approach can be used. Since this is rarely the case the usual approach is to remove any effect of the tracer concentration by performing a ratio-based measurement.

For all tracers considered here, dual-wavelength excitation in combination with single or dual-colour detection is used. This is necessary either to cancel effects of quenching due to the bath gas composition or because the emission spectrum is not temperature-dependent (e.g. acetone). A disadvantage common to all dual-wavelength excitation techniques is that the homogeneity of both light sheets must be assured or corrected for to make sure the ratio of excitation fluence is constant throughout the probe volume. The mean profile can be accounted for but beam profile irregularities and temporal fluctuations must be monitored or reduced using a beam homogeniser [49].

The same as for toluene, ketones e.g. acetone or 3-pentanone can be added as a tracer to the flow of interest. The thermometry strategy is to excite sequentially in time using two wavelengths that exploit the temperature-dependence of the UV absorption spectrum, and detect the resulting fluorescence following each laser pulse. The method for 3-pentanone and acetone is similar. 248 and 308 nm using KrF and XeCl excimer lasers [50, 51] is a sensitive combination of excitation wavelengths [52]. Images are taken with a short (100's ns) time delay so the flow field does not change, using for example a dual-frame intensifier and an interline transfer CCD [53], or two intensified cameras [51]. The ratio of these signals is a function of temperature. Acetone thermometry offers a high level of precision (1-2% at 300 K, depending on the excitation strategy) [52], and has been used for simultaneous measurements of temperature and the exhaust gas distribution in a fired spark-ignition engine [53]. Temperature calibration measurements up to 900 K have been performed.

The quantum yield of acetone, for example, is 0.2% [39], but it is not significantly quenched by temperature, oxygen or increasing pressure and the high vapour pressure (300 mbar at room temperature) permits high seeding concentrations. This technique is discussed as a possibility for high-speed measurements because acetone has been used for mixing studies at a repetition rate of 9.5 kHz using a frequency-quadrupled DPSS laser at 266 nm producing 1 mJ/pulse [25].

Signal-to-noise ratios between ~ 30 and 50 depending on the detection system could be achieved. However, the absorption spectrum of acetone and 3-pentanone spans 220 to 330 nm [39] and so for kHz-rate thermometry, another high repetition rate laser source that exploits the temperature-dependence of the absorption spectrum would be required (in combination with 266 nm, wavelengths above 280 nm (and below 330 nm) are appropriate [52]). The only sources are DPSS-pumped dye lasers, which do not provide enough pulse energy.

In sooting flames, for the same reason detailed above concerning PIV in the presence of tracer particles, Rayleigh thermometry will not work and atomic LIF techniques were developed as an alternative. Atomic tracers, typically indium, must be seeded into the flow as a metal salt e.g. indium chloride which are activated in the flame, or using laser ablation of an indium rod [54]. Indium atoms have been used as a tracer for thermometry up to 2800 K [55,56], in applications including a fired spark ignition engine [56] and a premixed flat flame burner [57]. Generally, two solid-state or excimer lasers are used to pump two dye lasers that excite transitions from two different ground states to a common excited state. For each pulse, separated by a short (100's ns) time delay, fluorescence from this upper level to the opposite ground state is deliberately monitored to achieve the desired spectral separation [58]. The ground state populations are temperature-dependent, so the ratio of the two signals, imaged using for example two intensified cameras [55], is a function of temperature.

Fully tunable radiation in the form of dye lasers are needed to match the spectrally narrow transitions. Drift or fluctuation of the laser frequencies significantly contribute to the measurement uncertainty [56,58,59]. In principle, 80 μJ/pulse, which has been used successfully for temperature measurements at low repetition rates [56], can also be generated using DPSS lasers pumping high-speed dye lasers. This would involve considerable experimental complexity. Even if this were feasible, the technique will only work above 800 K, where there is a sufficient thermal population of the upper ground state of indium.

In a similar way, molecular tracers can be used for thermometry. These might be added to the flow, e.g. NO [60], or be naturally present, such as OH radicals in flames or shock-heated mixtures [61]. Two dyes lasers are tuned to probe transitions involving closely-spaced rotational states, to cancel the tracer concentration and quenching effects. Spectrally-shifted UV fluorescence signals are detected using intensified cameras. For seeded tracers, temperature information can be obtained everywhere in the measurement domain. For OH LIF thermometry, temperature information is only available in post-flame regions > 1200 K, and bias due to the intermittent presence of OH in limited product regions must be considered when obtaining average temperature fields [62].

Considering the application of such a technique at high repetition rates, precise wavelength tuning of high-speed dye lasers would be required to match sensitive pairs of transitions. For NO, excitation is around 226 nm, and at high repetition rates this is not feasible due to heat buildup in optics. The technique would also require two high-speed intensifiers to detect the UV fluorescence, with the disadvantages outlined above. Therefore it is very unlikely that high-speed thermometry based on NO or OH radicals is possible.

2.3.3 Summary and Outlook

There are a range of LIF-based thermometry techniques which can be performed simultaneously with PIV. An important issue is the temperature range over which these tracers can be used. Organic tracers (toluene, acetone) will burn in flames, and at lower temperatures (< 273 K) the vapour pressure may be too low for sufficient tracer density, limiting the signal and causing condensation problems. Indium and OH radicals can only be used above a certain temperature. A further disadvantage is that all these tracers tend to have optical properties that make excitation and detection problematic, requiring high laser pulse energies, specific wavelengths or well-controlled laser spectral profiles, and usually multiple laser systems and intensified detectors. Such experimental complexity is what restricts the wide application of these techniques and is why they have infrequently, if it all, been used for temperature measurements, let alone simultaneously with PIV.

Despite the difficulties in achieving simultaneous temperature and velocity imaging even at low repetition rates, the preceding section explored how these techniques might be extended to much higher sampling rates. Limitations of the available laser technology makes this an extremely difficult task. For example, toluene LIF must be performed in nitrogen due to the low pulse energy of DPSS lasers. Application of other LIF techniques at kHz rates must rely on DPSS-pumped dye lasers with prohibitively low pulse energies. For dual-wavelength excitation the laser beam quality and control of the laser spectral profile would make such an approach very complex. The high laser energy of expensive, highly-specialised, and usually custom-built pulse-burst systems might in the future circumvent these issues and extend existing low-speed temperature diagnostics to kHz rates, albeit for short measurement durations. However, the same limitations when applying these techniques at low repetition rates would still apply.

The survey indicates there are no high-speed temperature imaging techniques for measurements in practical, oxygen-containing environments, that offer the essential capability of simultaneous velocity measurements.

A very different approach is to use thermographic phosphor particles, that are seeded into the flow as a tracer. These materials have many advantages compared with the LIF tracers described above. A technique for temperature and velocity imaging using phosphor particles is introduced in the next section.

2.4 Temperature and Velocity Imaging using Thermographic Phosphors

Thermographic phosphors are solid luminescent materials with temperature-dependent emission properties. Phosphors absorb excitation light, typically in the UV spectral region, and emit luminescence for an extended duration. Generally, either the temperature-dependence of the luminescence duration or the spectral profile of the emission are used for thermometry, either in one or two dimensions. Thermographic phosphors have been used for more than two decades to measure surface temperatures [63].

As a temperature sensor, phosphors have several important advantages. Firstly, there is a huge variety of phosphors with different luminescence properties. They have a wide range of temperature sensitivities, emission spectra, luminescence lifetimes, and luminescence intensities. Different phosphors can be used to cover temperatures ranging from the cryogenic [64] to 1900 K [65] and generally they have a melting point exceeding 2000 K. Many phosphors have broad absorption spectra in the UV spectral region and so they are flexible in terms of excitation wavelength. They also emit visible luminescence that can be easily detected using non-intensified cameras. The emission is generally insensitive to the pressure and gas composition [66,67], which is a critical advantage compared with the LIF tracers identified above.

By seeding thermographic phosphor particles into flows, they can be used as a tracer for both temperature and velocity. Laser light scattered by the particles is imaged to determine the particle velocity using an ordinary PIV approach. By exciting the particles and detecting their luminescence emission, the particle temperature can be determined. Micrometre-size particles are used, which rapidly assume the temperature and velocity of the surrounding fluid. This approach offers the possibility of simultaneous temperature and velocity imaging using simple instrumentation and a single tracer.

Following early studies in 2007 [68] and 2008 [69], the research on this topic began in 2010 at Imperial College. Our group implemented this concept and successfully demonstrated single shot measurements of temperature and velocity in 2012 [15]. The theoretical analysis and basic validation of the concept are included in the article published by our group [15] and thesis of my colleague Benoit Fond

[16]. Aspects of this work are only included here for clarity or continuity and are cited accordingly: the reader is referred to the published article (appearing as reference [15]) for further details.

The work presented in this thesis covers two major developments of the technique: its extension to simultaneous, time-resolved temperature and velocity imaging; and the characterisation of a phosphor that offers significant improvements in sensitivity. The thesis is organised as follows. The first part of chapter 3 introduces the basic theory of thermographic phosphors and their luminescence properties. A review of the literature on the topic of using phosphors to measure fluid temperatures is also provided. Chapter 4 contains the practical considerations and development work for the implementation of the technique at high repetition rates, and to increase the measurement precision. In chapter 5, demonstrations of time-resolved temperature and velocity imaging are provided and the performance of the technique is assessed. The characterisation of the phosphor zinc oxide for increased temperature sensitivity is reported in chapter 6. Chapter 7 summarises the findings of these studies and identifies key areas of future research.

3 Phosphor Thermometry

The aim of this chapter is to provide a basic introduction to phosphors and the ways in which they can be used for sensing temperature. The physical processes leading to luminescence and the ways in which the luminescence is altered by temperature are described. Essential luminescence properties of phosphors useful for temperature measurements in turbulent fluids are identified, before reviewing examples of flow measurements using phosphor particles.

3.1 Introduction

The most general definition of a phosphor is a solid luminescent material. Drawing on other definitions, it may be understood to mean “inorganic phosphors, usually those in powder form and synthesized for the purpose of practical applications” [70] and “usually intentionally doped with impurities” [71]. Phosphors are used in an enormous variety of applications, often to covert energy to produce light with specific characteristics. In cathode ray tubes a beam of electrons provides the energy which leads to the emission of light by the phosphor; in fluorescence lamps, UV light is responsible.

The basic principle is that the absorbed energy promotes the phosphor from a stable ground state to a state of higher energy. The phosphor is said to be excited: physically, the electrons are in a different configuration. The phosphor then radiatively decays back to the ground state. This is the light emission, or luminescence. A ‘thermographic’ phosphor is one where the luminescence emission is dependent on temperature, but this is true for all phosphors to some extent.

Examples include the UV emission of mercury which is used to excite three phosphors that emit blue, green and red light to produce the white light of fluorescence lamps. In plasma display panels, each ‘pixel’ is comprised of three different phosphors, each independently excited (again using the UV emission of mercury). The excitation is controlled to adjust the colour of the pixel. To make white light emitting diodes (LEDs), blue LEDs are used to excite a phosphor emitting a broad green to red band. Some phosphors are also used as scintillator materials to detect x-rays and gamma-rays. The incident radiation excites the phosphor and detecting the luminescence allows measurement of the harmful impinging radiation. In image intensifiers, electrons excite a phosphor screen and the visible luminescence is then detected by a camera. In solid-state lasers the visible pump radiation is absorbed by the crystal. The crystal emits the luminescence that is amplified by stimulated emission. For glow-in-the-dark toys luminescence is emitted for hours after the visible light, which excites the phosphor, is switched off.

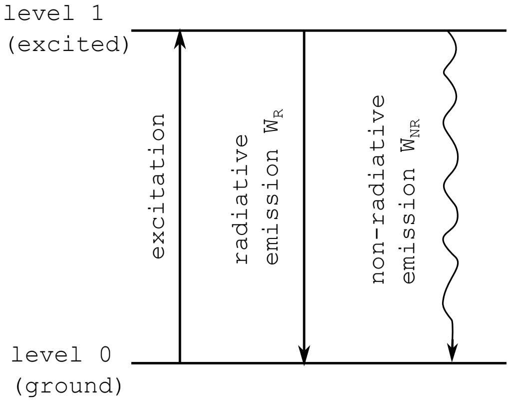

Figure 3.1: Two-level system showing excitation and radiative and non-radiative emissions.

Here the definition of luminescence is restricted to light emitted following the absorption of radiation from the UV to the infrared (for brevity: strictly speaking this is called photoluminescence). The physical mechanisms behind the brightness, colour and persistence of this luminescence, and how these are temperature-dependent and used for thermometry, will be discussed in the following sections. The following simple model shown in figure 3.1 illustrates the basic concepts of the time-dependent luminescence process.

Excitation light (provided by e.g. a pulsed laser) promotes luminescent centres in the phosphor from the ground (level 0) to upper excited (level 1) states, building an initial population N_{1_0} of excited centres. Following this, the population of the excited state decays according to the rates of radiative W_R and non-radiative W_{NR} emission:

$$\frac{dN_1}{dt} = -\left(W_R + W_{NR}\right) dN_1 \Longrightarrow N_1(t) = N_{1_0} \mathrm{e}^{-t/\tau} \tag{3.1}$$

Or in terms of the luminescence intensity I:

$$I(t) = W_R N_1(t) = W_R N_{1_0} \mathrm{e}^{-t/\tau} \tag{3.2}$$

where τ is the luminescence lifetime:

$$\tau = \frac{1}{W_R + W_{NR}} \tag{3.3}$$

The lifetime is the duration of the exponential decay of the light emission following excitation, due to electrons ‘trapped’ in the excited state. The total light emission I_{tot} is given by the integral of equation 3.2:

$$I_{tot} = \int_0^{\infty} I(t)\mathrm{d}t = \eta N_{1_0} \tag{3.4}$$

where η is the quantum efficiency, the fraction of absorbed light that is emitted:

$$\eta = \frac{W_R}{W_R + W_{NR}} \tag{3.5}$$

A high quantum efficiency is desirable to maximise the luminescence signal.

The interaction of light with solid materials depends on the optical characteristics of the material itself. The following considers how atoms form solids, and how in different cases the luminescence emission occurs and is affected by temperature.

3.2 Phosphors

The electron configuration is the distribution of electrons around the nucleus of an atom, that is established by the electrostatic interaction of the nucleus and all the other electrons in the atom. The distribution is described by atomic orbitals. A number (the principal quantum number) and letter (s, p, d, f) are used to designate the electron energy and angular momentum respectively, e.g. 1s, 2s, 2p, 3s, 3p, 3d, etc. Electrons occupy energy levels described by each orbital, and are referred to with this notation.

Considering a single, isolated atom, electrons occupy this set of discrete energy levels. However, phosphors take the form of a periodic arrangement of atoms called a crystal lattice, where atoms form bonds by sharing electrons. The potential field of multiple atoms (attractive forces of distant nuclei and repulsive forces of nearby electrons) causes a splitting of the energy levels. For a crystal comprised of n atoms, each original atomic level is split into to n energy levels, termed an energy band. In fact, the number of atoms in, for example, a phosphor particle is so large the bands are best considered as a continuum of levels [72].

Figure 3.2 illustrates this concept. As atoms are bought closer together to form the solid (decreasing atomic spacing, or separation of the nuclei), the discrete atomic levels are split into bands. The highest band occupied with electrons is called the valence band; the band above this, with higher energy, is called the conduction band. The energy separation between the two is named the band gap. In metals the valence and conduction bands overlap, so when accelerated by the presence of an electric field, electrons with increased energy are free to move into empty levels. Mobile electrons can then migrate through the material, permitting electrical conduction. Semiconductors and insulators have full valence bands; the next available band is separated by the energy gap and so these materials

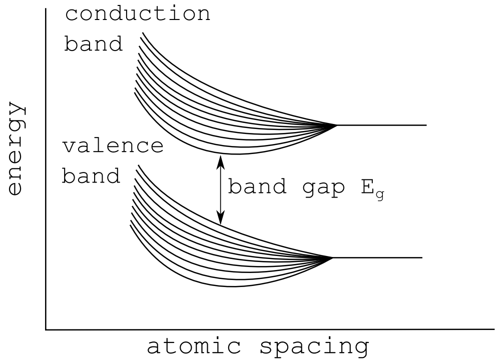

Figure 3.2: Splitting of energy levels to form electronic bands.

do not exhibit electrical conduction because in the presence of an electric field electrons cannot move into an empty level in the conduction band. The naming of insulators and semiconductors is somewhat vague because most semiconductors are anyway insulating. One reason for this distinction is that the band structure of semiconductors is often deliberately altered by introducing impurities [72].

The innermost electrons remain close to the nucleus in narrow bands, in a position similar to that for the isolated atom. The splitting of the atomic levels into bands is largest for the outer levels, because there the interaction between atoms is strongest. The atoms that form the solid partly determine the splitting of the levels and the band structure. Most phosphors are not comprised of a single element, and different elements will be present in varying quantities, and so the solid may consist of a geometric arrangement of complex molecules. The type of bonding, whether predominantly ionic or covalent, has a large influence on band structure [73] and therefore the optical properties.

Considering now the interaction of light with insulators and semiconductors, the absorption of incident photons with energies above the band gap ($E_g < h\nu$, where h is Planck's constant and ν is the frequency of the incident light) promotes electrons from the valence band into the conduction band [70]. Radiative (luminescence) or non-radiative processes can then occur. Such optical transitions involve valence electrons which participate in the formation of the solid and so the nature of the bonding is very important. Insulators have a large proportion of ionic bonding and large band gaps, e.g. sodium fluoride at 7 eV (177 nm). Semiconductors have a significant degree of covalent bonding and the band gap is lower e.g. zinc oxide at 3.37 eV (368 nm). These are 'interband' transitions between the valence and conduction bands in the material. Effectively, the whole material can be considered optically active.

A quite different situation is where either intentionally-added (doped) or naturally present impurities create energy levels within the band gap, between which 'band gap' transitions take place. Most often, these centres are involved in the luminescence emission [71]. Considering for example naturally-occurring impurities in semiconductors, transitions take place between the valence and/or conduction bands and the energy levels introduced by the impurities. However, usually impurities are deliberately added to produce the desired luminescence characteristics. In the case of rare earth or transition metal doped insulators, the processes of light absorption and emission take place entirely between the energy levels of the dopant ions. The host crystal lattice, normally transparent to visible light, is then said to be 'activated' by the impurity dopant ions. It is these latter class of materials that are most often referred to as phosphors, particularly in the context of thermometry.

A brief description of the luminescence mechanisms occurring in these two cases is now given. For more details, particularly for rare earth or transition metal doped phosphors, the reader is referred to references [73] and [74]. Reference [70] lists a huge number of phosphors used for a wide range of practical applications, and also contains some fundamentals of the luminescence process.

3.3 Luminescence of Semiconductors

Incident excitation photons of a given energy (above the band gap energy) promote electrons from the valence band into the continuum of levels forming the conduction band. Upon absorption, an electron promoted to the conduction band leaves behind a vacancy in the valence band called a hole. Coulombic attraction between the negative electron and positively charged hole forms an association called an exciton. In the excited state, this can be seen as energy levels below the conduction band. The energy difference between these levels and the conduction band is named the exciton binding energy.

Absorption of a photon above the band gap energy is shown in figure 3.3a. Non-radiative relaxation via the emission of phonons (quanta of lattice vibrational modes) occurs [75], before the electron and hole recombine to emit a photon. This emission is termed the near band 'edge' luminescence, occurring from exciton states (figure 3.3b) in semiconductors and insulators [70].

Exciton luminescence can occur due to excitons that are either 'free' or 'bound'. Impurities or defects create different levels in the band gap i.e. locally displace the position of the valence or conduction bands [72]. The emission from bound excitons results from transitions between these levels and/or the valence and conduction bands as shown in figure 3.4c. An example is where aluminium, indium or gallium impurities are deliberately added to zinc oxide (ZnO) [76], which affects

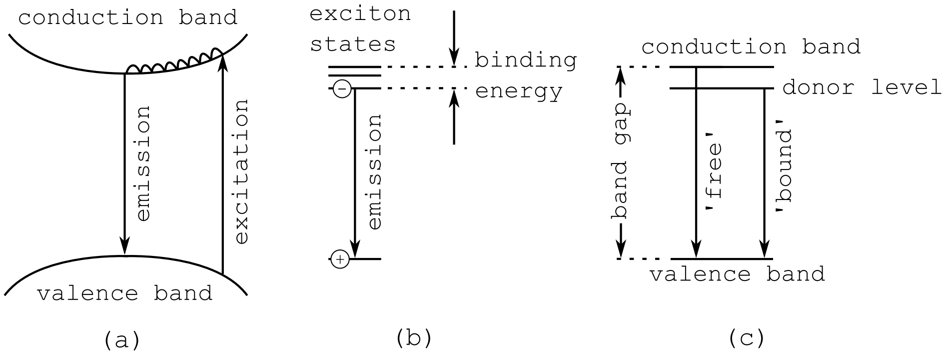

Figure 3.3: (a) absorption and emission processes in a direct gap semiconductor (see text). (b) representation of exciton states, found just below the conduction band in (a) and separated by the exciton binding energy. (c) Emission due to ‘free’ and ‘bound’ excitons, originating from additional (donor) levels within the band gap caused by impurities.

the position of the exciton emission peak maximum.

At very low temperatures (0-100 K), absorption spectra reveal sharp lines by absorption of incident light directly into the free or bound exciton states, and a broader band due to absorption into the continuum of levels in the conduction band. Normally at room temperature, these features cannot be distinguished due to broadening of the individual lines [75,77], and the absorption spectrum appears continuous as shown in figure 3.4. A representative emission spectrum of a typical semiconductor is also shown in figure 3.4. The luminescence emission occurs at a longer wavelength than the onset of the band gap, due to the exciton binding energy. Regarding the luminescence lifetime, radiative recombination of electrons and holes is probable in ‘direct band gap’ semiconductors, for example zinc selenide (ZnSe), gallium arsenide (GaAs) and zinc oxide (ZnO). The luminescence lifetime is therefore very short (< 1 ns).

Temperature Effects

With increasing temperature, the probability of non-radiative recombination via phonon emission increases due to the increased vibrational energy of the lattice. This increase in the non-radiative emission rate leads to a decrease in the quantum efficiency of the edge luminescence (equation 3.5).

Returning to the ‘difference’ between semiconductors and insulators, phosphors may be comprised of atoms with very different electronegativity. This means that one kind of atom has an increased tendency to attract electrons of different kinds of atoms towards it. In this way the ‘degree’ of ionic bonding within the solid increases, with the consequence that the valence and conduction bands tend

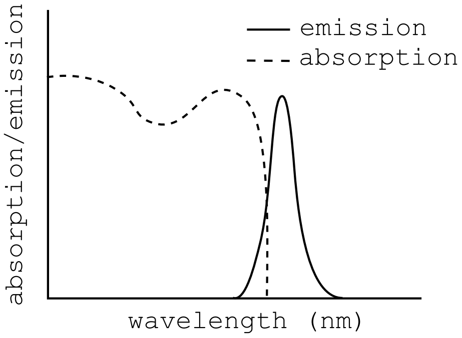

Figure 3.4: Typical absorption and emission spectrum for a semiconductor, showing the exciton emission. This is representative of room temperature, where free and bound excitons cannot be distinguished. The position of the broadened exciton peak will also depend on the type and concentration of impurities.

to each have the character of a particular type of ion [78]. Consequently, more energy is required to overcome the strong attraction of electrons to ions forming energy levels in the valence band and promote electrons to the conduction band. This is why an increasing degree of ionic bonding leads to a larger band gap [79].

As the temperature of the material increases the average separation between nuclei is larger, and so the potential field acting on the electrons decreases. The relative strength of the attraction toward ions of a different kind is therefore lower and so the band gap decreases. This shifts the absorption edge towards longer wavelengths. However, the attraction between electrons and holes remains the same (constant exciton binding energy) and so the edge luminescence also shifts to longer wavelengths.

Therefore there is a possibility to use semiconductors for remote thermometry by detecting the shift of the luminescence following excitation. In line with the accepted terminology, ‘insulators’ are not considered further here, because generally their band gap is so large that impractically short excitation wavelengths would be required in experiments. Rather, they are used in doped form as discussed in the next section.

3.4 Luminescence of Rare Earth and Transition Metal Doped Insulators

The previous section mentioned the role of impurities in semiconductors. In a similar fashion, small quantities of rare-earth or transition metal atoms can be added to a ‘host’ insulator, to which they form an ionic bond e.g. Eu^{3+} (europium), Mn^{4+} (manganese). Normally the laser excitation (occuring at photon energies much lower than the band gap) directly excites the dopant ions, which

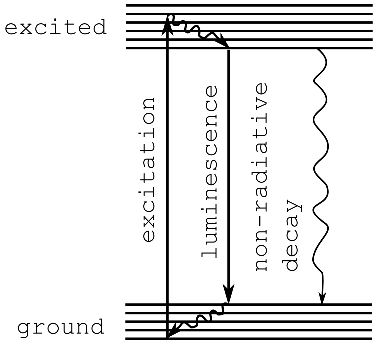

Figure 3.5: Two-level diagram for excitation, vibrational relaxation and luminescence emission. Thermal quenching between excited and ground states, leading to a decrease in the lifetime and quantum efficiency of the luminescence emission, is also shown.

then emit luminescence. This lends the material luminescence properties characteristic of the ion itself, completely different to those of the undoped material. Optical transitions take place between energy levels of the ion, which contain electrons that have little involvement in forming the ionic bond with the host lattice e.g. within the 3d level of transition metals, or the 4f level in trivalent rare earths. This is a clear difference between the interband transitions of semiconductors, where the valence electrons that hold the solid together are directly involved in the luminescence emission.

However, coupling with host lattice still has an important influence on the luminescence emission of the dopant ions, including the emission spectrum and temperature quenching behaviour. Using $BaMgAl_{10}O_{17}:Eu^{2+}$ (BAM:Eu) as an example, emission takes place between the mixed upper 4f5d and lower 4f orbitals. Even though the electrons participating in the emission do not directly contribute to the ionic bond, in the excited configuration the bond strength differs significantly so the equilibrium distance between the ion and lattice changes. The europium ions are said to be strongly coupled to the host lattice. A different case is the 4f-4f transitions of dysprosium in $Y_3Al_5O_{12}:Dy^{3+}$ (YAG:Dy). Whether in the excited or ground 4f states the bonding is similar. The effect this is has on the luminescence emission is revisited below, but an immediate example of this principle of ion-lattice coupling is the different spectral position of the emission line from divalent europium ions, if doped in different hosts. For dysprosium (and other trivalent rare earths) the emission is much the same regardless of the host [73].

The sequence of excitation, vibrational relaxation and emission is shown in figure 3.5. Prior to absorption the molecule is at some vibrational level in a ground electronic state. Incident photons promote the molecule to an excited electronic state. Fast non-radiative decay across vibrational levels in the excited state occurs via phonon emission, representing rapid dissipation of energy into the surrounding lattice. Photons are then emitted to a vibrational level of the ground state (this actually occurs over a range of vibrational levels depending on the temperature). Due to vibrational relaxation, the energy involved in the emission is lower than that in excitation and the emission occurs at a longer, Stokes shifted wavelength.

The luminescence of many transition metal and rare earth doped phosphors originates from optical transitions that are said to be forbidden on the basis of quantum mechanical selection rules. This has a significant effect on the luminescence lifetime. Transitions between electron configurations with the same principal quantum number are forbidden by the parity selection rule, for example the 4f-4f transitions in most trivalent rare-earths. Transitions can also be forbidden by the spin selection rule. These rules lead to the orders of magnitude differences in the lifetime. Broadly speaking, luminescence is very fast (order ns) where both rules are satisfied, of an intermediate duration (order μs) if only one rule is satisfied, and comparatively long (order ms) where the transition is forbidden on the basis of both rules. In this latter case, it is the coupling with the host that permits the observation of any luminescence at all. The transitions of YAG:Dy for example are forbidden, but due to interaction of the dysprosium ions with the YAG lattice luminescence with a lifetime of 1 ms at room temperature is observed.

Temperature Effects

As with semiconductors, the intensity of the luminescence emission is thermally quenched. The vibrational energy of the lattice increases with temperature and the probability of emission of multiple phonons that directly bridge the gap between excited and ground states is increased (multi-phonon emission), as shown in figure 3.5 [74]. Also, direct non-radiative transitions between excited and ground state (crossover relaxation) can also occur for phosphors with strong ion-lattice coupling. In both cases the non-radiative emission rate increases and the quantum efficiency decreases according to equation 3.5.

This increase in the non-radiative emission rate has a pronounced effect on the luminescence lifetime (equation 3.3), which can decrease by several orders of magnitude over a wide temperature range. For example, the lifetime of $Mg_4GeO_6F:Mn^{4+}$ changes between 3 ms at room temperature to below 1 μs at 1000 K [80]. By this mechanism different phosphors can be used for thermometry in different temperature ranges, depending on the onset of thermal quenching.

Measuring changes in the emission spectrum with temperature is another response used for thermometry. The emission spectra of YAG:Dy and BAM:Eu

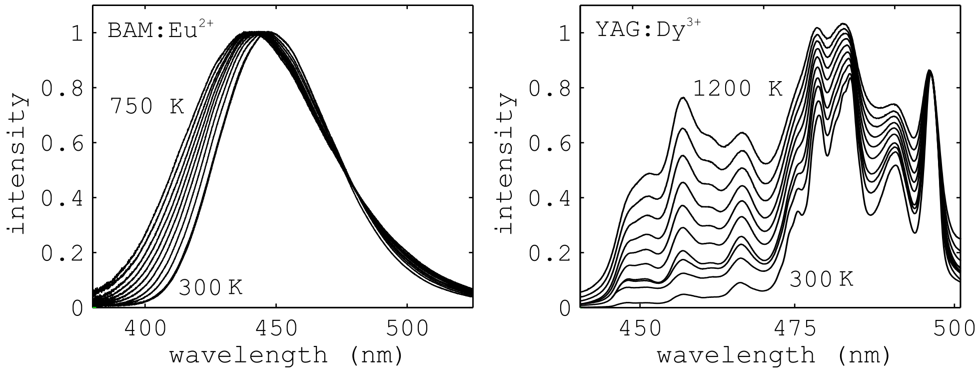

Figure 3.6: Normalised emission spectra of BAM:Eu^{2+} and YAG:Dy^{3+}.

phosphors are shown in figure 3.6. For YAG:Dy, the emission lines from different excited states to the ground state are spectrally narrow due to the weak ion-lattice coupling. Temperature changes the distribution of electrons in closely spaced excited states, altering the relative intensity of transitions between these states and a common ground state. This leads to a relative change in the intensity of the lines with temperature.

The broad emission of BAM:Eu is characteristic of the strong coupling between the europium ions and the host. With temperature, the emission line broadens and shifts towards the UV. The effect of temperature is to populate higher-lying vibrational levels, which leads to the broadening of the emission line. The effect is prominent because of the large difference in equilibrium ion-lattice separation in excited and ground states.

Such spectral changes provide another way to measure the temperature of the phosphor. How the temperature-dependent changes in lifetime and spectrum can be utilised for temperature imaging are discussed in the next section.

3.5 Phosphor Thermometry

3.5.1 Lifetime Method

Normally the lifetime method is used for point measurements e.g. on surfaces [81, 82] and in droplets [83]. Typically, the phosphor is excited using a UV laser and the luminescence is detected with a photomultiplier or photodiode. A fit through the temporal decay of the luminescence is used to extract the lifetime which is compared to calibration data. Due to the orders of magnitude change in the lifetime with temperature, this method is very sensitive. Compared to the intensity ratio method described below, it is less sensitive to the optical alignment

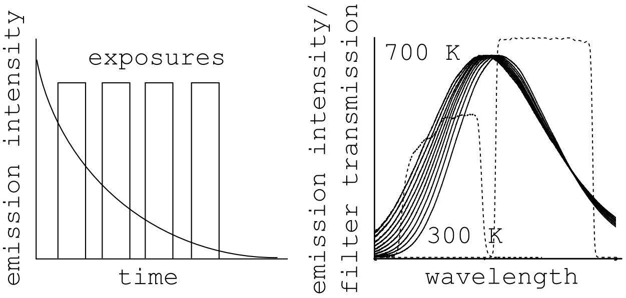

Figure 3.7: Strategies for planar temperature measurements using the lifetime (left) and intensity ratio (right) techniques (see text). For the lifetime method the exposures of a high-speed camera are distributed across the luminescence decay waveform. The intensity ratio method uses two interference filters (transmission profile superimposed) to exploit the temperature-dependence of the emission spectrum (that of the BAM:Eu phosphor is shown).

and more robust toward background interference, due to the nature of the fitting through multiple recorded points in the decay curve.

For two-dimensional measurements, a high-speed camera is used to image the luminescence decay. Frames distributed across the decay waveform are recorded and phosphorescence lifetimes are fitted to each pixel, as shown on the left in figure 3.7. Originally an intensified framing camera was used for this method for two-dimensional temperature imaging in droplets and sprays [84] and on the surface of burning materials [85]. High-speed CMOS cameras have been used to measure surface temperatures in engines e.g. [86, 87].

Such a method is difficult to apply in turbulent flows because short measurement durations (i.e. μs) are required to freeze the flow motion. A first requirement for this approach is a phosphor with a lifetime that varies around the μs scale, and a second is a camera capable of operating at frame rates around the MHz range at a reasonable spatial resolution. The general concept has actually been used for flow thermometry inside a motored IC engine at a sampling rate of 12.5 Hz using seeded $Mg_4GeO_6F{:}Mn^{4+}$ phosphor particles [88]. A high-speed CMOS camera operating at 40 kHz was used and four frames were recorded after each excitation pulse, for a total integration time of 100 μs. This approach is limited to relatively slow flows to avoid particles leaving the interrogation area during the total measurement duration. In addition, by covering only 100 μs of the decay, low temperatures cannot be reliably measured because the lifetime is much greater than the measurement duration ($>$ 1 ms below 670 K) [80], so the intensity between frames varies very little.

For much higher sampling rates, a suggestion for lifetime imaging is to use a high-speed CMOS running at 1 MHz (roughly the order of the maximum frame rate of current high-speed CMOS cameras, and at low resolution e.g. 256 x 24 pixels, see section 4.3) and a pulsed laser running at the desired sampling rate, e.g. 1 kHz. Using a phosphor with a lifetime that varies around 10 μs (if this measurement duration is acceptable for the application), the first ten frames of every thousand could be extracted for the lifetime determination.

Because the lifetime is so sensitive to temperature (changes by several orders of magnitude), from these examples it can be seen that any lifetime imaging approach applied in turbulent flows could only cover a limited range of temperatures.

3.5.2 Intensity Ratio Method

Alternatively, phosphors that exhibit a change in the emission spectrum with temperature can be used for thermometry. Generally used for planar measurements, the 'intensity ratio' is measured by exciting the phosphor using for example a pulsed laser and simultaneously imaging the luminescence using cameras fitted with two different interference filters, chosen to include emission lines or spectral regions that exhibit relative temperature dependency (see figure 3.7). The superposition and division of the two images results in an intensity ratio map, which can then be converted to a two-dimensional temperature field using a calibration curve. Examples of the intensity ratio technique include measurements on surfaces [89, 90], in sprays [91] and droplets [92], and for flow measurements using seeded particles. This last application is discussed separately below.

The measurement duration is determined by either the exposure time or the phosphorescence lifetime, whichever is shorter, and so the time resolution can be down to the nanosecond scale. In practice, ratio-based methods are straightforward to apply to planar measurements over a wide temperature range, using only two detectors and a single exposure. This is the temperature response utilised in this work.

3.6 Flow Temperature Imaging using Thermographic Phosphors

3.6.1 Phosphors Suitable for Flow Measurements

There is an enormous variety of phosphors, and the luminescence properties of many of them may be altered by changing the dopant concentration or adding impurities. Most phosphors have not been investigated and those that have were characterised primarily for lighting applications. Phosphors studied for thermometry were almost all doped with rare earth or transition metals. These studies indicate that different phosphors cover a wide range of temperatures, and that many have broad excitation spectra and emit visible luminescence. However, some further characteristics of the absorption and emission are either beneficial or essential for use as flow tracers.

Not all phosphors display a temperature dependence of the emission spectrum, but this is the first requirement of a phosphor suitable for ratio-based imaging. A sensitive response, i.e. a phosphor with a pronounced change in the spectrum for a small temperature differences is advantageous for precise measurements. In this context, chapter 6 of this thesis involves the characterisation of a phosphor with a very sensitive intensity ratio response.

For this technique, phosphor particles are seeded into flows in a dilute dispersion. They must be also small enough to trace the flow properties. This limits the number of luminescent centres in the measurement volume. The phosphor should therefore absorb as much of the excitation light as possible and have a high quantum efficiency, to maximise the signal. It should be noted that particularly for rare earth and transition metal doped phosphors, there is little data regarding absorption characteristics and quantum efficiency. Therefore it is hard to select or compare phosphors without testing them.

Finally, using a phosphor with a lifetime on the μs scale ensures that all the light can be collected during the short camera exposure, that must be used to resolve fluctuations in turbulent flows. Most of the emitted light must be rejected if using a phosphor with a lifetime on the ms scale, which drastically reduces the signal level.

The following short review shows the importance of some of these features in the success of the application of different phosphors as a flow tracer.

3.6.2 Review

The first reported experiments in 2007 used 4 μm diameter YAG:Dy particles to measure the temperature distribution in a heated jet and in a homogeneous charge compression ignition (HCCI) engine [68]. However, a later 2013 study showed that even 10 μm YAG:Dy particles do not emit sufficient signal for single shot measurements [93]. In 2008, $Mg_4FGeO_6:Mn^{4+}$ particles were used to simultaneously measure the temperature and velocity in heated air flows, but the signal was too low for single shot measurements [69]. The lifetime of these phosphors is in the ms range at room temperature, limiting the signal for short exposure times.

In 2010, work on the topic began at Imperial College. The phosphor BAM:Eu was identified as a promising phosphor for flow measurements due to its parity-allowed transition leading to a short luminescence lifetime of 1 μs at room temperature. Its quantum efficiency is also reported to be $> 90\%$ [70]. The first single shot temperature and velocity measurements were reported by our group in 2012 [15]. Measurements in a turbulent heated jet at temperatures of 700 K were presented. Since, several further studies by other groups using this phosphor have been reported [93, 94], as well as the use of other phosphors with longer lifetimes [95, 96].

All the aforementioned studies were aimed at low sampling rates of 1-10 Hz. In 2013, we extended the technique to sampling rates $>$ kHz using high repetition rate DPSS lasers and high-speed CMOS cameras [97]. This development work and demonstration of the technique is presented in detail in the next two chapters, using the phosphor BAM:Eu.

Based on the preceding introduction to phosphors and the temperature-dependence of their luminescence, it is evident that there are many possibilities to improve the technique by choosing an appropriate phosphor. In chapter 6, the use of the semiconductor zinc oxide for temperature measurements with increased sensitivity is reported.

4 Experimental Setup

This chapter outlines the design and development of an experimental setup for temperature and velocity imaging using phosphors. Emphasis is placed on extending the capabilities of the technique in terms of sampling rate and temperature precision. The performance of laser and camera technology suitable for high repetition rate measurements is analysed. The phosphor particles, experimental arrangement, and image processing techniques are described.

This chapter also contains experimental results. The high-speed cameras are characterised for ratio-based imaging, and compared to conventional low-speed cameras using simulations. To improve the measurement precision, the advantages of specific detection setups are quantified and modeled signals are used to identify filter combinations offering improved temperature precision.

In chapter 5, the developed high-speed system is applied to turbulent air flows ($Re \sim$ 700-10,000) in the temperature range 300-500 K. This chapter serves as a point of reference for applying the technique at high repetition rates, and need not be read in order.

4.1 Phosphor Particles

The phosphor should be chosen according to the considerations outlined at the end of the previous chapter. However, for this technique micrometre-size seeded particles are used and the size of these particles is critical. The particles must emit sufficient signal for precise thermometry, but accurately trace the flow. These points are covered in this section. Also, the manufacture and processing of particles, flow seeding methods, and the characterisation of phosphor particles for thermometry are discussed.

4.1.1 Signal and Particle Size

For a given phosphor material the luminescence signal depends on the absorption coefficient α at the excitation wavelength and the quantum efficiency of the transition detected for thermometry. α is proportional to the effective number density of luminescent centres in the material, and the probability of the absorption transition, and is related to the extinction coefficient k by $\alpha = 4\pi(k/\lambda)$. The real n and imaginary k parts of the complex refractive index $n - ik$ are optical constants of the material [73]. Both depend on the wavelength of the incident light.

The spatial extent of the solid, e.g. the particle diameter, also determines the nature of the laser-particle interaction and is critical in determining signal levels. The amount of light scattered and absorbed by a particle is determined

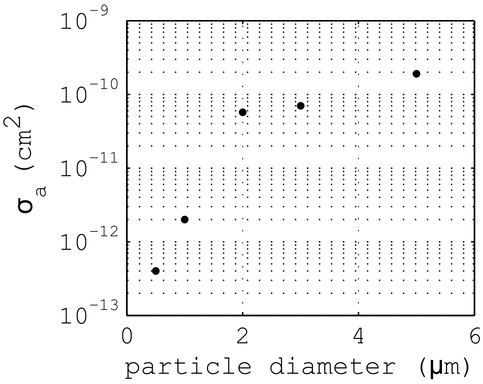

Figure 4.1: Absorption cross-section σ_a for different particle sizes. Calculated using an implementation [99] of the code provided in Bohren and Huffman [98].

by the scattering σ_s and absorption σ_a cross-sections. These cross-sections are calculated by solving Maxwell's equations for scattering by solid particles [98], using the particle diameter and the optical constants of the particle and medium, such as air. However, depending on the effective particle size, the cross-sections may have a complex dependence on the shape, structure and orientation of the particle. Often spherical particles are considered for simplicity.

In terms of the phosphor material, a large absorption coefficient and quantum efficiency are desirable, but for a given phosphor the effect of particle size on the scattering and absorption can be considered. Figure 4.1 plots σ_a against particle diameters 200 nm to 5 μm for an extinction coefficient of $k = 0.5 \times 10^{-5}$, a value consistent with measured luminescence signals of 2 μm BAM:Eu particles [16]. In this regime of low extinction σ_a increases with the cube of the particle diameter. Larger particles will absorb more light, leading to a dramatic increase in the luminescence signal.

Light scattering by small particles is a relatively strong process and the signal is often not a limiting factor for PIV. Due to interference effects occuring at the incidence of the laser light on the particles, the intensity of the scattering signal is strongly dependent on the angle of detection. This contrasts with the luminescence emission, which is emitted in all directions. Figure 4.2 plots the total scattering cross-section σ_s, and also the scattering at 90° $\sigma_{s,90^\circ}$ which is relevant to a typical PIV experiment light where light is generally collected normal to the direction of propagation of the laser beam. While σ_s follows the square of the particle diameter, $\sigma_{s,90^\circ}$ does not increase much over the considered range of particle diameters because of the large increase in forward scattering [98]. This produces the characteristic forward 'lobe' seen in phase plots of particle scattering,

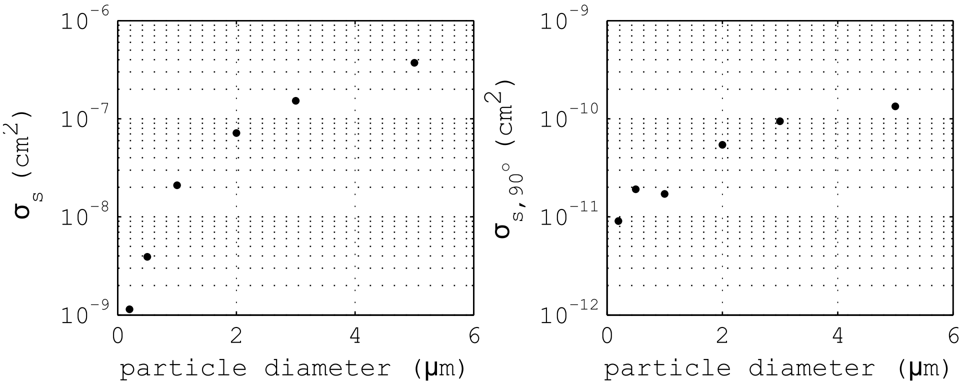

Figure 4.2: Left: total scattering cross-section σ_s and right: scattering cross-section $\sigma_{s,90^\circ}$ at a detection angle of 90° for different particle sizes. Calculated using an implementation [99] of the code provided in Bohren and Huffman [98].

in this regime of particle diameters.

Knowledge of the optical constants along with the quantum efficiencies of the appropriate transitions allows, to an extent, the comparison of different phosphors. Unfortunately these are often unknown, particularly for rare earth and transition metal doped phosphors. Therefore appropriate characterisation methods to determine signal levels are needed, as discussed in section 4.1.5.

4.1.2 Flow Tracing

The measurement accuracy fundamentally rests on how rapidly the tracer particles adjust to changes in fluid velocity and temperature. These are addressed in turn. The temperature tracing analysis is based on previous work carried out as part of this project and is not reported here in full. Only a short overview with some additional discussion is given, and quoted results from this work are cited where appropriate. For further information the reader is referred to the thesis [16], where detailed descriptions of the different models are provided, and the published article [15].

Velocity

For micrometre-size particles the particle Reynolds number is below unity for a wide range of gas viscosities and slip velocities, and a Stokes flow can be assumed. Considering a step change in gas velocity, the slip between the particle and the gas decays exponentially and can be characterised using the particle relaxation time constant τ_u, given by [100]:

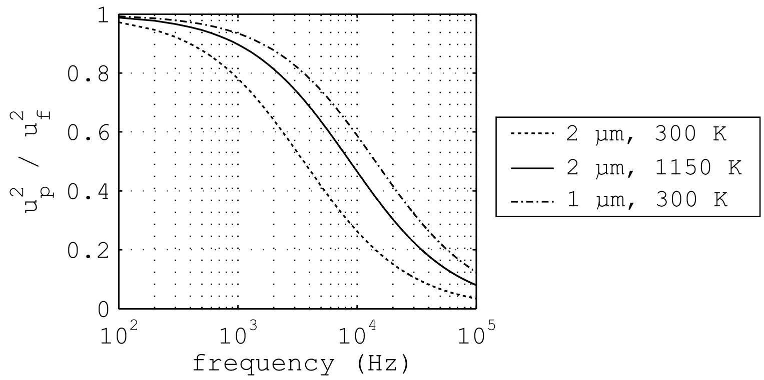

Figure 4.3: BAM:Eu particle response to flow velocity fluctuations of different frequencies in air.

$$\tau_u = \frac{\rho_p d_p^2}{18\mu} \tag{4.1}$$

The relaxation time scales with the square of the particle diameter d_p. It also increases with a reduction in gas temperature owing to the decrease in viscosity μ, and scales with the tracer material density ρ_p. Most phosphor materials such as BAM:Eu (3.70 g/cm^3) and YAG-based phosphors (4.55 g/cm^3) have a density similar to tracers widely used in PIV such as TiO_2 (4.23 g/cm^3) and Al_2O_3 (3.94 g/cm^3), resulting in very similar response times. As an example, in air the $3\tau_u$ (95%, $\tau_{u,95}$) relaxation times for 2 μm particles range between 53 and 65 μs at a mean gas temperature of 1150 K.

Other analyses use the frequency of the turbulent velocity fluctuations to determine the appropriate particle size [101, 102]. In this case, 2 μm particles of a similar density were reported to follow turbulence frequencies of 1 kHz in a lean methane-air flame [101]. Following this approach, the ratio of the time-average fluctuation velocities of the particle u_p and fluid u_f is given by [102]:

$$\frac{\overline{u_p^2}}{\overline{u_f^2}} = (1 + 2\pi f_c \tau_u)^{-1} \tag{4.2}$$

where f_c is the frequency of the turbulent flow. From this, different curves representing the relative particle and fluid fluctuations for different flow frequencies can be plotted for different BAM:Eu particle sizes and air temperatures as shown in figure 4.3.

For flow frequencies above several hundred Hz, PIV measurements using 2 μm particles will dampen the turbulent oscillations. Therefore, for measurements of second order statistics smaller particles may be required.

Temperature

The particle temperature must also rapidly assume the gas temperature. Owing to the volumetric heat capacity of the particle, a large transfer of thermal energy through the poorly conductive gas is required in order to achieve thermal equilibrium. From the foregoing analysis of the particle velocity, for micrometre-size particles heat transfer is dominated by conduction.

The temperature response involves a transient, one-dimensional, heat conduction problem. The system consists of a spherical particle in an infinite fluid, at different initial temperatures, e.g. a cold particle immersed in a hot gas. The particle thermal conductivity, of the order 10 - 20 W/mK for some well characterised host materials such as YAG or Y_2O_3 [103], is more than two orders of magnitude larger than the gas conductivity (< 0.1 W/mK for air at 2000 K). Consequently, the temperature inside the sphere can be considered uniform at all times. The temperature response time is therefore limited by heat transfer through the gas.

Two approaches were used to analyse the temperature response. The first is a lumped capacitance approach, considering time-independent heat conduction in the gas. Similar to the expression for the velocity relaxation time above, the temperature relaxation time τ_T, is given by [104]:

$$\tau_T = \frac{\rho_p C_{p_p} d_p^2}{12 k_g} \tag{4.3}$$

The temperature response has a quadratic dependence on the particle diameter, and is inversely proportional to the temperature-dependent gas thermal conductivity k_g. The volumetric heat capacity of the particle is represented by $\rho_p C_{p_p}$. The second approach uses a finite difference numerical model to solve the heat conduction equation [16], which was validated against an analytical solution [105]. This numerical model has two main advantages, in that it can model the temperature-dependent local gas thermal properties, and also account for radiation effects.

Table 4.1 compares the results of the two approaches for a 2 μm particle at 300 K in dry air at a temperature of 2000 K. The specific heat capacity C_{p_p} and density of undoped YAG at 300 K were used [103]. Two results using each model are listed. The numerical model results are given for uniform gas thermal properties evaluated at 2000 K and also accounting for local temperature-dependent gas thermal properties (thermal diffusivity $\alpha = k_g/\rho_g c_{p_g}$, where k_g, ρ_g and c_{p_g} are the gas thermal conductivity, density and specific heat capacity). Using the

Model	$\tau_{T,95}$ (μs)
Numerical model (T =2000 K)	26.9
Numerical model (variable T)	35.0
Lumped capacitance (T =300 K)	107.9
Lumped capacitance (T =2000 K)	26.8

Table 4.1: Temperature response times using different models and gas thermal properties evaluated at different temperatures, for a 2 μm YAG particle.

lumped capacitance model, the response time is evaluated using the gas thermal conductivity at two different temperatures (300 and 2000 K).

The lumped capacitance model is in good agreement with the numerical model result when using constant gas thermal properties. When accounting for the temperature dependence of the gas thermal properties in the numerical model, in this case of a cold particle in a hot gas, the response time increases by $\sim$ 30% to 35 μs. This is because the gas beside the particle is initially cooled down, which reduces the gas thermal diffusivity. The lumped capacitance model evaluated at the gas temperature will slightly underestimate the response since it does not include this effect, but using the initial particle temperature (in this case 300 K) results in a large overestimate. Therefore the lumped capacitance model serves as a useful guide to the particle temperature response time, if the gas thermal conductivity at the initial gas temperature is used.

Using the numerical model, effects of radiation on the response time can also be determined. The response time is increased by just a few %, because the rate of conductive heat transfer is much higher than the rate of radiative heat transfer from the particle during the transient regime. When the rates of conduction and radiation become constant there is a small steady state error which increases with the gas temperature and particle size, e.g. for 2 μm particles at 2000 K the error is just 8.6 K, for surroundings at 300 K [15].

While the temperature response time of the particles is critical for the measurement, the effect of the particles on the gas must also be evaluated. Considering an insulated boundary (fixed volume of gas and particles) the reduction in gas temperature can be evaluated for a fixed particle number density (number of particles per unit volume of gas, also sometimes referred to as the seeding density). Depending on the requirements of the measurement, typical particle number densities ranging from 10^9 - 10^{12} particles/m^3 might be used. For example, 15 particles per interrogation volume are recommended for PIV [102] so for a vector resolution of 600 μm a particle number density of 10^{11} particles/m^3 is required. For this particle number density, the bulk gas cooling caused by the extraction

	$\tau_{U,95}$ (μs)	$\tau_{T,95}$ (μs)
T=300 K	164.3	107.9
T=1150 K	67.2	38.1

Table 4.2: Temperature and velocity response times at different air temperatures for a 2 μm YAG particle.

of heat by the cold particles is 7.2 K at a gas temperature of 1900 K [16]. The volume fraction occupied by the particles is very small: at this particle number density the effect of the gas thermal conductivity is negligible, and the gas heat capacity is increased by just 0.5% at 1900 K.

Discussion and Summary

To summarise, for direct comparison of temperature and velocity responses, relaxation times at air temperatures of 300 and 1150 K are calculated using equations 4.1 and 4.3 for 2 μm spherical YAG particles, and shown in table 4.2.

The temperature response is faster than the velocity response, and so following the same restrictions when using solid tracer particles for PIV, the particles can also be used for temperature tracing. Both response times are significantly improved at higher temperatures due to the respective increase in thermal conductivity and viscosity.

Radiation has a negligible effect on the accuracy of the temperature measurement. Furthermore, the analysis indicates that for seeding densities of 10^{11} particles/m^3 there are no effects on the gas thermal properties.

The modeled responses for 2 μm particles at room temperature are $\sim$ 100 μs and so for high-accuracy measurements of turbulent temperature-velocity correlations, the use of smaller particles might be required. In theory, for the same particle number density, using particles with a smaller diameter will reduce the absorption cross-section and therefore the luminescence signal, by the cube of the particle diameter. However, since in principle the signal depends linearly on the particle number density, the same mass of particles can be seeded into the flow (i.e. an increase in the particle number density), increasing the signal without adversely affecting the gas thermal properties.

There are two limitations to this. Firstly, very high particle number densities may adversely affect the cross-correlation algorithm used for PIV. Secondly, from the considerations outlined in the following sections, particles cannot necessarily be obtained in any size, and even if this were the case, seeding particles of a specific, precisely-controlled diameter is not trivial.

It should be noted that a sphere has the minimum ratio of surface area to volume and any other shape will have a faster temperature response time. Considering the SEM image of the 2 μm BAM:Eu particles used in this work (figure 4.4), the flat, hexagonal discs will possess much better temperature tracing properties as well as significantly improved drag characteristics, also leading to a faster velocity response.

4.1.3 Phosphor Manufacture

When choosing phosphor particles the ability to obtain them with the exact size, shape, and structure is desired, as well as control the propensity of the particles to agglomerate. The manufacture of phosphors, and the difficulty in handling (e.g. seeding in the flow), processing and measuring fine powders, limits the possibilities for this.

Rare earth or transition metal doped thermographic phosphor powders are frequently produced using a solid state chemistry method [106]. Stoichiometric quantities of the precursor powders, including dopant e.g. europium in Eu_2O_3 are mixed (possibly with an additional flux) and heated, typically to > 1300 K, for an extended time (hours). The phosphor might then be ground using e.g. ball milling and then re-fired in an additional oxidising step. The specific details depend on the phosphor powder being manufactured [107]. Alternative techniques exist like the sol-gel method (the phosphor is synthesised from a liquid solution and deposited as a thin film on a surface) or precipitation from the liquid phase. There are other production techniques for particles made of different materials, e.g. semiconductors, that might be used for thermometry.

The particle size is chosen by the manufacturer to suit the original application such as lighting, or displays. Commercially available phosphor powders were used in this work. There are some inherent limitations in manufacturing and processing techniques. A production technique that yields a phosphor considered favourable for thermometry may not be suited to production of the material in the right range of sizes required for flow tracing. Furthermore the chemical composition of the precursors and phosphor product may have a tendency to produce particles of a certain size and state of agglomeration. Additional processing steps, like grinding, affect the surface characteristics, introduce impurities and can embrittle particles. Therefore the particle size cannot be arbitrarily chosen and will instead possess a certain distribution of sizes and possibly different shapes. Narrowing of this distribution using separation techniques (e.g. sieving, sedimentation) is difficult and, on account of the inefficiency, very expensive for powders in the micrometre size range useful for flow tracing.

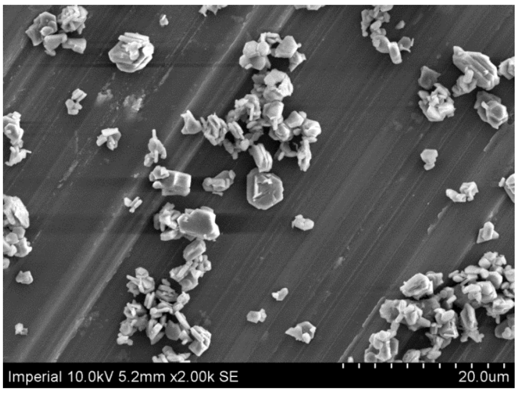

Figure 4.4: SEM image of BAM:Eu powder.

The distribution is often quoted as a cumulative distribution by volume. For a sample where for example 50% of the particles are below a certain size, there will be many more small particles. Size distributions are determined using techniques like electrozone sensing (Coulter counter) and laser diffraction [108].

Scanning electron microscope (SEM) images give a reasonable qualitative indication of the particle size and shape. An example image is shown in figure 4.4 for the BAM:Eu particles used in this study (KEMK63/UF-P2, Phosphor Technology). The image shows that the particles have flatter, angular disc shapes. The particle sizes appear consistent with the distribution quoted for the batch (50 %vol < 2 μm).

4.1.4 Particle Seeding

The preceding sections have identified factors that determine the appropriate particle size, and some limitations in obtaining particles of the desired distribution. However, controlling the seeding process so that the intended distribution of particles is delivered to the measurement region is crucial.

Geldart's classification of powders indicates that phosphor particles of the diameter required for accurate flow tracing belong to cohesive group C powders that cannot be fluidised in a strict sense [108], since the interparticle attractive Van der Waals forces are large compared with the drag force. The ease of dispersion depends on the particles themselves (size, shape and also electrical properties which govern the cohesive forces between particles), the manner in which the powder is handled prior to seeding, and the seeding method itself. Three seeding strategies and appropriate treatment of phosphor powder are described here.

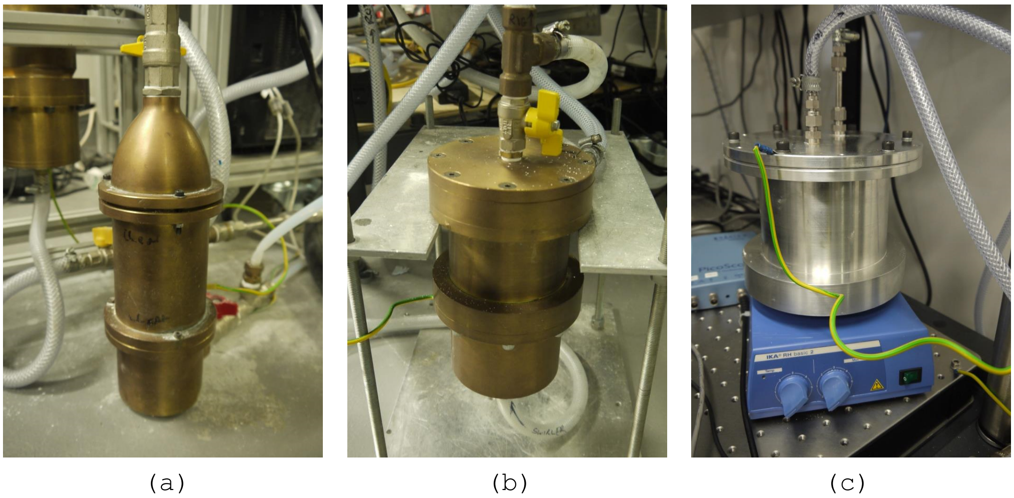
(a) (b) (c)

Figure 4.5: Particle seeders: (a) fluidised bed, (b) cyclone and (c) magnetic stirrer design.

Seeders

A fluidised bed seeder (see photographs in figure 4.5) uses the basic principle of fluidisation as a means of creating an airborne stream of particles. The flow is passed up through a porous plate and into the packed bed of particles. However the name 'fluidised bed' is something of a misnomer. Channels appear in the bed and particles that are seeded into the flow are entrained from these channels or from the bed surface, or on occasions the channels collapse. Consequently, the temporal consistency of the seeding is poor and the flow is likely to contain large agglomerates.

A cyclone seeder [109] generates a vortex by injecting air tangentially into a vessel filled with particles. The design used in this work used a swirling flow in the vicinity of the particle bed which passes up into a separate chamber where a counter-rotating main flow acts to separate large agglomerates by centrifugation. Consistent and spatially homogeneous seeding was obtained using this design, free of the large signal spikes characteristic of large agglomerates. This seeder is appropriate for larger flowrates > 100 L/min.

Another design more suited to seeding lower flowrates down to ~ 10 L/min was also used for these measurements. The flow is directed downward into a chamber filled with particles, and mechanical agitation is provided by means of a magnetic stirrer to disturb the bed and fluidise particles, which are extracted from the top of the vessel. The seeding using this design is also reasonably consistent and spatially homgeneous.

Particle Handling

Further steps involve drying the particles at moderate temperatures of ~ 150 °C for several hours before use, since moisture has a tendency to increase agglomeration, and grounding the seeder) to reduce the buildup of static electricity. Aerosil or Ludox coatings are flow aids based on SiO_2 nanoparticles, which enhance the flowability and reduce agglomeration by increasing the surface roughness, thereby increasing the particle separation and reducing attractive interparticle forces. The phosphor powder and Aerosil nanoparticles can either be mixed, or in the case of the Ludox coating the phosphor particles are suspended in an SiO_2 solution and then dried, creating an even coating of nanoparticles (an example can be seen in figure 6.2d in chapter 6).

4.1.5 Phosphor Characterisation

Chapter 3 identified favourable properties for a thermographic phosphor suitable for flow thermometry. However, as discussed above, in general the quantum efficiency of the relevant transitions and absorption coefficient of most phosphors are not known. Therefore a means of characterising phosphor particles is needed.

The simplest way to achieve this is probing the particles in the form of aggregated powder (see figure 4.6), which is often used to measure e.g. the emission spectrum or luminescence lifetime. In principle this is reproducible since the particles are immobile, and there are many particles so signal levels are high. However, using this method the number of particles contributing to the signal is unknown, yet for flow thermometry, the quantity of interest is the signal per particle. Furthermore, due to multiple scattering the optical properties of a particle are different whether it is dispersed in a gas or as part of a dense collection of particles [70]. Further difficulties in interpreting results acquired from studies of aggregated powder include effects such as laser-induced heating or damage, which may not occur in the gas.

Therefore it is necessary to also characterise phosphors in the flow, where the nature of the laser-particle interaction exactly matches the intended use for temperature imaging experiments. However, due to the difficulties in reproducing seeding conditions, let alone knowing the absolute number of particles, the number of particles that are being probed must be directly measured in situ.

This is neccessary for three reasons. First, fluctuations in the seeding density must be corrected for when varying certain parameters (e.g. laser fluence) providing repeatable quantification of signal levels for a given set of conditions. Second, this permits comparison of overall signal levels of different phosphors. The third reason is that with knowledge of the absolute number density of particles needed

Figure 4.6: Aggregated phosphor powder.

for appropriate signal levels, the effect of the particles on the gas properties can be evaluated.

In this work, a system developed by my colleague Benoit Fond at Imperial College was used to measure the number of seeded particles. This particle counting technique uses high-resolution Mie scattering images of seeded particles, instantaneously sampled in the same probe volume as the thermometry system [110]. The system is described in chapter 6 and used to characterise a phosphor for temperature measurements with increased sensitivity.

4.2 Laser Light Sources

Given that the instantaneous measurement duration is limited by the timescales of the turbulent flow to be investigated, normally the excitation duration need only be comparable to (or shorter than) this time. The ability of pulsed laser systems to deliver high energy in a short time is therefore beneficial for single shot imaging. In principle, all the optical power produced by the laser can be used to generate the measured signal. For continuous light sources (~ 1 W at UV wavelengths), the energy delivered to the region of interest during the measurement duration (normally defined in this case by the exposure time, set to match the desired temporal resolution) is much lower, and is in general unsuitable for planar scalar imaging.

Solid-State Lasers

First the excitation wavelengths required for phosphor thermometry are considered. For low repetition rate (< 10 Hz) applications, pulsed lasers based on different gain media are available. Depending on the specific wavelength, from the UV to IR pulse energies of the order mJ - J can be obtained. However, the fact that most phosphors have broad absorption bands in the UV spectral region does not place great restriction on the excitation wavelength. Therefore solid-state lasers based on e.g. neodynium-doped YAG crystals can be used, which produce light of fixed wavelength in the visible and UV.

The fundamental emission is at 1064 nm. KDP or BBO crystals can be used to efficiently generate light of a different wavelength via a nonlinear harmonic generation process, e.g. 532 nm (frequency-doubling). Dual-cavity frequency-doubled Nd:YAG lasers are often used for PIV due to the high pulse energy (100's mJ/pulse) and the sensitivity of cameras in this spectral region. Higher harmonics at 355 and 266 nm can also be extracted, with pulse energies around 10 - 100 mJ. It is these wavelengths that match the broad absorption bands of most phosphors.

Solid-state lasers are simple to operate and easy to maintain. This is an advantage considering other low repetition rate pulsed laser sources such as dye or excimer lasers, which require handling of harmful laser dyes or toxic gases.

4.2.1 High Repetition Rate Laser Systems

At the kHz - MHz rates that are required for time-resolved imaging, continuously producing pulses with equivalent energy to low repetition rate systems is very difficult. The optical output power is considerably lower than the electrical input and so at high repetition rates, a lot of excess energy must be removed from the laser, placing great demand on the thermal management. Even with more efficient laser systems, greatly reduced pulse energy or operation for a limited duration must be tolerated to achieve high repetition rates. It is this that restricts the application of conventional planar laser thermometry techniques, some of which were outlined in chapter 2, to time-resolved measurements.

Options for high-speed laser systems are limited. Some types of solid-state laser offer high repetition rates, but different pumping schemes or laser clusters and 'pulse-burst' systems are used. These are discussed in this section. Where applicable, the conversion of the fundamental and harmonic frequencies for other diagnostic techniques is highlighted. In the same way that the limited pulse energy restricts the application of established measurement techniques, low peak power and sometimes beam quality also limits the range of wavelengths that can be used.

Laser Clusters

Early efforts to achieve time-resolved measurements simply used several lasers or custom-built systems, such as a design from Thales consisting of four independent Nd:YAG lasers. The Q-switch of each cavity can be fired twice with a short (10's μs) time delay. This produces a train of 8 pulses at 100's mJ/pulse. For example, a similar system was used to pump a dye laser to obtain time-resolved OH LIF image sequences of a turbulent non-premixed flame [111]. Such an approach is expensive and impractical to extend to longer measurement sequences.

‘Pulse-burst’ Systems

These systems produce a train of pulses with energies of a similar magnitude to a conventional low-repetition rate solid-state laser. In an example of such a system [8], the fundamental output of a continuous-wave Nd:YAG laser is sliced into individual pulses (energies of $\sim$ nJ/pulse) using acousto-optical modulators and then amplified using a chain of flashlamp-pumped Nd:YAG amplifiers, typically by a factor of up to $\sim 10^9$. These systems were until recently custom-built and so performance varies, but pulse energies exceeding 1 J and repetition rates approaching MHz are achievable (depending on the specific combination of pulse energy and repetition rate, see below). Using harmonic generation or optical parametric oscillators UV wavelengths can be generated (e.g. 390 nm for CH imaging at 10 kHz [35], 355 nm for CH_2O imaging at 100 kHz [36]). The capabilities of these laser systems are constantly evolving, and commercial systems are now available [112].

Operated continuously, the system must be run in a duty cycle mode of operation (the burst duration compared with the ‘off’ time where heat must dissipate or be removed by cooling). The burst duration (normally of the order 1-10 ms in flashlamp-pumped systems) and the combination of maximum pulse energy and repetition rate is limited. The temporal envelope of the flashlamp pulse determines the time during which pulses can be amplified, which also restricts the burst duration. Alternatively, a recent system using diode-pumped Nd:YAG amplifiers was demonstrated to achieve 100 ms bursts with pulse energies of 250 mJ at 10 kHz and 40 mJ at 100 kHz at 1064 nm [113].

Diode-Pumped Solid State Lasers

Q-switched diode-pumped solid state lasers, in which laser diodes are used to pump the gain medium, are generally used for the ablation of material for laser machining. Commercially available DPSS lasers are also now used for high-speed laser diagnostics.

Due to thermal limitations, increasing the repetition rate of the laser would ordinarily require that the pulse energy is reduced so that the heat produced when operating continuously can be handled by the cooling system. In diode-pumped Nd:YAG lasers aluminium gallium arsenide laser diodes are used. The emission better overlaps the absorption spectrum of Nd:YAG compared with broadband

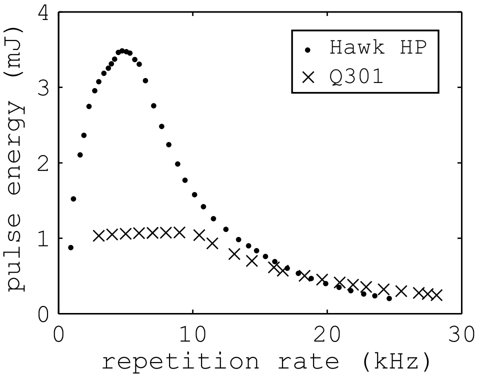

Figure 4.7: Pulse energy of the frequency-tripled DPSS lasers used in this work. Nominal values are indicated; typically actual measured values are slightly higher.

flashlamps and so the overall efficiency is improved [114]. This permits an increase in the power output. Diode-pumped Nd:YAG lasers typically produce several 10's mJ/pulse at 1064 nm, in the 1-10 kHz range. Unlike pulse-burst systems, DPSS lasers run continuously.

The fundamental output can be converted to visible and UV wavelengths using an intra- or extra-cavity harmonic generation scheme. Frequency-doubled dual-cavity systems are available for PIV. At 355 nm, the power produced across a broad range of repetition rates (from single pulse to 100's kHz) depends on the specific laser, but typically pulse energies around 1-10 mJ can be obtained in the range 1-10 kHz (see figure 4.7). At higher repetition rates the pulse energy decreases. At 266 nm, there are additional limitations owing to heat buildup in the crystal (and other optics) due to slightly increased absorption at this wavelength. This affects the output power [47] and the susceptibility of optics to damage [27], and so for high repetition rate measurements excitation at 355 nm is advantageous. The 532 and 355 nm output can be used to pump dye lasers, permitting time-resolved LIF imaging of flame radicals (e.g. CH at 390 nm [20], or doubling from 566 nm to excite OH at 283 nm [115]) using pulse energies of just 10-100 μJ.

DPSS lasers have good pulse-to-pulse energy stability, typically $<$ 2-3%. Depending on the laser design the M^2 factor ranges from values comparable to low repetition rate solid state lasers ($\sim$ 1) to $\sim$ 50. An example is the Hawk HP (Quantronix), used in section 6.5, which has $M^2 \sim 30$. However, in this work it was found that forming a laser sheet with a waist < 300 μm using a single cylindrical lens was a simple matter.

A novel application of DPSS technology is using a frequency-quadrupled Nd:YLF laser (fundamental wavelength 1053 nm) to excite OH radicals at 263 nm [116]. However the extended pulse duration of some DPSS systems (100's ns) can limit the conversion efficiency. Edge-pumped slab laser designs (such as that offered by Edgewave GmbH) offer short pulse durations of 1-10 ns similar to flashlamp-pumped solid-state lasers.

4.2.2 Discussion and Summary

No laser light source other than pulsed Nd:YAG lasers operating at the third (355 nm) or fourth (266 nm) harmonic is required for phosphor thermometry, due to the broad UV absorption band of most phosphors. This is a significant advantage compared to many LIF tracers, which usually require specific laser wavelengths, e.g. dye or excimer lasers, to match the absorption features of the tracer.

For high repetition rate measurements, excitation is restricted by the operating range of high-speed lasers, in terms of pulse energy and measurement duration. Therefore the most important consideration for high-speed measurements using phosphor particles is the laser energy required. Using the phosphor BAM:Eu, previous work by our group showed that in principle there is sufficient signal for precise single shot temperature measurements using laser fluences around 10 mJ/cm^2 [15]. The frequency-tripled output of DPSS lasers, on the order of a few mJ, is sufficient to generate adequate laser fluences with light sheets 100's μm thick that are typically used in laser-based imaging experiments. DPSS lasers therefore provide sufficient pulse energy for temperature measurements using BAM:Eu, covering repetition rates up to 10's kHz. Considering the limitations that low laser energy imposes on scalar measurement techniques, outlined in chapter 2, this is a crucial aspect of the practical implementation of the measurement concept at kHz rates. DPSS lasers run continuously, which, when coupled with the capabilities of high-speed CMOS cameras, is a critical feature for long duration measurement sequences that cover a wide range of flow timescales. DPSS lasers are easy to operate and maintain, and can be readily purchased from a variety of manufacturers.

Also, BAM:Eu saturates. There is little increase in the luminescence intensity for laser fluences above 10 mJ/cm^2 [15]. Therefore the orders of magnitude higher pulse energy available using pulse-burst laser systems would not produce any significant increase in the temperature precision. These laser systems are technically complex, expensive, generally quite large and are highly specialised given the level of expertise required to design and operate them. This has limited their widespread use for flow measurements [8]. However, the abilities of pulse-burst systems are indispensable in two circumstances. First, the high pulse energy is essential for the application of some imaging techniques (e.g. planar Rayleigh scattering thermometry) at high repetition rates. For phosphor thermometry, this might be necessary if using a phosphor that only provides sufficient signal when using the 1-2 orders of magnitude higher pulse energy of low repetition rate solid-state lasers. Secondly, they are needed to extend most imaging diagnostics to repetition rates $>$ 100's kHz, because in this regime DPSS lasers do not provide sufficient pulse energy.

4.3 Cameras

For imaging, cameras consisting of a two-dimensional array (or chip) of individual pixels are used. Each pixel contains a photosensitive area, which is generally made from silicon. Photons possessing energies exceeding the bandgap generate a charge that is stored in the potential well of each photosensitive element. The charge accumulated is proportional to the number of photons striking the detector during the exposure time. This principle is the same for all cameras but the way in which they are designed and operated gives the device very different capabilities. Here some common terminology is outlined, before discussing specific types of sensor.

In addition to the photosensitive area, each pixel may contain or be placed beside other components. The percentage of the chip surface that contributes to the effective photosensitive area is termed the fill factor. Microlens (or lenslet) arrays placed in front of the chip are sometimes used to increase the optical fill factor. Microlenses (and also other protective windows in the camera casing) are usually made from borosilicate, for which the transmission drops sharply below 350 nm; and the surface reflectance of silicon increases toward the blue and ultra-violet, so image intensifiers are needed for imaging at these wavelengths. These factors combine to give the effective quantum efficiency.

Usually a signal is registered even when no light is incident on the camera chip, because an offset voltage is applied to avoid negative signals. Additional thermally generated charge is also present in each pixel, but generally this 'dark' noise contribution is negligible for short (μs) exposure times. The offset usually consists of a fixed spatial pattern and can normally be removed by subtracting images recorded with the chip covered.

Accumulated charge is converted to a voltage which is then digitised by the analog-digital converter (ADC) to produce the final recorded value, termed the number of 'counts'. The ADC is adjusted to maximise the dynamic range between the read noise (see below) and the 'full well' of a pixel (the maximum number of electrons it can hold).

In the whole process of generating the final recorded value from the accumulated charge, or ‘reading’ the chip, there is a further random signal contribution. Different manufacturers use different terminology but here the combined effects of resetting the pixel before the next exposure and amplifier noise are termed the read noise. The read noise plays a critical role in detector performance and varies significantly between different types of camera.

In turbulent flows, short measurement times are required to avoid averaging over the fluctuating quantities. If the measured signal persists for a duration much longer than the turbulent timescales of interest, for example if using a phosphor with a long (ms) lifetime, gating capability is needed. When imaging scattered light (matching the laser pulse duration) or short luminescence signals (e.g. $< 1\ \mu$s), in principle long exposure times of several milliseconds can be tolerated because the persistence of the signal now determines the measurement duration. However, usually the contribution of background signals makes such an approach impractical. Even ambient lighting can lead to appreciable background signals. When imaging in a reacting flow, for example, flame chemiluminescence or blackbody radiation originating from soot will usually require shorter exposure times, unless interfering signals can be spectrally filtered.

Light incident on the chip during camera readout can generate additional charge because the mask on the charge storage areas is not 100% opaque (see below). This unwanted signal contribution is attenuated by a factor known as the extinction ratio. When imaging, for example, continuous sources with short exposure times, the background will be attenuated by the product of the extinction ratio (e.g. 2000:1 for the CCDs used in this work) and readout time. This can lead to ghost features in the image, characteristic of the light source and the readout pattern of the chip. For continuous background sources or intense signals outside the exposure, this contribution may be comparable to the signal accumulated during the exposure.

Therefore in all but the most idealised test cases some form of electronic gating around the microsecond scale and below is required to reject background. Some CMOS (complimentary metal-oxide semiconductor) and CCD (charge coupled device) devices offer this capability, as well as even faster gating provided by intensifier technology. In the following, the main features of these types of detector are summarised and comparisons are drawn between them. High frame rate cameras based on CCD/CMOS arrays are then discussed. Here the testing of high-speed cameras used in chapter 5 is reported. Signal-to-noise calculations are used to compare the performance of the different cameras used throughout this work. Intensifiers are also discussed to understand their disadvantages, particularly for high repetition rate measurements.

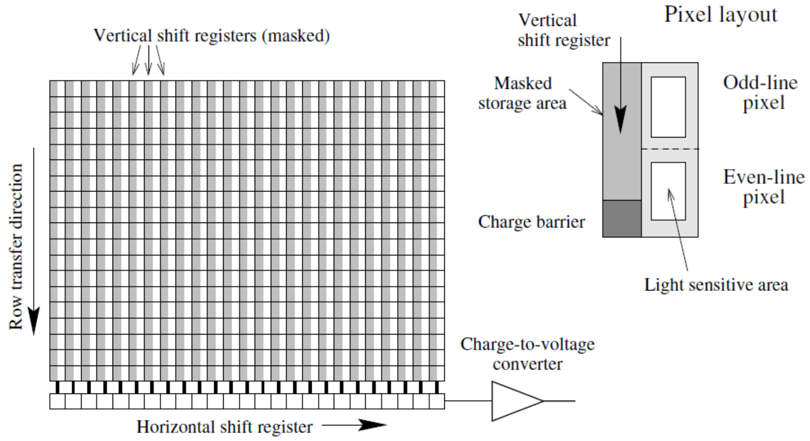

Figure 4.8: Interline transfer CCD. From [100].

4.3.1 CCDs

CCD refers to an architecture where the charge accumulated in each photosensitive pixel is sequentially transferred through storage areas to a location where charge is converted into a measured voltage.

Interline Transfer CCDs

For interline transfer CCDs each pixel is positioned beside a storage area that is permanently masked against light exposure, as shown in figure 4.8. Pixels are arranged so the photosensitive and masked areas alternately form rows or columns (depending on the chip architecture). This explains the terminology ‘interline’. An exposure is initiated by dumping the charge accumulated between acquired frames. At the end of the commanded exposure, charges are quickly transferred from the active region of each pixel to the respective storage area. Lines of storage areas are called shift registers, along which stored charges are transferred pixel-by-pixel to another readout register running along the edge of the chip. At the end of this shift register all charges are sequentially processed by the same charge-voltage converter and ADC.

There are several important features of this arrangement. The rapid shifting of charges to storage areas provides the inherent time gating capability of interline-transfer CCD cameras, where exposure times on the microsecond scale can be achieved. Each pixel is read with the same electronics (leading to the same gain, noise and linearity), but interline transfer CCDs are limited by the extended time taken for sequential readout of the pixels and so camera exposures cannot be (repeatedly) initiated and are limited to a low frame rate of around 10 Hz. Only some specialised CCD designs described below can be used for high repetition rate imaging.

These CCD cameras can be used for 'dual-frame' imaging, which is a particularly useful feature for PIV. After transferring the charge accumulated during the first exposure to the storage area, a second frame can be acquired, allowing a time separation between frames shorter than 500 ns. The exposure of the second frame matches the time taken to read out the first frame. Only after this is completed can the exposure of the second frame be ended by transferring charge to the register. The consequence is that the exposure time of the second frame is several orders of magnitude longer than the first. Although for PIV the effective exposure is determined by the laser pulse, this extended second exposure may contain a significant background contribution which must be suppressed using a narrow bandpass filter centered on the PIV laser line.

Typically for scalar measurements the resolution achievable using CCD cameras at full-frame is significantly better than that required, and would ordinarily be smoothed to reduce the influence of noise. The full-frame resolution is also normally larger than the minimum achievable laser sheet thickness, and the resolution of the scalar field need not be larger than the typically lower resolution of the PIV vector field. Therefore, the resolution can be reduced using some kind of averaging.

Some CCD cameras have the ability to read the total charge from a group (e.g. 4 x 4) of pixels, termed hardware binning. This effectively averages the accumulated charge on the chip (e.g. reduces the resolution from 1,376 x 1,040 to 344 x 260). Each binned pixel is only clocked once, which has the benefit of increasing the ratio of signal to read noise. This is a feature of great importance for low light level applications. Also, readout time is reduced and less memory is required for data storage.

4.3.2 CMOS

The primary difference for CMOS arrays compared with CCDs is that the charge-voltage conversion is performed in each pixel, shown in figure 4.9. For CMOS configurations with time gating capability, every pixel contains electronics that enable removal of charge accumulated in the photosensitive region outside the commanded exposure, and rapid charge transfer to a storage area at the exposure end. During readout, stored charges are sequentially converted to voltages in each pixel. Digitisation is often performed by several ADCs, each of which addresses a number of pixels. Because the readout time is not limited by a single charge-voltage converter and ADC as with interline transfer CCDs, CMOS technology

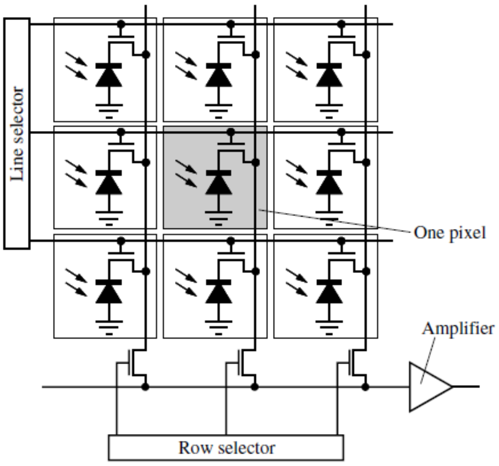

Figure 4.9: CMOS sensor. From [100].

can achieve high frame rates. Due to their design, some CMOS cameras are associated with spatial variations in fixed-pattern offset, overall non-linearity and pixel-to-pixel differences in sensitivity, gain and linearity [48].

sCMOS

sCMOS (‘scientific’ CMOS) cameras are a type of CMOS camera launched in 2009/2010. The main advantage of sCMOS technology is the exceptionally low read noise. They use just two digitisation channels and therefore like CCDs they are limited in frame rate (e.g. 50 Hz full-frame). They can be also be used in dual-frame mode for PIV, where the second exposure is limited by the time taken for digitisation.

4.3.3 High-Speed Cameras

Both CCD and CMOS sensors can be implemented in high-speed cameras. The use of CMOS sensors depends on the camera electronics, but CCD sensors must be integrated into a different system or adapted to achieve high speeds.

High-Speed CCDs

There are two approaches to high-speed imaging using CCD technology. One uses multiple intensified CCD chips and a system of beamsplitters or prisms to direct light toward them, with the advantage that very high (> 100’s MHz) frame rates with high (> 1 megapixel) resolution can be achieved [117]. Disadvantages are that the signal to noise ratio is compromised by the multiple reflections and use of intensifiers, and the high cost of these cameras.

Alternatively a single specialised CCD chip can be used. Each pixel contains multiple storage areas, so high frame rates can be achieved by successively shifting charge into these areas before ending the recording sequence and reading out the whole chip. These large pixels are comprised mainly of the storage areas, and so signal and resolution (e.g. 312 x 260 pixels) are sacrificed, though frame rates of $\sim$ 1 MHz are achievable [118].

The main point is that both types of high-speed CCD are limited by either the number of chips or storage areas in each pixel, and so typically the number of frames per sequence is 100 or lower. This is difficult to improve.

High-Speed CMOS

Because charge conversion is done at the pixel level in CMOS sensors, using multiple ADCs (e.g. 64, 128) the readout time can be reduced significantly. While a 1 megapixel CMOS sensor can be used at frame rates of 10's kHz, for higher speeds (up to $\sim$ 1 MHz) the number of read pixels must be reduced accordingly (to e.g. 128 x 32 pixels) [119].

Frame rate and resolution aside, CMOS cameras have two advantages in the context of high-speed imaging. Firstly, for the high-speed CCD-based cameras described above, the length of the recording sequence is indirectly limited by the readout time. More charge storage areas or extra chips have to be added to circumvent this problem, but this approach is inherently restricted. The record duration of high-speed CMOS cameras is only limited by memory. This is built into the camera (e.g. 64 Gb), so that long duration (several seconds) measurement sequences consisting of thousands of frames can be recorded.

Secondly, for high-speed CCD cameras the start of the acquisition must be commanded in advance. In high-speed CMOS cameras the memory is continuously overwritten, so the acquisition can be triggered retrospectively. It is this feature that permits the capture of rare or specific flow events, such as flame extinction or propagation (see chapter 2), with a high success rate. The memory can also be partitioned and acquisition can be synchronised to capture frames during a specific part of a repeating cycle, for example the compression and early expansion strokes of an IC engine [24]. This increases the number of frames containing the flow of specific interest, further extending the capability of these cameras to rapidly accumulate statistics.

It should be noted that these features rely on the ability of DPSS lasers to operate continuously. Long measurement sequences covering a wide range of flow timescales require laser systems that operate for the whole sequence. The post-triggering capability of high-speed CMOS cameras, which enables the capture of rare events, is only useful because these lasers run continuously.

4.3.4 Image Intensifiers

An image intensifier is principally a light amplification device. Intensifiers can be integrated with a sensor array, or bought as a separate unit that must be coupled to the sensor.

Incident light is imaged using a lens onto the photocathode, generating photoelectrons. Generated electrons are accelerated toward a microchannel plate (MCP), across which a high voltage is applied. The electric field of the photocathode can be switched to attract electrons toward the MCP or retain them. The MCP contains hundreds of channels within which secondary electrons are generated (typically thousands per input electron). The amplification process depends on the applied MCP voltage ('gain'). Electrons exiting the MCP are accelerated toward a phosphor screen, generating photons (typically hundreds per incident electron). This luminescence emission is then coupled to the sensor generally using a tandem lens or fibre coupling system. These basic components are shown in figure 4.10. The schematic is actually that of a three-stage high-speed intensifier (see below).

An S20 photocathode offers superior UV sensitivity to silicon sensors and so intensifiers are often used to image UV signals. Fast switching of the photocathode voltage also enables gating down to the nanosecond scale, using a nickel coating on the photocathode to allow fast charge and discharge. The switching of the photocathode voltage gives intensifiers the advantage that the extinction ratio is orders of magnitude higher than for CCDs and CMOS cameras, and completely attenuates background light sources outside the intensifier exposure time. Phosphors with high efficiencies and a green emission that peaks in the region where the sensor quantum efficiency is highest are preferable. The exposure time of the sensor must be long enough to detect the whole luminescence emission, but the actual exposure time of the measurement is determined by the voltage pulse applied to the photocathode.

Intensifier technology has several disadvantages. Thermally-generated electrons in the photocathode and MCP are also amplified and the amplification process itself possesses some statistical uncertainty: these contribute to a significant drop in the signal-to-noise ratio. The multiple components in the intensifier tube, particularly the MCP, leads to a loss in resolution [120]. Consequently, intensifiers tend to perform better than unintensified CCD or CMOS cameras only in

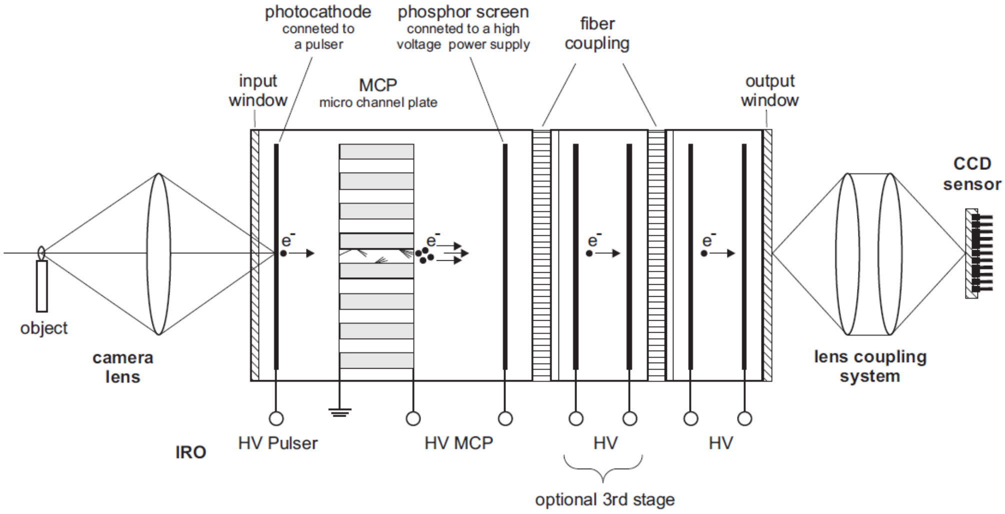

Figure 4.10: Three-stage high-speed intensifier. Additional photocathode/phosphor screen amplification stages are added. This allows lower MCP gain, reducing charge depletion effects. From [122].

extremely low light level conditions where the gain can be increased to overcome the detector read noise [121]. In this regime the signal-to-noise ratio is typically too low for quantitative imaging. Therefore their use is only considered useful for detection, UV imaging or where exposure times $<$ 100's ns are required. They may also be required in cases where the poor extinction ratio of CCD and CMOS cameras does not sufficiently attenuate light sources outside the exposure.

High-Speed Intensifiers

Intensifier design must be altered for high frame rates or for 'dual-frame' intensifiers used for two-line techniques. First, a rapidly decaying phosphor must be used. The cerium-based YAG:Ce (P46) phosphor has a decay time of 100's ns but a relative quantum efficiency of 30 % compared to the Gd_2O_2S:Tb (P43) phosphor used in low-speed devices. This can be compensated for with additional amplification stages as described below.

Secondly, depending on the input signal and gain, signal amplification partly or completely removes the MCP charge. The recharge time of a depleted MCP can take several milliseconds and so at high frame rates the MCP does not have time to be fully recharged between frames. This phenomenon, referred to as charge depletion, means for example that when illuminating the chip with a constant irradiance the recorded signal will decrease during the recording sequence. The gain of the MCP can be kept lower if additional amplification stages are added, using further pairs of photocathode and phosphor screens after the MCP connected using fibre couplings as shown in figure 4.10. This reduces the recharge time at the expense of a further loss in resolution.

Charge depletion effects in commercially-available two-stage high-speed intensifiers (High-Speed Intensified Relay Optics, LaVision) were studied by Weber et al. [48]. The severity and temporal persistence of charge depletion effects were found to depend on the frame rate, gain and overall irradiance, as well as the specific intensifier unit. For some combinations of parameters, depletion stabilises and it is common practice to discard thousands of frames from the start of each recording sequence to reach steady state e.g. [43–45]. A critical point is that depletion effects are likely to be localised [48]. The recorded intensity will depend on the signal at that spatial location in the previous frame (s). It has been suggested that an inter-frame referencing method would be required for correction [37], to adjust every recorded signal by some function of the intensity recorded at the same spatial location in previous frames.

The Weber study also reported severe non-linearities of up to 35% depending on the gain and specific intensifier unit, and also up to 5% variation in the pixel-to-pixel linearity of the whole system. For quantitative measurements, such large variations require that either the intensifier unit is characterised and operated in a limited regime where the system behaves almost linearly, or that a comprehensive evaluation is performed to relate recorded intensity to the input signal for each camera used.

Since parameter-specific pixel-to-pixel corrections must be applied, or the device must be used in a limited regime determined for each experiment, quantitative interpretation of images recorded using high-speed intensifiers is extremely complicated. Future work should focus on characterisation of local depletion effects to address this currently unknown source of measurement error.

4.3.5 Camera Comparison

Table 4.3 compares commercially available interline transfer CCDs and sCMOS cameras, supplied by LaVision. Both cameras have microlens arrays to increase the effective photosensitive area so the quantum efficiency (QE) is similar. The pixel size is the same but the sCMOS sensor has more pixels, so the sensor is much larger. The ratio of signal to read noise can be increased by hardware binning the CCD camera (typically 4 x 4 i.e. 344 x 260 25.8 x 25.8 μm pixels).

For high-speed CMOS cameras the electronics are different and typically operated at faster rates. Read noise is linked to the frame rate [121] so a camera

	CCD	sCMOS	CMOS
bit depth	12	16	12
QE % (at 450 nm)	60	45	30
chip size (h) x (v)	1,376 x 1,040	2,560 x 2,160	1,040 x 1,040
pixel size (μm)	6.45	6.5	20
read noise e^-	6	3	39
hardware binning	y	n	n

Table 4.3: Camera specifications.

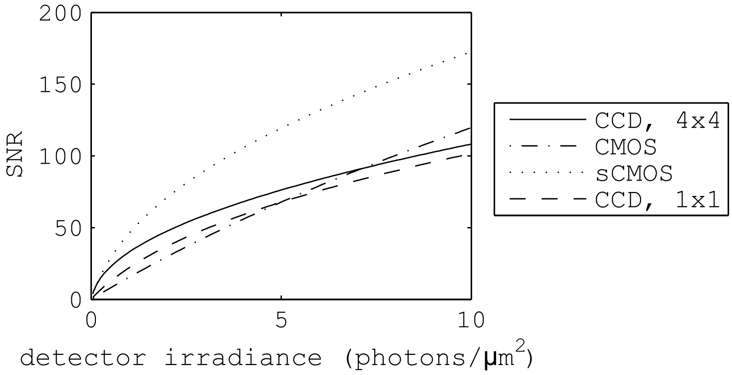

Figure 4.11: Simulated SNR for realistic signal levels using different cameras.

designed to operate at higher frame rates e.g. the high-speed CMOS (Fastcam SA4, Photron) compared in table 4.3 will typically have a higher read noise than low speed cameras. The pixels are larger and although for CMOS detectors the effective quantum efficiency increases with pixel size [120], the high-speed CMOS does not have a microlens array and the quantum efficiency is lower.

In principle the parameters listed in table 4.3 determine the the noise-limited performance of the camera. Considering the difference in read noise, for the same number of photons/pixel the high-speed CMOS would require around an order of magnitude more signal to match the performance of the low speed cameras. However, the size of both the pixels and overall chip have a big impact on the camera performance.

Signal-to-noise ratios (SNR) were simulated using the data in table 4.3. A range of signal photons n_p that produce similar signals in terms of counts to those measured in typical experiments (using the known quantum efficiency η and ADC factor) were considered. The signal $n_p\eta$ to noise σ ratio is calculated using the sum of squares of the shot noise $\sqrt{n_p\eta}$ and the read noise n_r:

$$\sigma = \sqrt{n_p \eta + {n_r}^2} \tag{4.4}$$

Figure 4.11 shows predicted SNR against irradiance at the detector, considering the same field of view and resolution in the measurement plane. The profiles of all curves indicate the influence of read noise, where at low light levels this noise source significantly contributes to SNR. For each camera the gradient decreases as operation approaches a 'shot-noise limited' regime where the SNR increases with the square root of the signal.

Effectively, comparing the CCD for unbinned and hardware-binned (4 x 4) operation shows the benefits of increasing the pixel size. Larger pixels collect more light, increasing the ratio of signal to read noise.

A larger chip permits the camera to be positioned nearer the measurement plane for the same field of view, increasing the light collection. This increased signal is distributed over a larger chip so that for the same f-number optics, the irradiance at the detector is the same. The benefits of a larger chip can be seen by comparing unbinned CCD and sCMOS cameras, which have a similar read noise and pixel size. The intrinsic SNR of each pixel is approximately the same but because of the higher resolution of the sCMOS chip many more pixels can be averaged over for the same final resolution, leading to a better overall SNR. This differs from a previous analysis where camera performance was compared at constant magnification, which masks the benefit of chip size [16].

Therefore, the larger pixels and overall chip size of the high-speed CMOS camera means that with increasing signal levels the performance approaches and even exceeds that of a low-speed binned CCD camera.

This theoretical simulation provides an indication of the noise-limited performance only. As noted above, CMOS sensors are associated with non-linearities and variation in fixed-pattern offset, which can also affect the measurement. In the following section the high-speed cameras used in chapter 5 are characterised.

4.3.6 High-Speed CMOS Characterisation

The use of high-speed cameras for quantitative measurements has previously been investigated using Fastcam SA1.1 cameras (Photron) [48]. The camera gain was found to decrease with increasing signal, such that the overall nonlinearity is less than 5% over the maximum dynamic range of the camera. The pixel-to-pixel variation in gain was within 1%. These results are shown in figure 4.12. In this work, similar high-speed cameras were used. Based on preliminary measurements of phosphorescence signals from seeded BAM:Eu particles using these cameras, recorded intensities were below 500 counts. Therefore overall nonlinearity and

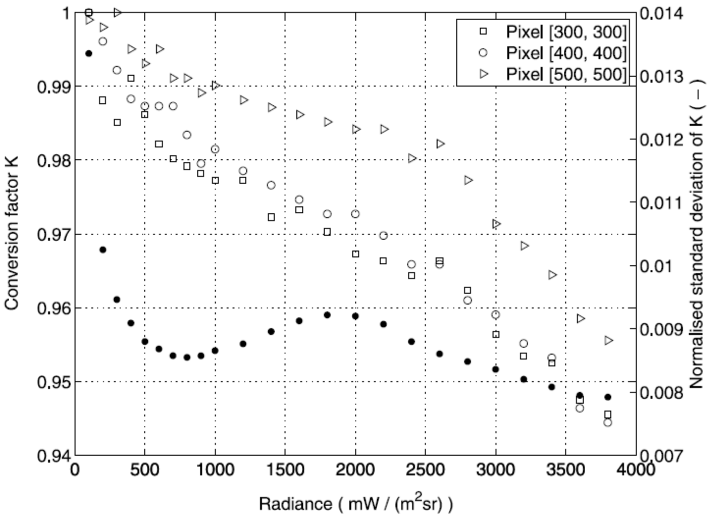

Figure 4.12: Gain (K) against radiance for a high-speed CMOS camera (Fastcam SA1.1, Photron), from [48]. The gain factor for three different pixels are shown; the solid dots are the normalised pixel-to-pixel standard deviation of the gain factor.

pixel-to-pixel gain variation would be expected to have a small impact on the accuracy and precision of the temperature measurement.

A series of experiments were conducted to directly investigate the effects of nonlinear sensor response on the measured intensity ratio. The two-camera system used for thermometry consisted of two high-speed CMOS cameras (Fastcam SA5, Photron) arranged in a beamsplitter configuration (section 4.4.1) and fitted with interference filters (section 4.4.3). The whole system was investigated by imaging different light sources, processing and dividing image pairs (section 4.5.1) and calculating appropriate statistics of intensity ratios obtained for different illumination conditions.

Firstly, to check linearity characteristics a BAM:Eu phosphor pellet was placed behind two diffusive glass screens and illuminated by the third harmonic (355 nm) of a pulsed Nd:YAG laser. Two different pulse energies of the laser were used to cover a range of recorded intensities between 20 and 500 counts. Secondly, to characterise the frame-to-frame stability a stable tungsten halogen lamp (LS-1, Ocean Optics) was placed behind the screen.

These cameras display a fixed-pattern offset of hundreds of counts, which must be subtracted. The camera supplier provides an intensity calibration feature, based on an acquired dark image, to correct for the large non-uniformities in this offset and reduce its magnitude. This was disabled for the present study since it modifies the gain after each calibration [48], which would otherwise introduce the requirement of a new temperature calibration after every use of this calibration feature, which must be avoided for repeatability. Instead, a manual background subtraction was performed. As noted in other studies [48], thermal drift of this offset was observed and so (as in all experiments) the cameras were switched on and left to stabilise over several hours. All images were recorded using the two-camera system at a repetition rate of 3 kHz to exclude effects of different recording frequencies on camera performance.

Linearity

When imaging phosphorescence using the given filter combination, the value of the intensity ratio is 0.2 at room temperature. Therefore, nonlinearity will be reflected by differences between ratios obtained at different illumination levels, obtained using different laser energies. Pixel-to-pixel variations in gain will be reflected in spatial variations when dividing two ratio images. To decrease the influence of statistical noise, an average of 100 single shots was compiled for each illumination level.

Considering a homogeneously illuminated region of 600 x 600 pixels, the spatially averaged ratio at each illumination level differed by less than 0.1%, indicating that the nonlinearity is negligible in this range of intensity. The pixel-to-pixel standard deviation of the divided ratio images was 3.1%. Both findings are in good agreement with the previously mentioned study [48], when propagating the uncertainties for comparison with the divided ratio image evaluation used here. No smoothing was applied in this analysis, but it was found that the spatial variation in pixel gain was reduced to 0.6% after the images were processed as in chapter 5, so no image correction is necessary for actual gas-phase experiments.

Frame-to-Frame Stability

A sequence of images of the stable light source was recorded. Based on a homogeneously illuminated region comprised of 50 processed pixels in the centre of each intensity ratio image, the frame-to-frame standard deviation of the spatially averaged ratio was found to be 1.5%. This is larger than the single shot pixel-to-pixel standard deviation in the same area (0.7%), indicating these frame-to-frame fluctuations are an order of magnitude larger than the 0.1% expected when considering a statistical distribution of the sampled mean. Further investigation revealed this effect was isolated to one camera, which produced the significant frame-to-frame fluctuation in intensity ratio. However, this behaviour was not consistent on a day-to-day basis and for some recording sequences the fluctuation was barely detectable. This error was therefore considered a fault of this specific camera.

Frame-to-frame variation of the overall intensity ratio results in an overall change in the mean measured temperature between frames, which must be corrected. A procedure for this is given in chapter 5.

4.3.7 Discussion and Summary

For imaging at low frame rates, comparison of the sCMOS and hardware-binned CCD showed that the sCMOS offers superior performance and will improve the measurement precision. However, for facilities where there is a larger minimum distance between the measurement plane and cameras, or for smaller measurement regions, a camera with a larger chip will either require long focal length optics (where the f-number is higher, reducing light collection), or decreased magnification at the expense of wasted chip resolution. A hardware-binned CCD would then offer performance closer to that of an sCMOS camera. Interline-transfer CCDs, and later the sCMOS cameras compared in this section, were used throughout this work.

In terms of functionality CMOS technology offers clear advantages for long-duration high repetition rate measurements. The simulation indicates that the relative performance of high-speed CMOS cameras and low-speed hardware-binned CCDs depends on the signal level. This is due to read noise. For low signal levels the low-speed system will perform better. Linearity and stability issues were experimentally characterised and shown to be suitable for quantitative measurements. High-speed camera technology is improving rapidly, with increasing effective quantum efficiencies (increased fill factor) and also frame rates at full resolution.

Other factors may contribute to the camera performance. Linearity data provided by the manufacturer may only be tested for a limited part of the total dynamic range. As shown above read noise is critical but values may not be as quoted and vary between different generations of camera. Particularly for low-light level applications, proper background subtraction, and therefore offset stability, is important. Other sources of noise not accounted for and further onboard treatment of sampled voltages would be included in measurements of ISO speed ratings (ISO 12232) but this information is not always available from manufacturers. Therefore prior testing of cameras is often necessary, and for intensified camera systems a prerequisite for quantitative measurements using for example a stable, calibrated light source and an integrating sphere to achieve uniform irradiance of the sensor.

The cameras discussed here are suitable for imaging visible luminescence signals, as is the case with many thermographic phosphors. Therefore, intensifiers are not required, which leads to improved resolution and SNR. The discussion of high-speed intensifiers shows that this is a critical advantage at high repetition rates where their use makes quantitative imaging very difficult.

4.4 Setup for Intensity Ratio Imaging

The previous section identified cameras suitable for thermometry. This section covers how these cameras are implemented for practical measurements. The camera arrangement, lenses, and optics used to filter and separate the two detection channels used for the two-colour approach are discussed in turn.

4.4.1 Camera Arrangement

As highlighted in chapter 2, often different planar measurement techniques are applied simultaneously. These images have to be overlapped, so the field measurements of for example velocity and OH radical concentration are matched in physical space. However, scalar measurement techniques using two-colour or two excitation wavelength imaging actually requires the mathematical division of two simultaneously (or quasi-simultaneously) acquired images. In this case the intrinsic measurement precision depends in part on the precise superposition of the two acquired images.

This technique involves the unique requirement for the division of two particle luminescence images. The distribution of intensity in an instantaneously acquired particle image fluctuates with a high spatial frequency due to the inherent nature of imaging seeded particles. This is a very different situation to imaging homogeneously distributed tracers used for LIF techniques. The following measurements and discussion show that the way in which the particle luminescence is detected is especially important in this case.

In the literature several approaches have been used to simultaneously capture two spectrally filtered particle images. These methods, shown in figure 4.13, were tested in this work, and common advantages and disadvantages of each are discussed here.

Stereoscope

A stereoscope (or image doubler) consists of two mirrors and a prism (see figure 4.13), fitted onto the camera lens, that allows simultaneous imaging of the area of interest onto a single CCD chip. Mechanical vignetting of light occurs due to the prism and mirrors, which reduces the collection (effective f-number) and also produces a strong gradient in intensity across the imaged field. This effect is reproduced in reverse through the other aperture. After division of the two

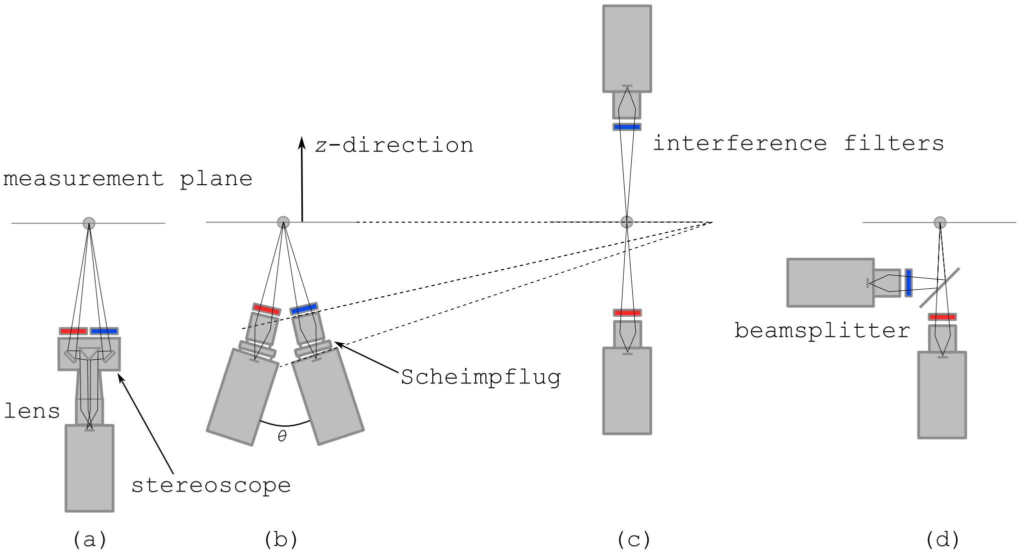

Figure 4.13: Camera setups for intensity ratio imaging. (a) stereoscope; (b) stereo setup with two Scheimpflugs; (c) cameras positioned on opposite sides of the measurement plane; (d) beamsplitter arrangement.

images, this produces a steep horizontal gradient in the intensity ratio field. This can affect the dynamic range of the temperature measurement.

The most critical problem arising from the use of stereoscopes is cross-talk. This is due to light originating from regions adjacent to the field of view which is transmitted through each aperture onto the opposite side of the chip. This means that a source of light present outside the field of view interferes with the measurement. At maximum aperture, the cross-talk contribution was measured to be up to 35% of the total signal. In almost all practical applications, there will be luminescence from particles illuminated by the laser sheet outside the field of view. This contribution cannot be subtracted and the stereoscope cannot be used. This cross-talk decreases when closing the aperture, but this drastically reduces the amount of collected light. Only by stepping the aperture down to f/16 can cross-talk be completely suppressed, corresponding to two orders of magnitude less light.

Due to the reduced resolution and compromised signal, the stereoscope configuration is considered unsuitable for ratio-based imaging.

Stereo Imaging

Using stereo arrangements, e.g. two cameras positioned next together, planes imaged through each aperture are at an angle to the laser sheet and also at opposite angles to each other. This leads to off-axis defocusing and a difference in

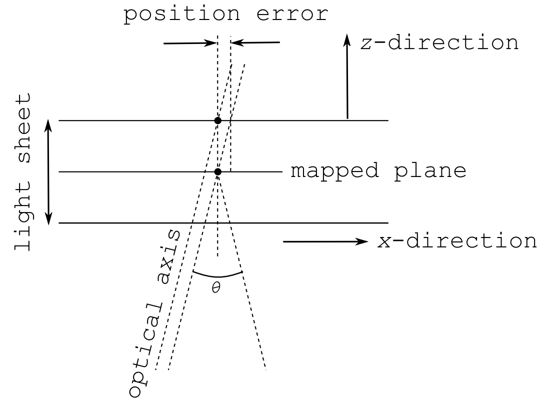

Figure 4.14: Perspective error using a stereo arrangment. The two particles are physically located in the same x position, but the particle at the back of the light sheet appears in a different x location in the image plane, and will not be corrected properly using a mapping procedure applied in the centre of the light sheet.

magnification across the field of view. Scheimpflug adaptors are used so that the subject, lens and image planes meet at a common point as shown in figure 4.13. This allows elimination of off-axis defocusing. This arrangement also provides full resolution and in principle no loss in signal.

To correct for the difference in magnification across the field of view, and also for rotation, translation and other distortion, a procedure (see section 4.5.1) must be used to map pixels from the image to object planes, allowing superposition of each image. The laser light sheet has a finite thickness, typically 100's μm, but the mapping procedure is applied at some specific point along the optical axis (z-direction in figures 4.13 and 4.14), for example in the middle of the light sheet.

Using a stereo arrangement, particles are located at a different position in the image plane depending on their z position within the light sheet. Therefore only particles located in the plane in which the mapping procedure is applied will be registered to a common location in each mapped image. This is illustrated in figure 4.14. The effect on the measurement precision was quantified in a series of experiments, as described below.

Opposing Camera Arrangement

Positioning the cameras on opposite sides of the measurement plane eliminates this problem. The entire field of view is imaged in focus and with uniform magnification, and in principle the only mapping procedure required is to horizontally flip one of the images prior to division. However, in this configuration, the filter of each camera reflects particle phosphorescence toward the opposite camera and interferes with the intensity ratio measurement. Also, this arrangement cannot be used for measurements in facilities with optical access from only one side.

Beamsplitter

An issue common to all three of the schemes discussed above is that the collection paths for each channel are different. Therefore any differences on the optical path between the measurement plane and each camera, such as deposits on windows, will interfere with the ratio measurement.

When using two cameras in a beamsplitter arrangement, as shown in figure 4.13, the detection path is the same. By positioning one camera on a labjack and two translation stages, translation and magnification can be corrected and rotation can be accounted for by altering the vertical angle of the beamsplitter. This not only removes any optical mismatch between the two detection paths, but permits manual alignment with a degree of accuracy that enables direct division of the raw images prior to any software image mapping. This is discussed further in section 4.5.1.

A practical point is that like most optical setups the camera alignment is sensitive to small movements. An advantage of the elimination of the software dependency also allows the alignment to be checked online during measurements.

Setup Comparison

A series of measurements were conducted to evaluate the benefit of using the beamplitter setup and characterise the error when using stereoscopic imaging setups (stereoscope or two-camera systems). This was done by imaging the intensity ratio field in a turbulent jet with each setup.

2 μm BAM:Eu particles (KEMK63/UF-P2, Phosphor Technology) were seeded into a room temperature jet of air. The frequency-tripled output of a flashlamp-pumped Nd:YAG laser (NanoTRL, Litron) was formed into a laser sheet 700 μm thick in the measurement plane. Particle luminescence was detected using two sCMOS cameras (Imager sCMOS, LaVision) with 105 mm f/1.8 Nikon lenses in the two arrangements (b) and (d) shown in figure 4.13. The first arrangement (d) used a dichroic beamsplitter and interference filters (see section 4.4.3) to separate the two channels. In the second stereo arrangement (b) the full angle θ between the cameras was varied between 9° and 60° (see figure 4.13). In all cases the field of view (43 x 36 mm) was kept the same.

For each set of 100 images taken using each arrangement, images were corrected for background and matched using a dewarping algorithm based on images of a commercial calibration target (LaVision). Images were then binned 4 x 4, filtered

Setup	precision (%)
Beamsplitter	1.1
Stereo (9°)	5.2
Stereo (60°)	12.7

Table 4.4: Normalised single shot intensity ratio standard deviation using different camera arrangements.

(15 counts), and smoothed using an 11 x 11 moving average filter, for a final resolution of 700 μm. A normalised average intensity ratio image was used to correct for non-uniformity in light collection. From a region in the centre of each single shot image, the average intensity and normalised standard deviation of the intensity ratio was calculated. Further details of the image processing steps are given below in section 4.5.1.

Table 4.4 shows the intensity ratio precision for each setup, compared for approximately the same signal in each case. Even in the stereo arrangement where the cameras were positioned as close as possible to one another, the registration between particles imaged at the front and back of the light sheet either side of the dewarped plane (see figure 4.14) degrades the intensity ratio precision. In the case where the stereo angle is increased to 60°, this problem is exacerbated: the shift in particle position between each dewarped image is clearly visible. To reduce this error, the cameras must be positioned farther away from the measurement plane, reducing the light level and therefore the precision. The use of a beamsplitter setup is considered essential in maximising the precision of ratio-based thermometry.

PIV Camera

The PIV camera can be positioned on the opposite side of the measurement plane in open test facilities, using an absorption filter (colour glass) to ensure no particle luminescence is reflected back into the temperature imaging system. Alternatively a longpass beamsplitter to separate scattering and luminescence can be used. This allows all three cameras to be positioned on the same side of the measurement plane.

4.4.2 Lenses

Ordinarily for imaging diagnostics commercial camera objectives are used to form an image on the camera chip. These objectives are actually a series of lenses designed to minimise chromatic abberations (where different wavelengths are refracted by different amounts), spherical abberations (a difference in the covergence of light rays at the centre and toward the periphery of the lens) and astigmatism (different effective focal lengths in the horizontal and vertical directions). Lenses with low f-numbers are desirable to maximise luminescence collection e.g. 50 mm f/1.2. Where the cameras must be positioned farther from the measurement plane, longer focal length lenses are needed to maintain the same field of view. However, long focal length lenses tend to have a higher f-number, e.g. 105 mm f/1.8, 85 mm f/1.4, and have a large diameter. This requires either filters of the corresponding size, or more often an adaptor to step down to the filter size, tolerating some vignetting of light toward the peripheries of the image.

4.4.3 Filters and Sensitivity

For two-dimensional ratio imaging, filters that transmit parts of the spectrum that exhibit relative temperature-dependency are used. For interference filters, thin-film coatings with different refractive indices are deposited on the filter substrate with thicknesses on the order of the light wavelength, controlling the nominal wavelength and passband via constructive and destructive wave interference.

There are two basic requirements of the choice of filters: one, that they transmit as much of the luminescence emission as possible, and two, that they offer high sensitivity. The sensitivity is defined as *the change in the intensity ratio with temperature*. Given the inherent statistical measurement error, the temperature precision will increase with increasing sensitivity.

These two constraints are coupled in that a more sensitive filter combination will not necessarily improve the temperature precision: if the filters transmit less light the statistical error in the two intensity measurements will increase, leading to increased error in the intensity ratio. From the propagation of error, the standard deviation of the intensity ratio $IR = I_a/I_b$, where I is the transmitted intensity $n_p\eta$ (see section 4.3.5) in each channel, denoted by the subscripts a and b, is given by:

$$\sigma_{IR} = \frac{I_a}{I_b}\sqrt{\left(\frac{\sigma_a}{I_a}\right)^2 + \left(\frac{\sigma_b}{I_b}\right)^2} \tag{4.5}$$

where σ is the noise in each channel, from equation 4.4.

Equation 4.5 can be used to determine the intensity ratio precision for signal levels comparable to those measured in gas-phase experiments, adjusted to account for the relative transmission of the filter combination. Spectrally-resolved data can be also used to evaluate the temperature sensitivity at each temperature, by digitally integrating the spectrum using filter transmission profiles. With both the intensity ratio precision and the temperature sensitivity, the temperature error can

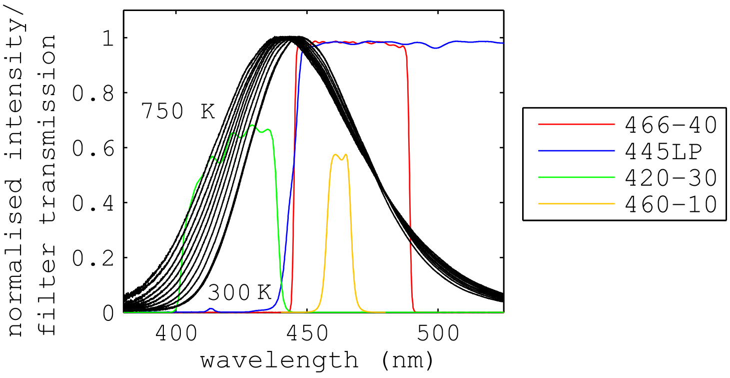

Figure 4.15: Normalised emission spectrum of BAM:Eu between 300 - 750 K (50 K temperature intervals). Filter/beamsplitter transmission profiles (provided by the manufacturers) shown in colour.

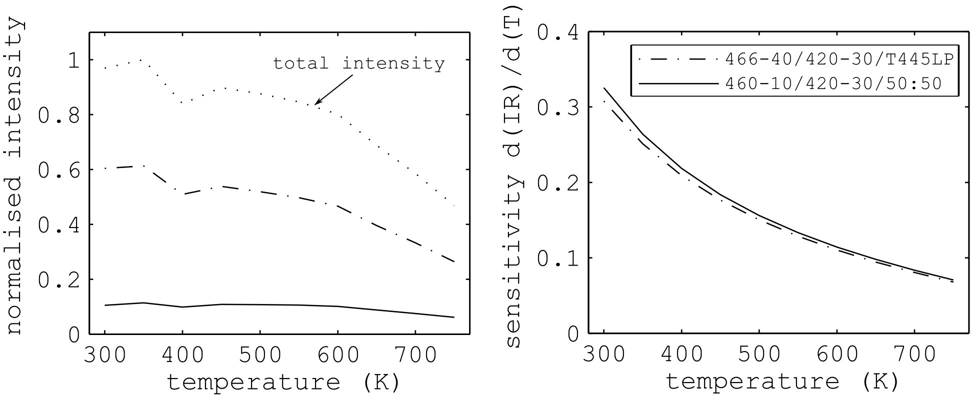

Figure 4.16: Left: Integrated emission intensity of BAM:Eu for two different filter combinations. The unfiltered emission intensity is also shown. Right: Normalised temperature sensitivity with temperature ($\%IR$/K) for the two filter combinations.

be predicted for different filter combinations.

In earlier work using the phosphor BAM:Eu [15], 460-10 (67899, Edmund Optics) and 420-30 (D420/30m, Chroma Technology) inteference filters were used (notation central wavelength, full-width at half-maximum), in conjunction with a 50:50 beamsplitter, with an anti-reflective (AR) coating on the reverse side to avoid ghost reflections (46642, Edmund Optics). The normalised emission spectrum of BAM:Eu and the filter transmission curves are shown in figure 4.15.

There is a possibility of improving the filters to increase the temperature precision. This is important for thermometry using BAM:Eu in general, and critical for kHz-rate measurements if signals are lower, because high-speed CMOS cameras are predicted to perform with a reduced SNR compared with low-speed CCDs.

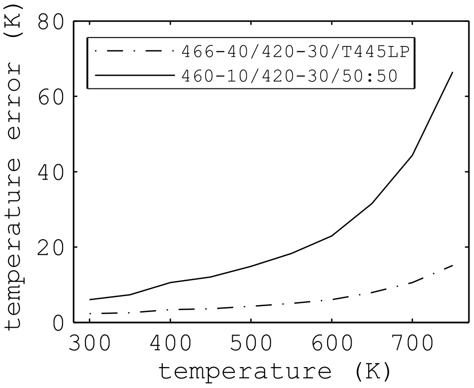

Figure 4.17: Simulated temperature error for the two different filter combinations.

The use of a dichroic beamsplitter that spectrally separates the two channels increases the signal in each channel by close to a factor of two. For this a longpass dichroic at 445 nm (T445LP, Chroma Technology) AR-coated on the reverse side was chosen, the profile of which is shown in figure 4.15. The narrow 460-10 filter was replaced with a 466-40 filter (86363, Edmund Optics), integrating × 5 more of the emission.

In the following, these two filter combinations are compared: the set 460-10/420-30/50:50 from [15] and the proposed set 466-40/420-30/T445LP. Figure 4.16 indicates the overall transmitted light of the two filter combinations and the total integrated emission (left) and the temperature sensitivity of the two filter combinations (right). Figure 4.17 indicates the temperature error, evaluated using the sensitivity and equation 4.5. This analysis assumes the use of the high-speed cameras analysed in section 4.3.5, for a signal the same as that measured in gas-phase experiments.

The decrease in signal transmitted by both sets of filters reflects the overall decrease in the emission intensity due to thermal quenching (figure 4.16 (left)). The new filter combination transmits $> 4 \times$ more light across the studied temperature range. This improves the precision in the intensity ratio, and since the sensitivity is approximately the same for both sets of filters (figure 4.16), the temperature error is significantly reduced for the new filter set (figure 4.17).

This benefit increases with temperature. As the luminescence signal decreases with temperature, the effects of camera read noise have an increasingly dominant role in the intensity ratio precision (and therefore temperature error). For low signal levels it is crucial to use filters that maximise the transmission of the luminescence emission. As signal levels increase toward the shot noise limited regime the relative benefit of improved sensitivity increases compared with higher signal transmission.

It should be noted that, for a given phosphor, the temperature precision cannot be arbitrarily increased, since a significant increase in the sensitivity may require filters with narrow passbands, decreasing the signal and therefore the intensity ratio precision. The importance of the inherent sensitivity of the intensity ratio response of phosphors is investigated in chapter 6.

Using these filter combinations the sensitivity of BAM:Eu decreases with temperature. A filter that extends the passband toward the UV below 400 nm will improve the sensitivity at higher temperatures. Also, a filter that integrates the peak between 435 nm and the edge of the transmission of the 445 nm long-pass filter used here increases the signal but decreases the sensitivity. Filters that avoid specific background sources (e.g. for BAM:Eu, lines of C_2 and CH chemiluminescence which might be prominent in combustion applications) are favourable and have been suggested in work by other research groups [123] but this is likely to severely limit the signal level. Therefore, when choosing filters a complete analysis is necessary, and must include the camera performance and realistic signal levels over the temperature range of interest.

One of the most important parameters is the optical density outside the passband of the filter, which must block light effectively at the laser wavelengths used for PIV and phosphor excitation. Optical densities > 5 were used in this work and were found to completely suppress scattered light. Further considerations include the surface flatness of the beamsplitter, specified in units of the light wavelength λ/inch. Thicker substrates permit better surface flatness, down to fractions λ/inch. Non-flat dichroics can cause aberrations including astigmatism and curvature in the reflected image, which would degrade the resolution and require correction. The scratch-dig specification relates to the surface quality, where lower numbers indicate improved surface quality. Beamsplitters used in this work have specifications < 6 λ/inch, 80-50 scratch-dig.

4.5 Image Processing and Calibration

Following acquisition, treatment of the luminescence image pairs is required. Background subtraction, image registration (dewarping), filtering and smoothing procedures are briefly described here, along with the white field correction. The concluding section covers the method for temperature calibration. Further details can be found in [16].

4.5.1 Image Processing Steps

Background Subtraction

Only particle luminescence that originates from the measurement plane during the exposure should be used for the temperature evaluation, and sources of background that contribute to a recorded signal must be identified (if possible) and subtracted. Particularly for low signal levels, the intensity ratio is sensitive to small variations in background which can lead to a temperature error if improperly subtracted.

As previously mentioned, usually there is a fixed-pattern offset for each camera that can be subtracted by recording images with the camera lens capped. The background should be regularly assessed to check that the offset of the camera does not drift in time.

Even if they can be easily evaluated and subtracted, background that originates from additional sources of light integrated during the exposure will degrade the measurement precision, due to shot noise of the background signal. Therefore avoiding sources of background light is preferable, and essential for cases where the background signal is of a similar magnitude to the signal itself.

In enclosed environments the most prominent source of background is likely to be due to phosphor particles deposited on surfaces that are excited by the laser. The number density of particles, once deposited on the surface, is much higher than that dispersed in the gas and so this background signal contribution may be orders of magnitude larger than the actual signal if steps are not taken to avoid excitation of deposited particles using the laser. When imaging beside surfaces it should be noted that this is still important, even if the surface is outside the field of view. The luminescence emission originating from the surface is so large that the point spread function of the optical system leads to a signal contribution in the image.

Image Registration

Accurate registration of images is required before division. In the case of the beamsplitter arrangement where distortion is minimised, it is possible to avoid any mapping procedure at all and only rotation, magnification and translation need be accounted for. In this case, manual alignment can be based on a target placed in the plane of the laser sheet. A coarse cross-correlation between each camera image can be performed using PIV software while grabbing images of the target. The residual displacement field is displayed live, greatly simplifying the manual alignment procedure.

Following alignment, the mean displacement across the whole image can be calculated using the cross-correlation algorithm. Using this alignment method, generally the residual error due to distortion can be reduced to, for example, ~ 0.15 4 x 4 binned pixels when using interline-transfer CCDs.

For distortion common to both images, like a pincushion effect, the images can still be divided, and then the intensity ratio image can be mapped after division. Otherwise in the case of differences in the two images that make manual alignment impossible (for example, subtle differences in magnification or other distortion), some form of software image mapping prior to division is required. This is achieved using images of a well-defined target, generally an evenly-spaced array of known shapes (e.g. crosses or dots) at least as large as the area of interest. The known physical spacing/geometry of the dots in the object plane is related to the imaged position of the dots (i.e. the calibration target image) in the image plane using a mapping function. Alternatively, a cross-correlation between the particle images themselves using PIV software can be used to find a mapping function to invert the displacement between the two images. For these procedures, a commercial dewarping algorithm and PIV software developed by LaVision were used. Further details on image mapping can be found in [16, 124].

Cutoff Filtering

Computing temperature information from pixels containing low numbers of counts will result in a noisy temperature field. Furthermore, the statistical distribution of sampled ratios is such that noise biases ratios toward higher values (for more details, see [16]). Therefore a cutoff filter is applied to the images prior to smoothing, to remove signals with a low number of camera counts.

The bias effect means that image pairs should always be smoothed to the final resolution and then divided, not the other way around.

Smoothing

Generally a moving average filter of a uniform size (e.g. 3 x 3) is used to reduce the effects of statistical noise. Sometimes, software binning of images is more appropriate, particularly using high resolution CMOS cameras that cannot be hardware-binned. Megapixel images demand a lot of storage space and are laborious to process, so reducing the image size is beneficial.

After this step the resolution of the imaging system can be evaluated, including effects of the applied processing steps. The geometric projection of a pixel in the measurement plane is not a suitable measure of resolution because of the various optical elements on the optical path (filters, lenses) which reduce the

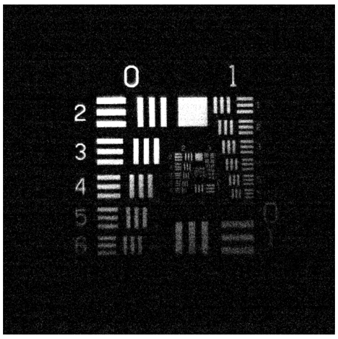

Figure 4.18: 1951 USAF resolution target, imaged using a high-speed CMOS camera.

actual resolution due to phenomena such as diffraction. Although the applied dewarping and smoothing steps might reduce the final resolution to an extent where these effects play a limited role, the resolution should be directly measured using equivalently processed images of a resolution target as shown in figure 4.18.

Groups of lines are printed on this target with a specified spacing (spatial frequency) r' in line pairs/mm. The modulation transfer function M_{TF} for a group of lines relates to the contrast between the maximum I_{max} and minimum I_{min} pixel intensities at locations on and between lines [100]:

$$M_{TF}(r') = \frac{I_{max} - I_{min}}{I_{max} + I_{min}} \tag{4.6}$$

The half-width σ of a Gaussian curve representing the imaged intensity distribution of a perfectly sharp point in the object plane is given by:

$$\sigma = \sqrt{-\frac{\ln(M_{TF}(r'))}{2\pi^2 r'^2}} \tag{4.7}$$

An alternative method is to image a sharply defined edge (e.g. a razor) placed in the measurement plane and fit a Gaussian profile through the pixel intensities in the vicinity of the edge to determine the line spread function. Using either of these methods, the full-width at half-maximum ($2\sqrt{2\ln 2}\sigma$), or at a contrast appropriate for the measurement, should be quoted along with the measurement precision.

For the temperature measurement, the resolution is determined from images recorded using a single camera. Given that the images are typically smoothed to a resolution significantly larger than the remaining misalignment between luminescence images, further loss in resolution caused by dividing two images for the intensity ratio is considered negligible.

The spatial resolution of the PIV measurement depends on the interrogation window size and the degree of overlap, such that the resolution lies between the vector spacing and the size of the interrogation window.

The spatial resolution is indicative of the accuracy with which the size of flow structures can be measured. For determining gradients and scalar dissipation, unbiased measurements can only be obtained for flow scales several times larger than σ [125]. Furthermore, a measurement that does not resolve the smallest turbulent scales will also contain an error if the function of the mean of the sampled quantity (in this case, a temperature calculated from an unresolved intensity ratio measurement) does not equal the mean of the function of the sampled quantity (i.e. a smoothed temperature calculated from fully-resolved intensity ratio measurements). This is true for non-linear relationships between the measured variable (temperature) and the sampled quantity (intensity ratio), and may be the case for this temperature measurement technique if there is a non-linear dependence of the sampled intensity ratio on temperature.

The use of smoothing reduces noise but degrades the spatial resolution, so the use of smoothing/binnning methods, and the design of the experiment itself, depends the flow under investigation and the specific quantities that are being measured. A discussion of flow measurement errors caused by finite imaging system resolution can be found in references [125, 126].

White Field Correction

Processed image pairs are divided to produce intensity ratio images, which require one further correction before calibration. The interference filter transmission profiles are sensitive to the incident angle of the luminescence emission. In an imaging configuration, the incident angle of off-axis points in the measurement plane varies spatially and so the effective transmission of the system changes over the field of view. The same effect arises when using a dichroic beamsplitter, which causes an additional left-right distribution across intensity ratio images.

A white field correction must be performed to correct for this spatial non-uniformity in light collection, which involves imaging a light source with the correct characteristics using the two-camera system. Intensity ratio images are then divided by this correction ratio image (white field), to leave the true intensity ratio distribution.

The correction does not need to be spatially uniform in intensity, but due to the angular dependence it must, like the luminescence signal from the particles, emit uniformly in all directions (i.e. Lambertian). Also, it must be the correct colour. For example, using a narrow line LED source for the correction will lead to an overestimation of the angular dependence because of the steep spectral gradients in

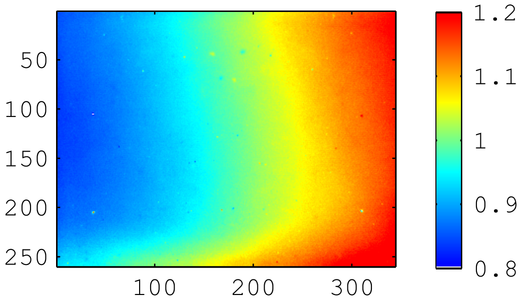

Figure 4.19: Typical white field image using a phosphor placed behind diffusive glass screens, recorded using two CCD cameras in a beamplitter configuration.

the vicinity of the edge of the filter passbands. The emission of the phosphor used in actual experiments is the correct colour, and a white field source comprising of a phosphor pellet, excited using the laser and placed behind two diffusive ground glass screens can be used to correct images [15]. An example white field image of this source, recorded using a two-camera/beamsplitter arrangement, is shown in figure 4.19. An alternative is to use a highly diffusive reflective material, which produces a Lambertian and spectrally uniform reflection of incident light. This can be positioned in the measurement plane and illuminated with luminescence appropriate for the phosphor used in the experiment.

A more practical alternative is to use an average intensity ratio image recorded using the luminescence of particles seeded into a uniform (typically ambient) temperature flow. The recorded field has all the required characteristics for the corrective white field, and would be imaged in most experiments anyway as part of a calibration procedure (see next section). This strategy was used in the experiments performed in chapters 5 and 6 of this work.

4.5.2 Temperature Calibration

Finally, intensity ratio images must be converted to temperature. One possibility to obtain the desired intensity ratio-temperature relationship is to use spectrally-resolved data, digitally integrated using filter transmission profiles, in a procedure the same as that used for the filter analysis of section 4.4.3. While this is appropriate for designing experiments, it cannot be used for calibration due to the angular-sensitivity of the interference filters. The transmission profiles are slightly broadened toward the UV even for a point directly on the optical axis because non-collimated light is imaged through each filter over a range of angles. Even if this effect was characterised with certainty, the absolute intensity ratio and the temperature response would still depend to some extent on the specific experimental setup.

In-flow calibration procedures are therefore required. For intermediate temperatures, an electrically-heated jet of phosphor-seeded air is probed using the temperature imaging diagnostics. In a constant-temperature region of the flow that remains completely unmixed with surrounding air (the jet potential core), average intensity ratios can be computed for stable exit jet temperatures. These ratios are calibrated against temperatures sampled using fine-gauge thermocouples positioned in the measurement plane at the same spatial location used to compute the intensity ratio. A fit of temperature to intensity ratio is then used to evaluate intensity ratio images recorded in experiments.

This does require that a temperature-controlled flow can be set up in the measurement domain, or established by other means in larger facilities using for example air preheaters, or laminar flames for calibration at high temperatures. Alternatively, the temperature can be calculated from known parameters. For example, a procedure in an IC engine might use simultaneous ratio measurements and polytropic compression relationship to determine the calibration curve as in for example [44, 45].

The accuracy depends on the fit and the accuracy of the thermocouple measurements. The in-flow calibration system lends consistency to a single measurement campaign or set of measurements: systematic errors are revealed by repeated calibration sequences. Data retrieved from calibration measurements can also be used to evaluate the temperature precision as described in the next chapter.

5 kHz-Rate Temperature and Velocity Imaging: Demonstration and Results

The previous section identified lasers and cameras suitable for the extension of the technique to high repetition rate imaging. This chapter demonstrates the implementation of this system and characterises the measurement precision.

5.1 Experimental Setup

Test Cases

Initial measurements were conducted in a turbulent jet ($Re \sim 10,000$) of air (21 mm nozzle diameter, velocity 7 m/s) surrounded by a room temperature co-flow (80 mm diameter, velocity 0.5 m/s). The flow could be electrically heated using a 1256 W heating tape (STH 102-080, Omega Engineering) wrapped around the delivery tube.

In a second demonstration study, the central nozzle was removed and a pipe of 6.25 mm diameter heated to 530 K was positioned horizontally above the co-flow as shown in figure 5.1. The free stream velocity was set to 1.6 m/s so at a temperature of 293 K the Reynolds number was $\sim$ 700, resulting in irregular vortex shedding in the wake of the cylinder [127].

In both test cases presented here, the gas streams were seeded with 2 μm BAM:Eu phosphor particles (KEMK63/UF-P1, Phosphor Technology) using reverse cyclone seeders. The particles were treated with a Ludox coating and were dried overnight at 125 °C in a furnace before use.

Temperature Imaging

For thermometry, the phosphor particles were excited using the third harmonic of a diode-pumped Nd:YAG laser (Q301, JDSU). The experiments were performed at 3 kHz. At this repetition rate the power output at 355 nm was measured to be 4 W (1.3 mJ/pulse), with a measured pulse duration of 25 ns. The beam was expanded using a Galilean telescope of f = -50 mm and +250 mm lenses and then formed into a 600 μm thick and 50 mm high light sheet using f = -50 mm and +500 mm cylindrical lenses.

The phosphorescence emission was detected by two non-intensified CMOS cameras (Photron SA5, 12 bit, 1,024 x 1,024 pixels), characterised in section 4.3.6. The cameras were operated at 3 kHz. The exposure time was 9 μs, with the actual measurement duration determined by the phosphorescence decay time of BAM:Eu (1 μs at room temperature). The cameras were fitted with 50 mm

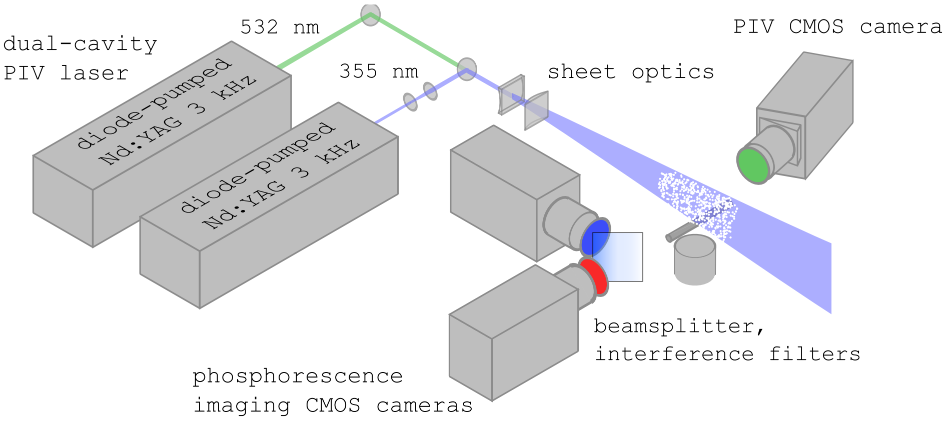

Figure 5.1: Experimental setup for kHz-rate temperature and velocity imaging.

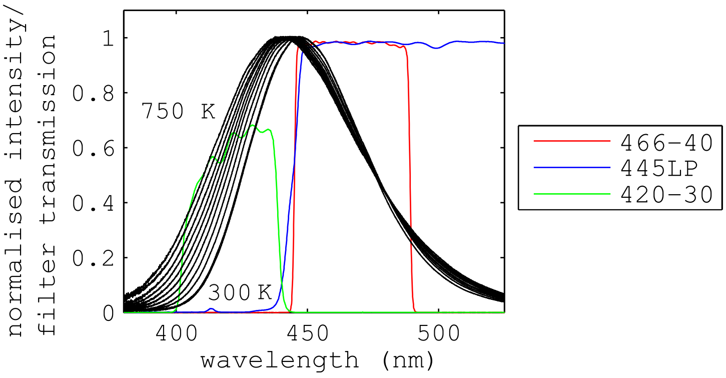

Figure 5.2: Normalised emission spectrum of BAM:Eu between 300 - 750 K (50 K temperature intervals). Filter/beamsplitter transmission profiles used for kHz-rate temperature imaging are superimposed.

f/1.4 Nikon lenses and the improved filter combination identified in section 4.4.3 was used to separate and filter the two detection channels. The transmission profiles of the beamsplitter (445 nm longpass) and filters (466-40 and 420-30 nm) are also shown in figure 5.2. The entire camera/beamsplitter system was aligned using micrometre stages to minimise relative distortion and differences in the light collection path.

After acquisition, background images were recorded and subtracted from the image pairs. Images were then spatially overlapped using software-based mapping based on images of a calibration target positioned in the measurement plane. A cutoff filter at 15 counts was applied (corresponding to approximately three times the readout noise of the camera), followed by 4 x 4 digital binning and a 3 x 3 unweighted moving average filter. The final spatial resolution was 720 μm,

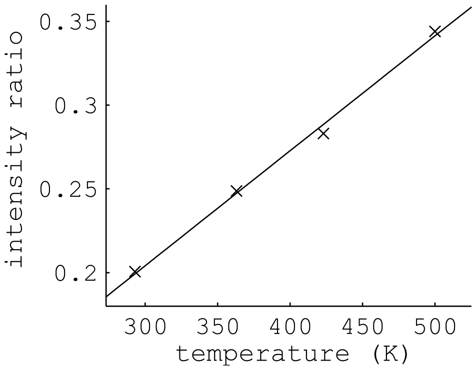

Figure 5.3: Temperature calibration curve. A quadratic fit to the measured datapoints is also shown.

experimentally determined by the full width half maximum of the line spread function measured using images of a razor blade positioned in the measurement plane.

An intensity ratio image was computed from each filtered image pair. Spatial non-uniformity in the relative light collection efficiency was accounted for by dividing each single shot intensity ratio image by an average ratio image based on 100 uncorrelated shots obtained in the gas-phase at room temperature. As mentioned in section 4.3.6, frame-to-frame gain fluctuations were found to occur for one of the cameras. A region in each image at a known (room) temperature was used to correct for frame-to-frame differences in the overall intensity ratio.

To calibrate the intensity ratio response with temperature, a thermocouple was positioned in the measurement plane during steady operation of the jet at different exit temperatures. The thermocouple readings were compared to mean intensity ratios obtained at the same location and a quadratic fit to this calibration data was used to convert the ratio images to temperature, as shown in figure 5.3. Considering the small temperature range, the few calibration points used here are considered sufficient for this demonstration study.

Particle Image Velocimetry

For PIV, a dual-cavity, frequency doubled diode-pumped Nd:YAG laser (IS-611DE, Edgewave) was operated at 3 kHz with a pulse separation of 50 μs, equally bracketing the phosphorescence excitation light pulse. The 532 nm laser beams were superimposed on the 355 nm beam using a dichroic mirror placed before the sheet optics, and the width of the 355 nm beam was adjusted with the telescope to match the thickness of the 532 nm sheets. Light scattered by the particles was imaged using a third CMOS camera (Photron SA1.1, 12 bit, 1,024 x 1,024 pixels) equipped with a 105 mm f/2.8 Nikon lens with the f-stop at f/11 and a 532-10 nm bandpass filter. The camera was operated at 6 kHz to achieve double-frame acquisition at the desired 3 kHz. The camera was positioned on the opposite side of the measurement plane at a 6° angle to prevent any interfering background reflections between the two detection systems. A Scheimpflug adapter was used eliminate off-axis defocusing across the field of view.

The Mie scattering images were mapped to an independent coordinate system using the same calibration plate. To overlap the temperature and velocity images, an imaged reference point was then used to match the origin of both coordinate systems. Particle images were then processed using a multi-pass cross-correlation algorithm (DaVis 7.2, LaVision) with an interrogation window size of 32 x 32 and 50% overlap, resulting in a final vector spacing matching that of the temperature resolution (720 μm).

Triggering System

High-speed CMOS cameras acquire frames continuously, overwriting the onboard memory. The cameras receive ‘sync’ signals at the appropriate frequency to synchronise this acquisition, provided by a trigger clock (9528, Quantum Composers). The clock also provides signals to the UV laser Q-switch and the Q-switch of each cavity of the PIV laser. For PIV, dual-frame acquisition is achieved by timing the pulses of each independently-triggered cavity so that the first laser cavity is triggered at the end of the exposure of one frame and the second laser cavity is triggered at the beginning of the exposure of the subsequent frame. With the PIV camera operating at a framing rate of 6 kHz, image pairs are prodcued at the desired 3 kHz repetition rate. The speed of the onboard camera clock is 175 kHz for the SA1.1 camera, so the minimum interframe time (δt) using this method is 5.7 μs.

To temporally match the first frame of every sequence, a recording was commanded using a custom-made manual trigger switch unit, which received pulses from the clock at 3 kHz and on manual activation transmitted a single pulse to the trigger input of all three cameras.

The 16 Gb onboard memory of the temperature imaging cameras was sufficient to record $\sim$ 11,000 frames at full resolution, corresponding to a recording duration of 3.6 s. The actual recording time was limited by the frame rate and memory size of the PIV camera. With an 8 Gb memory, this camera could only record $\sim$ 5,500 frames at 1,024 x 980 pixels, for a total aquisition time of 1 s.

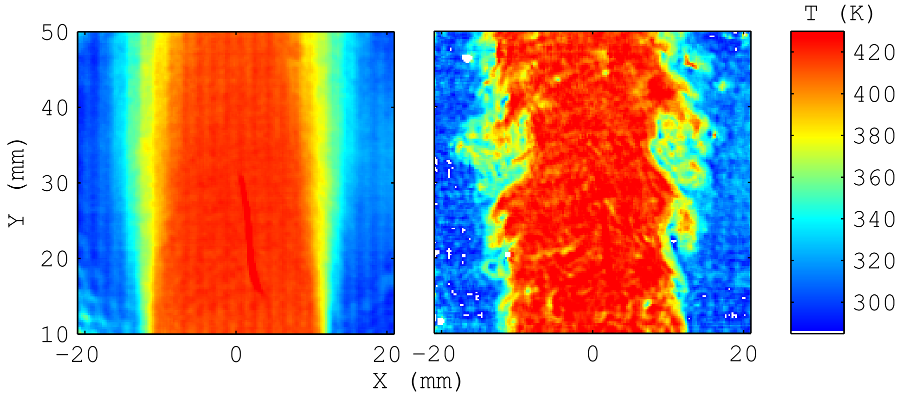

Figure 5.4: Temperature fields in a turbulent jet recorded at 3 kHz (T = 423 K). Left: average field compiled from 100 single shot images. Right: single shot.

5.2 Results

Accuracy and Precision of kHz-rate Thermometry

Figure 5.4 shows an average image and example single shot recorded in the jet at 423 K. From images similar to this (and from other image sequences) recorded at four steady jet exit temperatures, the accuracy and single shot precision of the technique at kHz rates was determined.

At each temperature, from 100 uncorrelated images 20,000 independent measurements were sampled from an 8.8 mm x 8.8 mm region in the jet potential core. At the highest axial position in this region the jet core was 9.5 mm wide, ensuring no turbulent temperature fluctuations influenced the results. These statistics were used to compile the histogram shown in figure 5.5. The single shot pixel-to-pixel standard deviation was found to be 4.9 K (1.7%), 7.8 K (2.1%), 9.2 K (2.2%) and 21.9 K (4.4%) at 293 K, 363 K, 423 K and 500 K respectively. From repeated measurement sequences, the maximum deviation of the mean measured temperatures to the flow temperature indicated by a thermocouple positioned in the measurement plane was 5 K.

Measurements in the Wake of a Heated Cylinder

To demonstrate the utility of the combined diagnostics, time-resolved temperature and velocity fields were measured in the wake of the heated cylinder. Figure 5.6 shows nine temperature and velocity fields, each separated by 5 ms. The mean velocity field has been subtracted from the instantaneous fields to better visualise the movement of eddies, and only every fifteenth image from the original 3 kHz recording is displayed so that the cyclic vortex shedding can be seen.

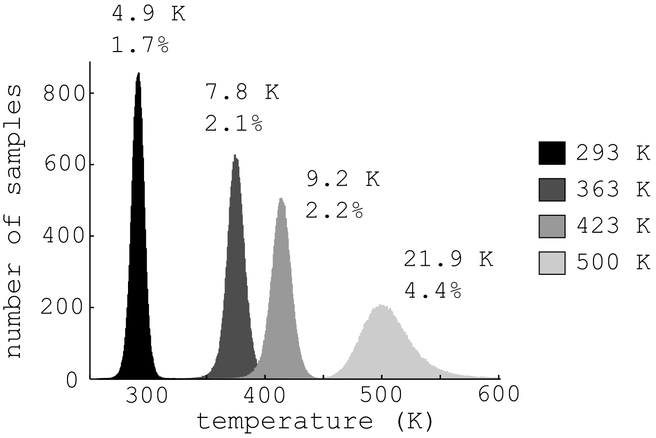

Figure 5.5: Histograms of 20,000 independent temperature measurements, recorded at 3 kHz for each steady jet temperature.

Counter-rotating eddies of hot gas are alternately shed from either side of the rear stagnation point, which then cool as they are convected away from the cylinder. The Strouhal number $St = fL/U$, where L and U are the characteristic length (in this case the cylinder diameter) and free stream velocity respectively, and f is the frequency of the vortex shedding cycle, tends to a constant value of $St = 0.2$ in this regime of Reynolds numbers [128]. From the image sequence the frequency of the cycles is approximately 40 Hz, in good agreement with the theoretical value ($f = 50$ Hz). The recording rate surpasses that required to resolve the phenomena of interest, but the sampling rate was chosen for demonstration purposes since kHz rates are appropriate for the measurement of unsteady flow behavior more frequently encountered in the study of turbulent flows of practical interest. A video of this flow covering 50 ms at the full 3 kHz recording rate, allowing the visualisation of two full vortex shedding cycles, has also been published online [97].

5.3 Discussion

Comparison of Low-speed/High-speed Thermometry

In chapter 4, the DPSS laser and CMOS camera technology which were used in this demonstration were compared with the low-speed flashlamp-pumped solid-state lasers and interline transfer CCD cameras used previously [15]. Regarding the phosphor excitation, the fluence used here was ~ 4 mJ/cm^2, which is sufficient to saturate 2 μm BAM:Eu particles. Therefore, despite the two orders of magnitude lower pulse energy, the same signal per particle can be achieved.

Concerning luminescence detection, the filters were improved and a dichroic

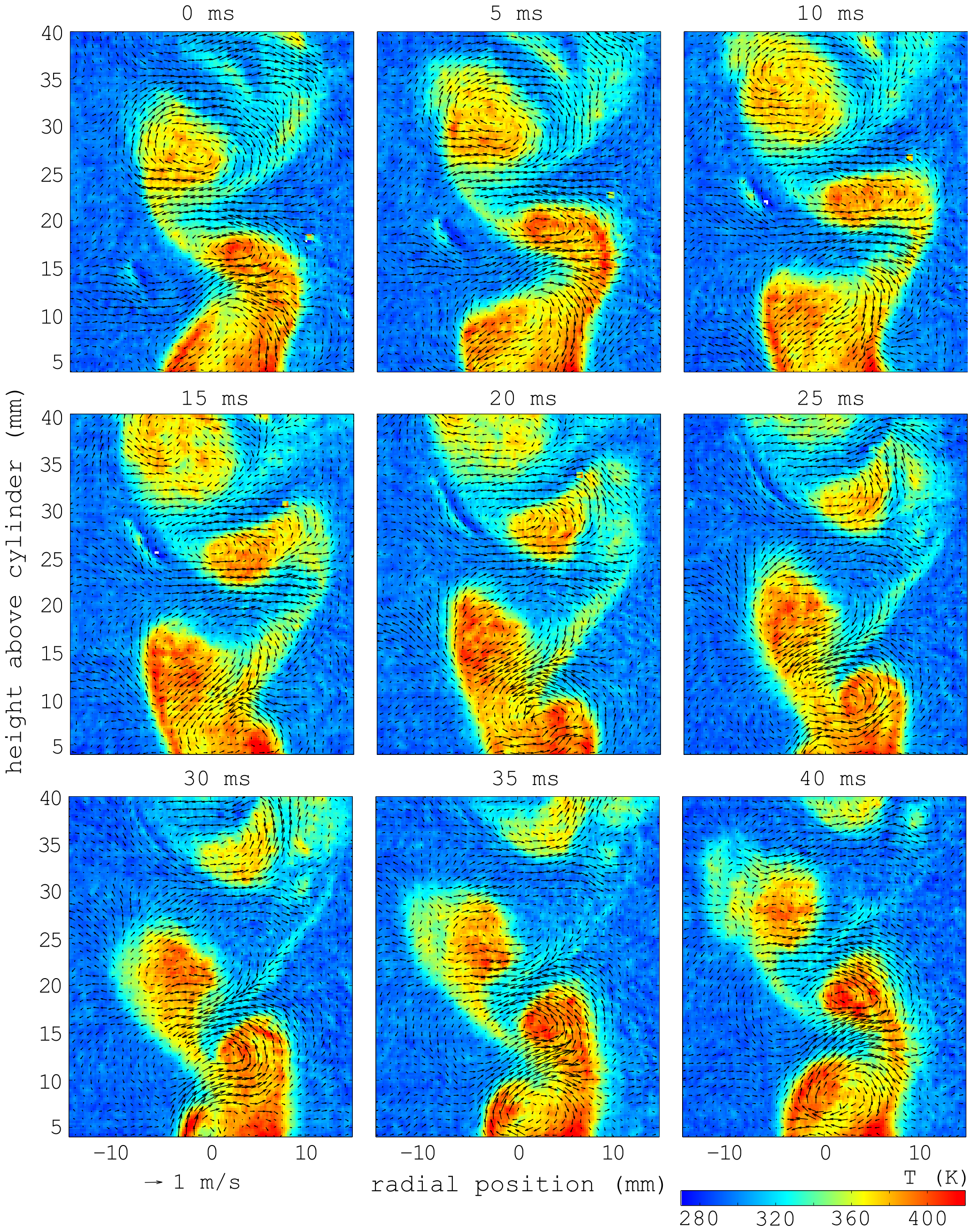

Figure 5.6: Temporal evolution of the temperature and velocity fields in the wake of a heated cylinder. Every fifteenth image of the 3 kHz recording is displayed. The mean velocity has been subtracted from the instantaneous velocity fields.

beamsplitter was used. This results in a 5 × increase in collection efficiency, compared with the filters used previously [15]. However, for the same collection optics, the performance of the high-speed CMOS cameras should be compared with low-speed, hardware-binned interline transfer CCD cameras.

Figure 4.11 in section 4.3.5 showed that read noise has a pervasive effect on the relative camera performance. At low light levels the CCD system offers improved performance, but as the signal level increases the high-speed detection system offers equivalent and even better results. Using measurements of the signal per particle from previous work using BAM:Eu [16] and those presented in the next chapter, the particle number density used in these experiments was calculated to be approximately 6×10^{11} particles/m^3, which produces a reasonable temperature precision. However, this relative performance is an important consideration in applications where signal levels are expected to be much lower, for example where collection is limited, seeding densities are lower, or at high temperatures, where thermal quenching of the luminescence emission decreases the signal per particle. In such cases, the temperature precision achieved with low-speed CCDs cannot currently be realised using the high-speed system.

Sampling Rate

The pulse energy of the 355 nm laser is constant up to 10 kHz and so the thermometry measurement could have been performed at frequencies up to 10 kHz (at reduced readout of 1,024 x 744 pixels) without any decrease in the signal to noise ratio. In this experiment, the sampling rate for simultaneous measurements was limited to 3 kHz by the PIV camera, which operated at nearly full frame readout to achieve comparable spatial resolution between the two measured fields.

6 Characterisation of Zinc Oxide

For some applications subtle differences in temperature are important. Examples include natural convection, some cases involving ignition in a flow (typically turbulent) where the temperature distribution is non-uniform, and other situations such as heating and ventilation in buildings and vehicles. Such applications require a high measurement precision.

In principle the intrinsic precision of ratio-based thermometry using phosphors is a function of the signal, which determines the precision in the intensity ratio field; and the sensitivity (change in intensity ratio with temperature). Signal levels can be improved by increasing the seeding density, using a different excitation scheme, employing different phosphor particles with a high absorption cross-section and quantum efficiency, or improving the luminescence collection. Considering the experimental setup in chapter 4, some of these approaches are difficult to realise in practice. For example, laser energy and wavelength are limited for high speed measurements and may not increase the signal because of saturation; and fast lenses with optimised filters and a bright, short lifetime phosphor (BAM:Eu) are currently implemented.

For the same experimental parameters that govern the signal-to-noise ratio (and the intensity ratio precision), the temperature precision goes directly with the improvement in sensitivity. For a given phosphor, the sensitivity can to some extent be controlled by choosing appropriate filters, but there is a compromise between sensitivity and signal.

Ultimately, finding a phosphor with a more pronounced temperature-dependence of the emission spectrum would provide an inherently greater sensitivity. To achieve improved temperature precision and meet the demands of the applications mentioned above, the aim of this chapter is to identify and test a phosphor with a more sensitive ratio response. The temperature range considered is 300 - 500 K, relevant to heat transfer studies in practical systems.

For this study, phosphors reported in the literature that permit sensitive ratio-based surface temperature measurements were considered. Clear candidates are zinc oxide (ZnO) phosphors containing excess zinc (ZnO:Zn) and gallium (ZnO:Ga). The strong redshift of their UV luminescence with temperature was previously investigated for temperature measurements [92,123]. ZnO:Gn was used for thermometry of burning methanol droplets [92] and ZnO:Zn applied to surfaces to determine the temperature uniformity of a heat flux burner [129], where temperature differences as low as 60 mK could be measured.

At room temperature, depending on the filters, the sensitivity reported in these studies is approximately three times higher than the BAM:Eu used so far in this work. These materials are therefore potential temperature sensors for ratio-based measurements in flows, with the desired increase in the precision of the temperature measurement.

In this chapter, first the luminescence properties of ZnO materials are presented. The role of deliberately added impurities in the doped phosphors previously used for thermometry are considered. From this ZnO itself is identified as a promising phosphor for increased temperature sensitivity, requiring characterisation for flow thermometry.

Spectrally-resolved investigations of aggregated ZnO powder are presented. The particles are also characterised in the gas, where the nature of the laser-particle interaction matches the intended application (see section 4.1.5 for a complete discussion). The luminescence and intensity ratio response of ZnO particles to various parameters including temperature are measured, and the results are interpreted in the context of ratio-based temperature imaging. In terms of signal and temperature precision, the results are compared to those obtained using BAM:Eu particles. Precise thermometry in a weakly turbulent ($Re = 2000$) electrically-heated airflow is demonstrated. Sources of error are analysed in detail. Further experiments are performed to examine the effects of laser fluence and power density on the luminescence emission.

6.1 Properties of Zinc Oxide

6.1.1 Luminescence Properties

ZnO emits luminescence in two bands: a fast (< 1 ns) UV emission and a slower (~ 1 μs), broad emission in the green spectral region. Among a range of optoelectronics applications, the optical properties of ZnO are favourable for the development of UV LEDs, lasers based on ZnO nanostructures [130, 131], and scintillation detectors [76]. The green emission of ZnO is also employed for field emission displays [132]. It is also used in medicine and other skin treatments (including blocking UV radiation in suntan lotion), pigments in paints, anti-corrosive coatings, and additives in rubber. Its high heat capacity (500 J/kgK), thermal conductivity ($\sim$ 100 W/mK) and melting point (2200 K) [76] means ZnO is used to control the thermal and optical properties of ceramics.

ZnO is a direct band gap semiconductor (3.37 eV, corresponding to $\lambda =$ 368 nm) [75]. The room temperature absorption spectrum is shown in figure 6.1, depicting a broad band covering the wavelength of frequency-tripled Nd:YAG lasers (355 nm). At room temperature, the UV luminescence occuring at $\sim$ 385 nm is due to excitons [70, 76, 132]. ZnO exhibits this bright luminescence at room temperature because the exciton binding energy is 60 meV, which is significantly

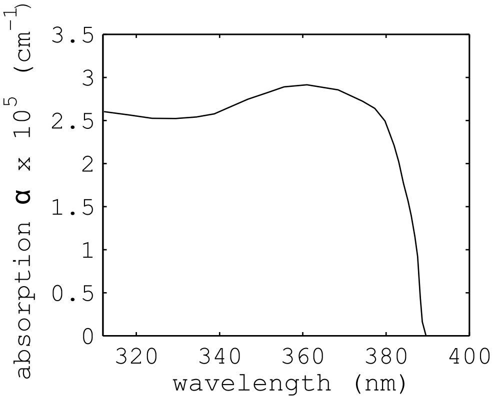

Figure 6.1: Room temperature absorption spectrum of ZnO. Data from [77].

larger than the thermal energy ($k_B T = 26$ meV at 300 K), compared to other direct band gap semiconductors e.g. gallium nitride (exciton binding energy 25 meV). The luminescence redshifts with temperature due to the decrease in the band gap width [76].

Pure ZnO emits UV luminescence [70] but the position, linewidth, intensity and lifetime [76] as well as the temperature sensitivity depend on the type and concentration of naturally present or deliberately added impurities, which are typically on the ppm level. For example, the lifetime of ZnO is $\sim$ 700 ps but the addition of e.g. gallium or iron can reduce the lifetime by around one order of magnitude [76]. The origin of the green 'defect' luminescence at around 510 nm has been attributed to localised composition variations including zinc vacancies, oxygen vacancies, and the presence of copper ions [76]. Preparation or heat treatment of ZnO in low oxygen concentration environments increases the green emission intensity [131,132]. Notably, higher excitation irradiance increases the ratio of UV to green luminescence [132].

Since pure ZnO and that containing various deliberately added impurities is reported to emit UV luminescence, and noting that most ZnO material would contain impurities to some extent, ZnO which is not deliberately doped could be considered as a material useful for thermometry.

6.1.2 Particle Size and Manufacture

The majority of worldwide ZnO is manufactured using the indirect ('French') process. A flow of vapourised zinc reacts with oxygen to form ZnO particles. The primary particle size is controlled by the temperature and residence time in the flow. This process forms particles a few hundred nanometres in size. Larger crystals are obtained using alternative methods [76].

Different ZnO powders were obtained from Sigma-Aldrich. According to the manufacturer particles are sieved < 45 μm and specific information on size average and distribution varied. Figures 6.2a and 6.2b show SEM images of the phosphor (96479, Sigma-Aldrich) used for the measurements described in this chapter. For all tested powders the primary particle size was around 200 nm. The provided assay guarantees a chemical purity > 99 %, listing over a dozen trace elements present in the batch. No specific size distribution was available for this powder.

The temperature response time of primary particles is just over 1 μs at 293 K. For larger agglomerates seeded into the flow with a projected size of, e.g. 2 μm (see figures 6.2a and 6.2b), the response time is 100 μs, based on a spherical particle. However, in this case the response time will be significantly overestimated since the ratio of surface area to volume is much larger for these particles.

Treatment that is used to intentionally vary the composition of ZnO can affect the particle size. For example, ZnO is fired in a reducing (argon) atmosphere to promote oxygen vacancies, leading to excess zinc (ZnO:Zn). SEM images of samples (GK30/UF-F2, Phosphor Technology) of both the precursor ZnO and fired material (figures 6.2c and 6.2d) reveal such differences (the tested precursor ZnO appears as the ZnO depicted in figures 6.2a and 6.2b and is not shown here). Figure 6.2d clearly shows the SiO_2 coating, which was applied by the manufacturer to improve flowability.

It is presumed that during firing the particles coagulate, creating larger primary particles which form fused agglomerates. Particles of this size will not trace the flow with sufficient accuracy. Furthermore, preliminary characterisation measurements seeding this phosphor powder proved problematic. Large signal spikes recurring in luminescence images caused by these large, unseparated agglomerates tended to saturate the CCD camera. In each image these regions must be filtered using software, leaving large gaps with no signal.

6.2 Spectrally-Resolved Measurements

In this section the setup for spectrally-resolved measurements of aggregated phosphor power is described. Different ZnO samples, the dependence of the luminescence emission on the laser fluence and the temperature response are studied.

6.2.1 Experimental Setup

To obtain spectra of zinc oxide samples at different temperatures, the powder was contained in a ceramic crucible and placed in an optically accessible temperature-controlled oven (Lenton Furnaces). Samples were excited at 355 nm using the third harmonic of a flashlamp-pumped 5 Hz pulsed Nd:YAG laser (Quanta-Ray

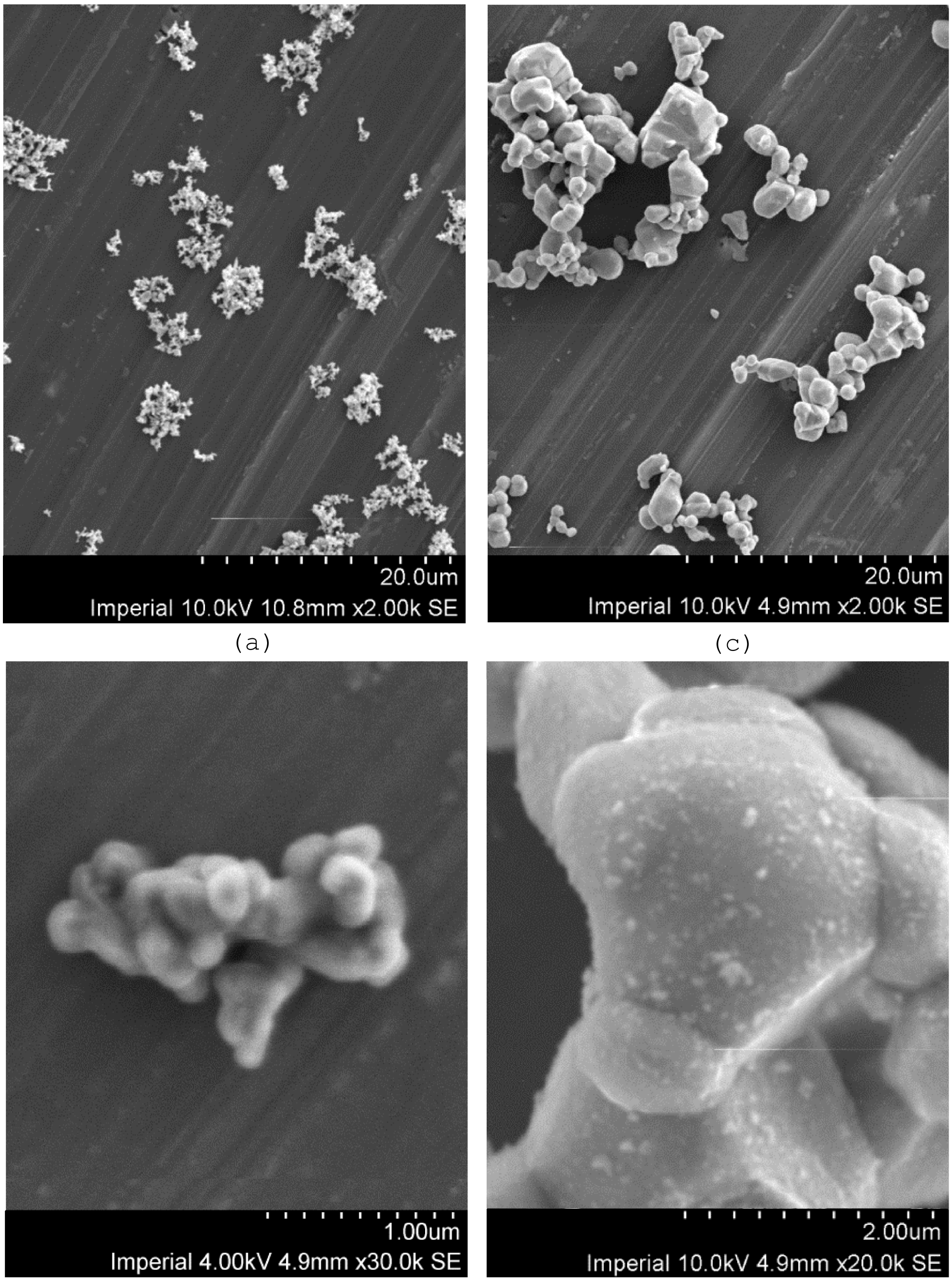

(a) (c)

(b) (d)

Figure 6.2: SEM images of ZnO powders. (a) and (b), left: ZnO (96479, Sigma-Aldrich). (c) and (d), right: ZnO:Zn (GK30/UF-F2, Phosphor Technology). Note the difference in magnification between the lower images (b) and (d).

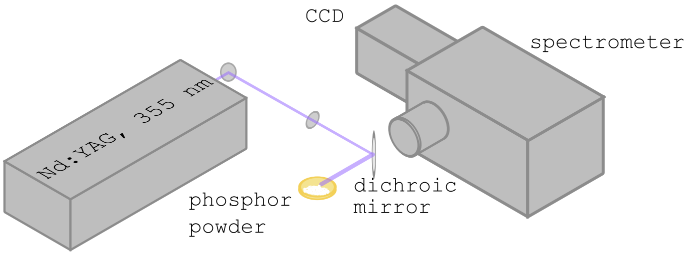

Figure 6.3: Spectroscopy setup. The furnace used to heat the phosphor samples is not shown.

GCR-150, Spectra-Physics), with a nominal pulse duration of 10 ns (figure 6.3). A photodiode-based energy-monitoring unit (Energy monitor V9, LaVision) was used to measure the energy of the laser on a shot-to-shot basis. This system was calibrated using a pyroelectric energy detector (PEM 45K, Radiant Dyes). The laser beam diameter was adjusted using an iris and reflected onto the sample using a dichroic mirror.

Luminescence was collected using an f/4 lens and spectrally dispersed using a 300 mm focal length f/4 spectrometer (Acton SP-2300i, Princeton Instruments) with a grating groove density of 300 g/mm. Spectra were recorded using an interline transfer CCD camera (Imager Intense, LaVision) with an exposure time of 5 μs. The entrance slit width was 100 μm, providing a spectral resolution of 1 nm, as measured using a mercury lamp. The transmittance of the complete detection system was calibrated using the reference spectrum of a tungsten halogen lamp (LS-1, Ocean Optics).

Spectra were acquired at different temperatures during a furnace cooling cycle lasting for a duration of several hours. The temperature of the phosphor was measured using an N-type thermocouple positioned in the powder. These measurements were in good agreement with the furnace temperature readings, indicating temperature uniformity throughout the furnace and within the probed powder.

ZnO Samples

Different samples of ZnO were examined. ZnO:Zn (GK30/UF-F2, Phosphor Technology) and two different production lots of the same ZnO (96479, Sigma-Aldrich) were illuminated with a fluence of 2.5 mJ/cm^2.

This ZnO phosphor emits UV luminescence. Within the repeatability of the measurement, signal levels of all samples are similar to within 50%. The normalised spectra in figure 6.4 indicate clear differences between the doped and

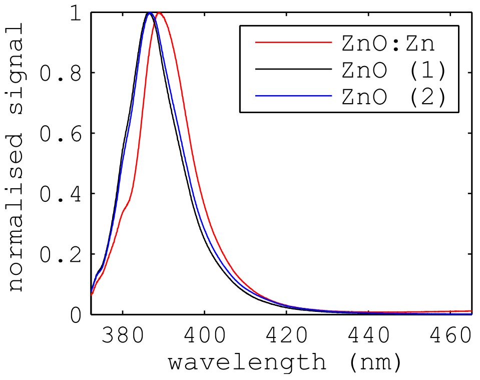

Figure 6.4: Normalised spectra of ZnO samples ($T = 296$ K).

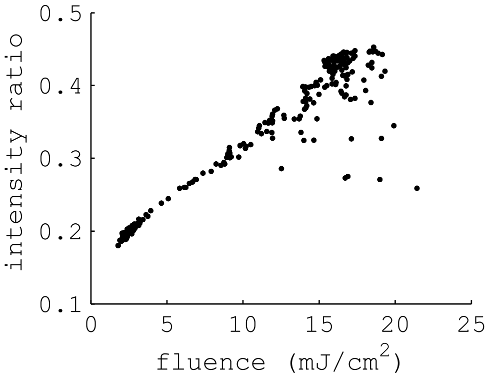

Figure 6.5: Intensity ratio against fluence for aggregated ZnO powder ($T = 292$ K).

undoped phosphors. Though the width of the emission band is similar, the sample with excess zinc shows a pronounced heel on the UV side of the spectrum and the peak is shifted 2.5 nm toward the visible. Variation between different production lots of the same ZnO is barely detectable, despite the low tolerance on impurities. These results indicate the sensitivity of the edge emission of ZnO to chemical composition.

Laser Fluence Effects in Aggregated Powder

The laser fluence was varied to investigate whether this has any influence on the emission spectrum. Spectra were numerically integrated using filters at 387-11 and 425-50 nm (see section 6.3). Figure 6.5 shows that the ratio increases with fluence. Above 10 - 15 mJ/cm^2, though the trend is maintained, for some laser shots the scatter in the intensity ratio increases, with large deviations toward lower ratios.

The origin of the ratio fluctuation is well-illustrated by the time series of

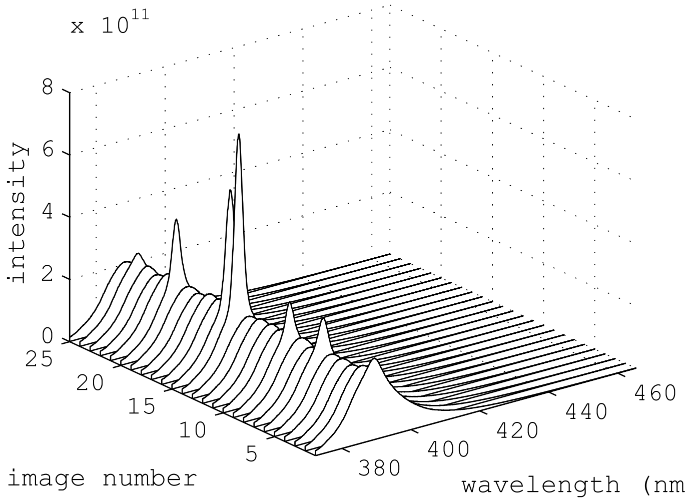

Figure 6.6: Time series of spectra recorded using a fluence of 20 mJ/cm^2.

spectra recorded with a fluence of 20 mJ/cm^2 shown in figure 6.6. The reason for some laser shots producing ratios that deviate from the trend of ratio against fluence is due to a narrowing of the emission peak and a pronounced increase in intensity. For shots where this chaotic phenomenon clearly occurs the lineshape and intensity of the luminescence emission vary. This prevents investigation of the behaviour of aggregated powder at higher fluences since some shots saturate the camera.

Other studies of zinc oxide have attributed this behaviour to amplified spontaneous emission (ASE) [133, 134]. Emitted luminescence illuminates other excited particles, amplifying the luminescence by stimulated emission. For pulse durations in the picosecond regime the profile and intensity of the lasing action is uniform [134]. Here, the laser pulse duration is one to two orders of magnitude longer than the luminescence lifetime but these excitation power densities still produce a sufficient population inversion that leads to ASE. In both the cited studies, for pulses in the nanosecond regime similar irregularities in ASE behaviour was reported. The threshold for ASE varies and may depend on the particle size distribution and particle arrangement [133], which affects the re-absorption and multiple scattering of luminescence. Lasing action is presumed not to occur within single particles acting as a cavity, since the primary particle size is shorter than the light wavelength.

A powder sample was also exposed to a fluence of 100 mJ/cm^2 for several hundred laser shots and then left for several minutes to allow any heat buildup

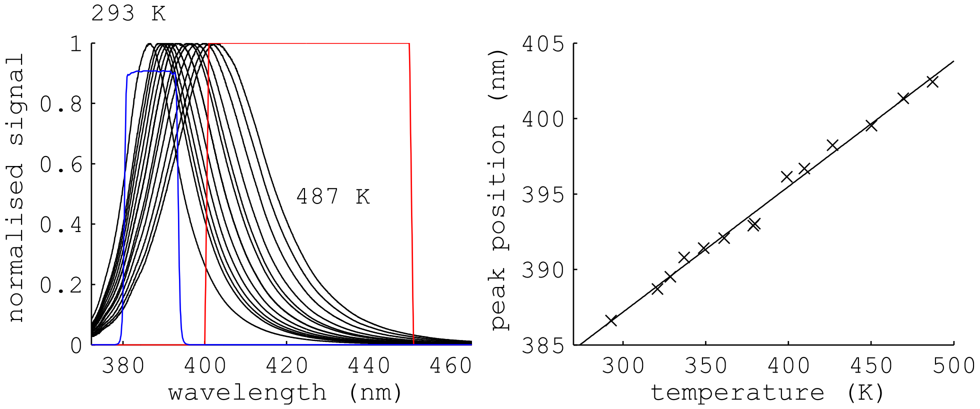

Figure 6.7: Left: normalised ZnO spectra recorded using a fluence of 5 mJ/cm^2. The temperature interval between curves is approximately 20 K. The transmission profiles (provided by the manufacturers) of the filters used in the characterisation study in section 6.3 are shown in colour: blue: 387-11 and red: 425-50. Right: emission peak maximum with temperature.

to dissipate. Following this treatment, to the eye the powder appeared darker and the emission intensity when illuminating the phosphor with a low fluence was reduced by a factor > 4 (results not shown here), indicating damage likely caused by laser-induced breakdown.

It is difficult to determine whether these effects always occur to some degree in aggregated powder. However, when the particles are dispersed in a fluid as a tracer for temperature measurements, ASE between multiple particles is considered unlikely due to the small subtended solid angle amongst particles. The indication of laser-induced breakdown at high fluences suggest operating in a regime of lower fluence is preferable. These results also highlight the difficulties in characterising phosphors using studies of aggregated powder outlined in section 4.1.5.

Temperature

ZnO powder was heated to 487 K and spectra were periodically recorded at 20 K intervals during a continuous cooling cycle using a laser fluence of approximately 5 mJ/cm^2 (figure 6.7). The luminescence emission peak is redshifted, following the decrease in the bandgap width with increasing temperature. Broadening of the emission line is also evident.

The redshift is pronounced, providing good prospects for sensitive ratio-based thermometry, and also continuous between the tested 293 and 487 K as shown in the right plot of figure 6.7. The absolute change of the emission peak position for a given temperature difference is approximately constant with increasing temperature ($\sim$ 0.09 nm/K) in this temperature range. Using the empirical Varshni formula, which relates the band gap to temperature [76], the predicted change in the peak position of $\sim$ 0.04 nm/K is significantly lower than that measured, and the magnitude of the change increases with temperature.

6.3 Gas-phase Characterisation

The results of the previous section suggest that the ZnO phosphor is suitable for sensitive ratio-based measurements. In this section the characterisation of ZnO particles in the gas is presented, which is arranged as follows. The experimental setup is described, including the particle counting system required for gas-phase characterisation. For the results, firstly measurements of the luminescence intensity, temperature response and intensity ratio precision are presented to demonstrate the feasibility of using ZnO as a temperature tracer. Additionally, BAM:Eu particles were measured using the same system to compare the intrinsic intensity ratio and temperature precision of each phosphor, and evaluate the potential benefits of ZnO in terms of temperature sensitivity. This provides a back-to-back comparison of the two phosphors, and validates the system which was previously used for the study of BAM:Eu particles [16]. Further results are organised into two parts, where the seeding density, laser fluence and temperature are studied to evaluate their influence on the luminescence intensity and the intensity ratio. Some discussion and interpretation of the results is included where appropriate, and implications for practical temperature imaging are highlighted.

6.3.1 Experimental Setup

Phosphor Particles and Flow Facility

Unless otherwise stated, for all measurements described in this section ZnO phosphor particles (96479, Sigma-Aldrich) were used. The particles were dried overnight in a furnace at 125 °C before use. A 21 mm diameter jet of air, seeded with a seeder of magnetic stirrer-type design, was used for the phosphor characterisation. The seeded stream could be electrically heated up to 500 K using an inline heater (AHP-7562, Omega Engineering) controlled using a K-type thermocouple placed at the jet exit. The setup is shown in figure 6.8.

Particle Counting

The aim of the particle counting system is to measure the particle seeding density, irrespective of particle size, shape or orientation, using the Mie scattering signal. As shown in section 4.1.1, the collected intensity at 90° only increases by a factor

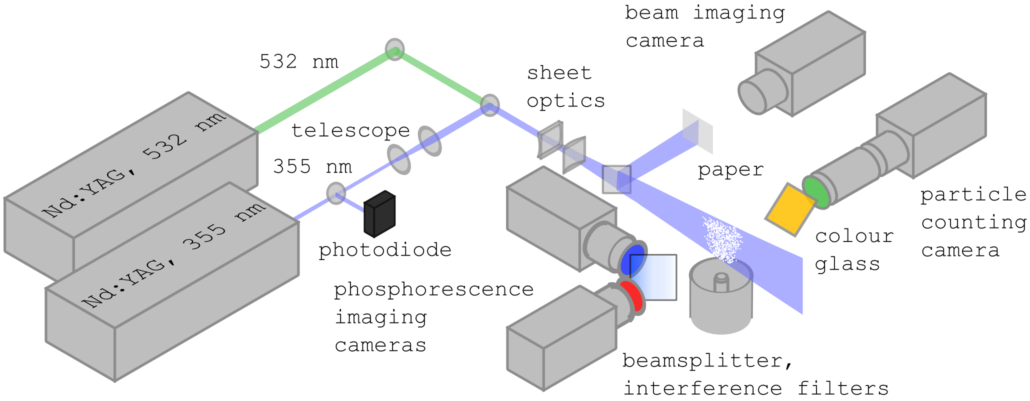

Figure 6.8: Setup for phosphor characterisation, including particle counting system.

of ten for particles with a diameter between 200 nm and 5 μm. Therefore, with a correctly adjusted system, the presence of particles can be detected with equivalent certainty over this range of particle size using a 12 bit CCD.

The particles were illuminated at 532 nm with the second harmonic of a 5 Hz pulsed Nd:YAG laser (Quanta-Ray LAB-150, Spectra-Physics). A thin light sheet was formed in the measurement plane (measured as 160 μm, see below) using a f = +500 mm cylindrical lens. Care was taken to ensure that the fluence of the green beam was kept constant at approximately 700 mJ/cm^2 for all measurements presented here. The peak intensities of the weakest particle signals were well above the 15 count threshold (see below).

A hardware binned (2 x 2) interline transfer CCD camera (Imager Intense, LaVision) equipped with a 2 X teleconverter (Tamrom AF 2X), a 105 mm f/2.8 lens with the f-stop at f/4, a 532-10 nm interference filter (LaVision), and an OD 2 neutral density filter was used to detect the scattering signal. A colour-glass (OG515, Schott) was positioned in front of the detection system at 45° to prevent interference arising from luminescence reflected by the 532 nm filter in the luminescence detection channels. The field of view was 7.7 x 10.2 mm.

Images were then processed using Matlab in order to evaluate the number of local maxima. First, a cut-off filter of 15 counts was applied to filter above the camera read noise. The counting algorithm then sorted pixels by descending order of intensities. The spatial location of the maximum was marked and all pixels less than 3 pixels from this maximum were removed from the list, in order to remove the wings of high peak intensity particles. In this way, maxima were found until all pixels were evaluated. The number of local maxima in each image was used as a measure of the number of particles.

Particle Excitation and Luminescence Detection

Particles were excited at 355 nm using the same frequency-tripled flashlamp-pumped pulsed Nd:YAG laser used for the spectrally resolved measurements. 532 nm and 355 nm beams were overlapped in the measurement plane using a long-pass dichroic mirror. The UV sheet thickness was set independently of the particle counting system by controlling the beam size before the sheet forming optics (f = +500 mm cylindrical lens) using a Galilean telescope comprised of f = -100 and +125 mm spherical lenses.

The luminescence emission from the particles was detected by two interline transfer CCD cameras (Imager Intense, LaVision) with 50 mm f/1.4 Nikon lenses. The cameras were hardware-binned 4 x 4.

Two high transmission (> 90 %) interference filters at 387-11 (84094, Edmund Optics) and 425-50 (86961, Edmund Optics) were chosen to filter the luminescence emission, using the sensitivity analysis in section 4.4.3. Transmission curves are shown in figure 6.4. A 50:50 plate beamsplitter, AR-coated on the reverse side (46642, Edmund Optics) was used to separate the two channels. The camera exposure time was set to 5 μs, beginning 1 μs before the laser pulse. The field of view of the cameras was 28 x 21 mm. The camera/beamsplitter system was manually adjusted and no software mapping was used. Using this procedure, the mean residual displacement between the two recorded images was 0.15 binned pixels, as determined by cross-correlation. Background subtraction, cutoff filtering, and a moving average filter were applied to the images, for a final resolution of 600 μm. Further processing used to correct and extract information from the images is described where appropriate.

Laser Energy and Sheet Profile Measurements

To accurately size the probe volumes in order to determine the seeding density and the excitation fluence, the laser sheet profiles were measured. The laser sheets were reflected using a glass window with an AR coating on the reverse side onto a thin piece of paper in a position that matched the window - measurement volume distance. This paper was imaged using a CCD camera and lens. The images of the sheets reflected from both the front and the back surface of the glass window were found to have the same FWHM thickness, confirming the homogeneity and linear character of the paper fluorescence. Sheet thicknesses and vertical distributions were repeatedly checked during measurements and for both laser systems found to be independent of the pulse energy. Alternatively, a similar system that directly illuminates the CCD chip could be used [135].

The same system described in section 6.2.1 was used to measure the pulse

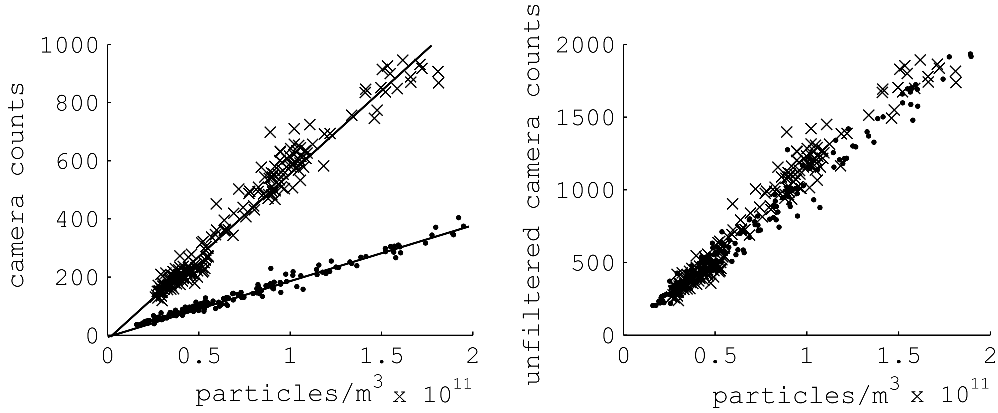

Figure 6.9: Left: Signal of seeded ZnO (dots) and BAM:Eu (crosses) particles recorded using an excitation fluence of $\sim$ 50 mJ/cm^2. The signals plotted here are the filtered channels (387-11 for ZnO and 466-40 for BAM:Eu). Each datapoint represents the average intensity of a single sampled image. Linear fits to both datasets are also shown. Right: unfiltered (corrected) signal, indicating that the luminescence intensity of each phosphor is very similar.

energy of the UV laser on a shot-shot basis, which varied on average by 10 %. The overall pulse energy was varied using the laser flashlamp energy.

6.3.2 Signal Comparison and Measurement Precision

In this section measurements of the luminescence intensity, temperature response and intensity ratio precision of ZnO and BAM:Eu particles are presented to evaluate the potential benefits of ZnO in terms of temperature sensitivity.

Luminescence Signal

Simultaneously the particle number density, laser energy and luminescence signal of the seeded particles were measured. The signal for each channel was evaluated using the mean number of counts recorded in a region of the jet that remained unmixed.

The results shown in figure 6.9 indicate that, as expected, the luminescence signal is a linear function of the seeding density. For direct comparison, also plotted is the signal of 2 μm BAM:Eu particles (KEMK63/UF-P2, Phosphor Technology), which were seeded into the same flow in a separate experiment using a spectral filter combination proposed in section 4.4.3.

The signals plotted on the left in figure 6.9 are the optically-filtered luminescence emissions. Using the emisson spectra, the proportion of light integrated by each filter combination can be used to determine the relative unfiltered lumines-

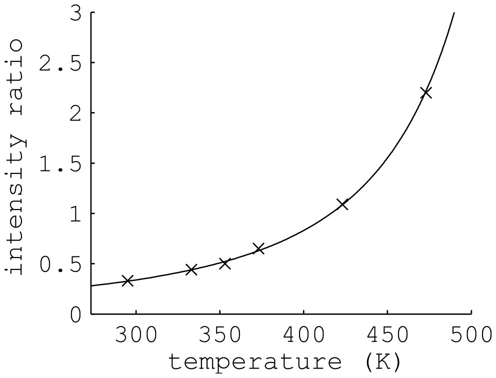

Figure 6.10: Temperature calibration curve for ZnO.

cence emission of each phosphor, which is plotted on the right in figure 6.9. This indicates that the emission intensity per particle of BAM:Eu and ZnO is very similar.

Particles ranging between 200 nm and 2 μm are detected with equivalent certainty by the counting system. The absorption cross-section is strongly dependent on the particle diameter. If it is presumed that primary ZnO particles (200 nm) are seeded into the flow, this result would suggest that the absorption coefficient of BAM:Eu is several orders of magnitude lower than ZnO, given that the quantum efficiency of BAM:Eu is $>$ 90 % [70].

Alternatively, it is possible that agglomerated ZnO with an effective diameter ($\sim$ 1 - 2 μm) comparable to primary BAM:Eu particles is probed in these experiments. In this case, light absorption would have a complex dependence on the agglomerate size, shape and structure. Though it is not possible to draw a definite conclusion regarding the relative absorption properties and quantum efficiency of the two phosphors, it is evident that for the same number of particles and for similar experimental conditions, signal levels are of a comparable magnitude.

Temperature Calibration

The measurements in section 6.1 already indicate that ZnO will have an intensity ratio response to temperature. This was investigated in the heated jet over a range of temperatures between 295 and 473 K, to produce the calibration curve shown in figure 6.10. The few calibration points used here are considered sufficient for this demonstration study. It should be noted that compared with the calibration curve of BAM:Eu in chapter 5 (figure 5.3), the sensitivity increases with temperature.

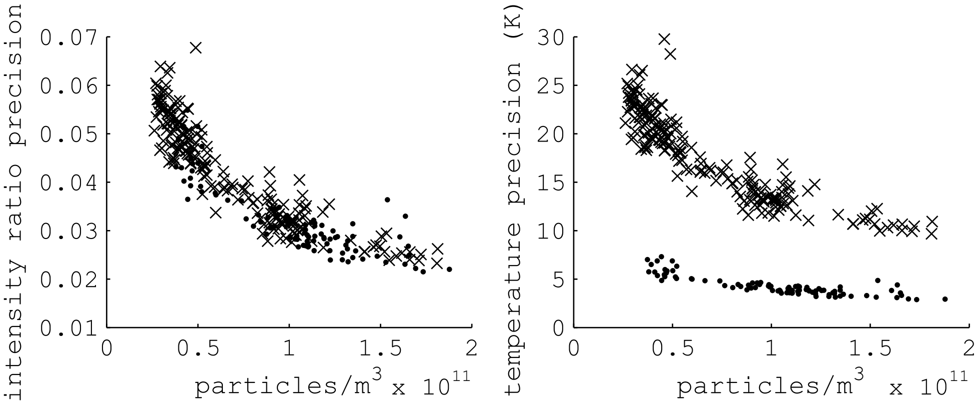

Figure 6.11: Left: Normalised single shot intensity ratio standard deviation against seeding density for ZnO (dots) and BAM:Eu (crosses). Each datapoint is the intensity ratio standard deviation of a single sampled image. Right: Temperature precision. Results were evaluated from data on the left using calibration curves for each phosphor.

Measurement Precision

Using the two-camera thermometry system, intensity ratio images were taken in the jet at room temperature, while measuring the seeding density using the particle counting camera. Single shot ratio images were processed as detailed above and corrected for differences in collection using an time-averaged ratio field compiled from the same recording sequence. For each image, from a region inside the jet core, the normalised standard deviation of the intensity ratio was calculated.

Figure 6.11 shows results of intensity ratio precision against seeding density for ZnO and BAM:Eu. The signal is proportional to the number of particles (figure 6.9) and so the precision improves with seeding density. Since the emission per particle is similar for ZnO and BAM:Eu, for the same seeding density, laser fluence and light collection efficiency the single shot intensity ratio precision is the same.

Using calibration measurements recorded in the heated gas for both ZnO and BAM:Eu, the data can be evaluated in terms of temperature precision as shown in figure 6.11. Because the change in intensity ratio with temperature is larger for ZnO the temperature precision is significantly improved. Using these filter combinations, at room temperature a threefold improvement in temperature precision can be achieved for the same luminescence collection and spatial resolution. This comparison clearly shows the benefits of using a phosphor with increased sensitivity.

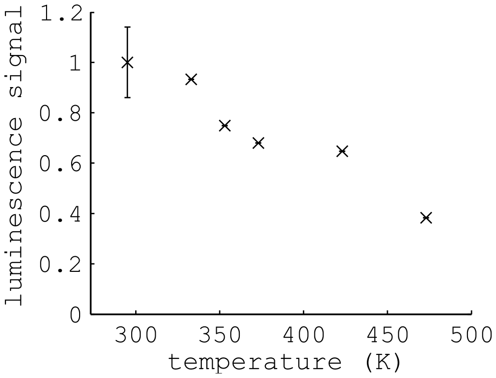

Figure 6.12: Mean luminescence signal per particle with increasing temperature. The error bar corresponds to the standard deviation of five repeated measurement sequences at 295 K.

6.3.3 Luminescence Signal

Here the effects of temperature and laser fluence on the luminescence signal are investigated.

Temperature

The flow was heated to investigate the influence of temperature on the luminescence intensity. The seeding density was also simultaneously measured to determine signal levels on a per particle basis. The effect of temperature on the overall luminescence intensity of ZnO particles is shown in figure 6.12. At 473 K the luminescence emission drops to 40 % of the signal at room temperature. Therefore, reasonable signal levels can be achieved over the range of investigated temperatures.

Laser Fluence

A strong dependence of the signal on laser fluence would be anticipated, as this would affect the number of excited luminescent centres in the material. To investigate this the laser energy was varied during recording sequences while measuring the luminescence intensity and the pulse energy. The seeding density was simultaneously measured to correct the data for seeding density fluctuations. The results are shown in figure 6.13.

Below 5 mJ/cm^2 the signal increases linearly with the laser fluence. Above this value the rate of increase of luminescence emission with laser fleunce decreases until the signal is constant. This is similar to the 'saturation' behaviour of BAM:Eu reported in earlier work [15]. This effect is considered further in section 6.5.

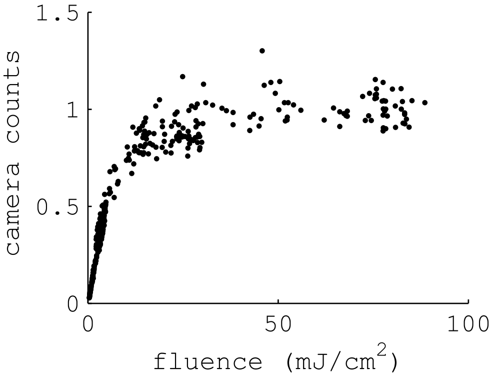

Figure 6.13: Evolution of luminescence signal with laser fluence. Each datapoint represents the average intensity of a single sampled image.

6.3.4 Intensity Ratio

Ideally, the intensity ratio is solely a function of the gas temperature. In this section the effects of seeding density and laser fluence on the intensity ratio are investigated to identify possible sources of error. Following these results, the effects of temperature on the intensity ratio are revisited.

Seeding Density

The absorption edge of ZnO depends on the concentration and type of impurities and the deliberate introduction of certain elements into the crystal. Therefore there may be a varying degree of overlap of the absorption band and edge luminescence emission of ZnO, which can be seen from the absorption and emission spectra in figures 6.1 and 6.4. This has been noted to produce a difference between the measured luminescence emission peak and that predicted by the exciton energy in studies of ZnO bulk samples [77]. In this case, luminescence can be reabsorbed by particles on the detection path. With the filters used here this effect would dominate in the UV channel, so the intensity ratio might be expected to increase with the seeding density.

This effect was investigated by measuring the seeding density and simultaneously acquiring intensity ratio images. Images were corrected as described above and the average intensity ratio of each single shot was calculated. Figure 6.14 indicates there is no effect on the measured intensity ratio for seeding densities up to 2 x 10^{11} particles/m^3 in a 21 mm diameter jet. Besides the spectral overlap, this effect also depends on the particle absorption cross-section and the length of the detection path. The absorption is too weak to produce any noticable effect for

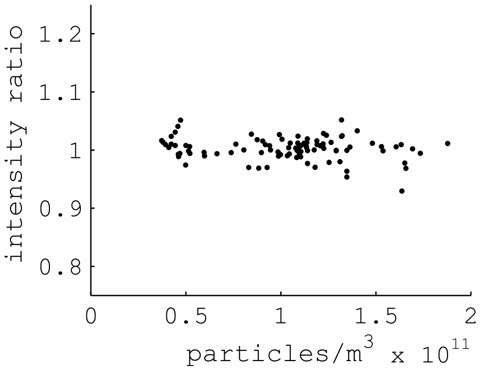

Figure 6.14: Dependence of the intensity ratio on the seeding density. Each datapoint is the average intensity ratio of a single shot image.

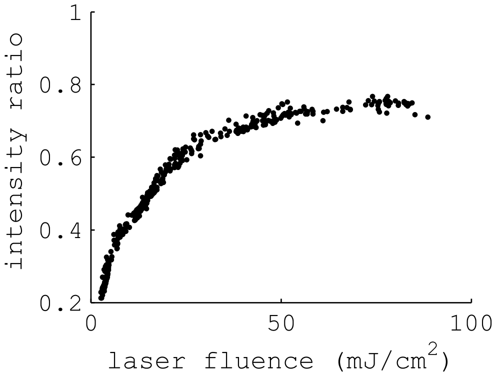

Figure 6.15: Dependence of the intensity ratio on the laser fluence. Each datapoint is the average intensity ratio of a single shot image.

these seeding densities and this path length, but this effect should be considered according to the flow under investigation.

Laser Fluence

The influence of the excitation fluence on the measured ratio was investigated (figure 6.15). The laser energy was recorded while simultaneously acquiring intensity ratio images. From the lowest fluence investigated (3 mJ/cm^2) the ratio continuously increases with increasing fluence. Beyond 60 mJ/cm^2, the ratio becomes independent of the fluence.

For the filter combination used in this study, the ratio increases with temperature and so one explanation for this behaviour is that the particles are heated by the laser pulse. Heating effects would depend on the total energy (fluence), but

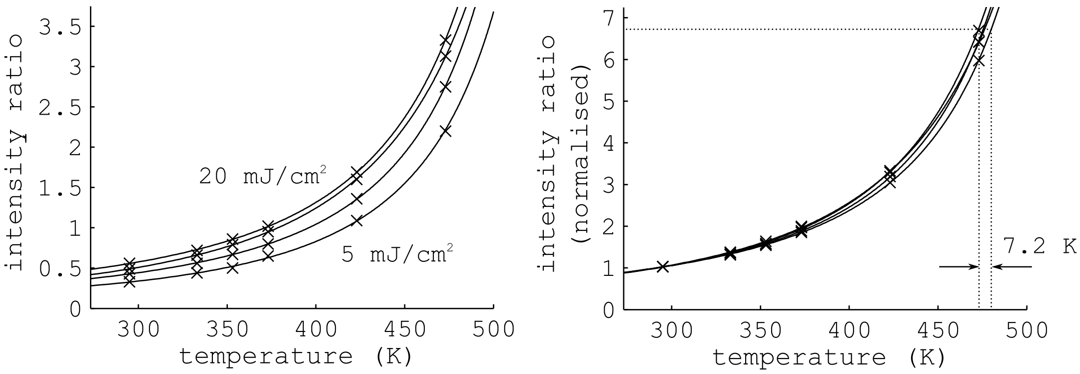

Figure 6.16: Temperature calibration curves at fluences of 5, 10, 15 and 20 mJ/cm^2. Left: absolute ratio. Right: data normalised at 295 K.

increasing the laser energy also increases the excitation irradiance (here referred to as 'power density'). Higher power densities may affect the luminescence emission, contributing to the observed trend in intensity ratio. These two proposed mechanisms for this behaviour are explored further in section 6.5.

Independent of the reason, that the intensity ratio depends on both the fluence and the gas temperature has two implications when using ZnO as a tracer for temperature imaging.

First, temporal and spatial variations in fluence must be considered, and where appropriate corrected for. For example, if the laser energy fluctuates shot-to-shot by 10%, this will lead to a shot-to-shot error of 6.2 K in temperature.

Even if the fluence is corrected for, a second implication is that the laser fluence may modify the effects of temperature on the intensity ratio, i.e. alter the calibration curve. If this is the case, then the absolute laser fluence must be known at every point within the measurement plane. The technique is greatly simplified if a single calibration curve can be applied, irrespective of fluence. This is investigated in the next section.

Temperature Calibration at Different Laser Fluences

The effect of laser fluence was investigated in the heated jet over a range of temperatures between 295 and 473 K. At each stable jet temperature the fluence was varied between 5 and 20 mJ/cm^2 (higher fluences were not used due to the laser-induced damage effects identified in section 6.2). From recorded curves of intensity ratio (IR) against fluence (similar to that shown in figure 6.15), temperature calibration data was extracted for specific laser fluences.

Figure 6.16 shows calibration datapoints for different fluences, through which curves of the form $x_1+(x_2 IR^{x_3})$ have been fitted. As the fluence increases between 5 and 20 mJ/cm^2 the absolute intensity ratio increases. If each curve is normalised to the intensity ratio at room temperature the curves collapse, as shown in the right plot of figure 6.16. The maximum deviation (7.2 K) between curves measured at different fluences is marked on the plot. This is discussed in more detail in section 6.4.2.

This indicates that the change in the normalised ratio with temperature is the same irrespective of laser fluence. The implication of this is that a single calibration curve can be used to convert the intensity ratio images to temperature, regardless of the laser fluence.

With this in mind, if spatial and temporal fluctuations in fluence can be corrected for, the dependence of the intensity ratio on laser fluence has no bearing on the measurement. Strategies for these corrections are presented in the next section.

6.4 Temperature Imaging Experiments

In this section temperature measurements using ZnO tracer particles are presented. The foregoing measurements identified that the intensity ratio depends on both the laser fluence as well as the gas temperature. In imaging experiments, generally the laser light sheet is not uniform and depends on the spatial profile of the laser beam and the optics used to form the light sheet. A particle will therefore be illuminated by a fluence that varies locally depending on its position within the laser light sheet. Furthermore, the laser energy and sheet profile may fluctuate shot-to-shot and/or drift in time.

Ordinarily, a correction for non-uniform light collection efficiency must be applied. A simple procedure for this is to use an average intensity ratio field obtained in a uniform temperature flow (see section 4.5.1). In this case the average intensity ratio field will also contain the effect of the laser fluence variation within the light sheet and so can be dealt with by using the same method. The corrected, normalised ratio field can then be converted to temperature using calibration data. The previous section identified that this normalised calibration curve is the same irrespective of laser fluence.

The feasibility of this strategy is demonstrated here, along with a detailed error analysis of this procedure and other sources of uncertainty. A fluence of 5 mJ/cm^2 is used, to demonstrate thermometry with ZnO using the lower energies of DPSS lasers, for precise time-resolved measurements.

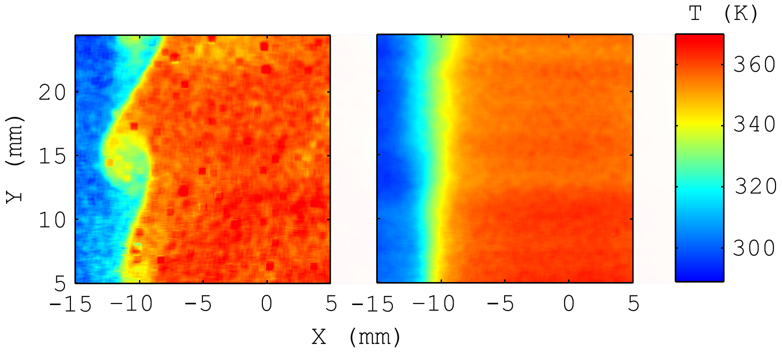

Figure 6.17: Temperature fields in a turbulent jet (T = 363 K). Left: single shot. Right: average field compiled from 100 single shot images. Image size has been reduced to 20 mm in the x-direction.

6.4.1 Temperature Imaging Demonstration

Measurements were performed in the heated jet. The flow velocity was 1.9 m/s, corresponding to a Reynolds number $Re \sim 2000$. The central jet was surrounded by an 80 mm diameter coflow ($T = 296$ K) with an exit velocity of 0.5 m/s, independently seeded with the same phosphor using a reverse cyclone seeder to ensure particles were present everywhere in the measurement volume. Flow temperatures were measured using a K-type thermocouple (nominal accuracy 2.2 K) placed at the jet exit.

The laser light sheet, formed using + 500 mm and - 50 mm cylindrical lenses, intersected the central axis of the jet. Particles were excited using a fluence of 5 mJ/cm^2. Pulse energies were measured on a shot-to-shot basis using the energy monitor system.

Luminescence images were recorded using the thermometry system. The field of view was 5 mm above the nozzle exit, slightly offset from the jet centreline to visualise the shear layer at one side of the jet. Processing was applied as detailed above, using a 7 x 7 moving average filter to obtain a final resolution of 600 μm, matching the sheet thickness. The measured ratio field requires correction for the non-uniformity in light collection efficiency, and also the spatial variation in fluence as described above. This was accounted for by recording sets of images at room temperature before heating the jet. Average ratio images compiled from these sets were normalised and used to correct the data. Corrected ratio fields were converted to temperature using calibration data recorded at 5 mJ/cm^2 as shown in figure 6.16.

Figure 6.17 shows a single shot and average temperature field recorded in the jet stabilised at 363 K. The jet is in the laminar-turbulent transition regime, and

T_{jet} (K)	296	363
$\overline{T}_{meas}$ (K)	295	360
σ_{IR} (%)	3.9	3.8
σ_T (K)	5.4	4.0

Table 6.1: Average temperature ($\overline{T}_{meas}$), normalised single shot intensity ratio standard deviation (σ_{IR}, %) and single shot temperature precision (σ_T, K) standard deviations for jet temperatures $T_{jet} = 296$ and 363 K.

the single shot shows large vortical structures generated by shear between the jet and surrounding coflow. The resolution of the measurement is sufficient to resolve cooler regions within these eddies, caused by the mixing of hot gas and cooler coflowing air. The average temperature field shows the effect of these turbulent fluctuations, leading to some broadening of the shear layer.

Average temperatures, and single shot intensity ratio and temperature statistics were evaluated from a constant temperature region of the flow comprising of 200 independent measurements (table 6.1). Thermocouple readings of the jet exit temperature are included (296 and 363 K).

The deviation between temperatures measured using the thermocouple and the phosphorescence technique is 3 K. The shot-to-shot standard deviation of the average temperature is 5.0 K.

The sensitivity of ZnO with this combination of filters was evaluated from the calibration data. The normalised change in intensity ratio with temperature increases at higher temperatures, as shown in figure 6.18. This is because this filter combination effectively exploits the continuous redshift of the emission peak with increasing temperature. Given that the luminescence emission intensity decreases only slightly between 296 and 363 K, the precision in the intensity ratio is similar (table 6.1) and so the improvement in sensitivity at higher temperatures leads to increase in the temperature precision from 5.4 to 4.0 K at 363 K.

6.4.2 Error Analysis

Here the sources of error resulting from the dependence of the intensity ratio on the laser fluence are analysed in detail. Errors are quantified in two ways. First, errors arising from fluence variations that are not accounted for can be assessed, such as drift and fluctuation of the laser sheet profile. Secondly, the possible error (termed here 'calibration error') stemming from the assumption that the change in the normalised ratio is the same for all fluences is also addressed, using data shown in figure 6.16.

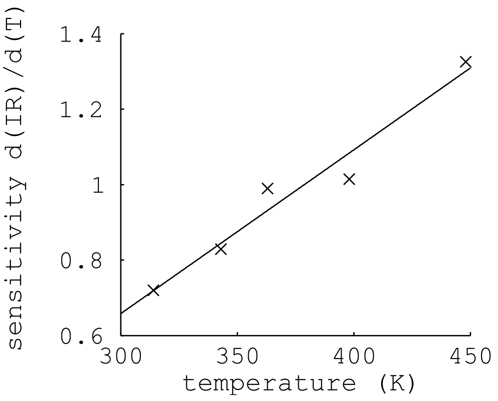

Figure 6.18: Normalised temperature sensitivity with temperature (%IR/K), evaluated using calibration data shown in figure 6.16.

Laser Fluence Error

The fixed variation in fluence within the laser sheet is accounted for by dividing by an average ratio image acquired at room temperature. While the particle position in the image plane is known, a particle will be illuminated by a different fluence depending on its depth position within the light sheet. At 10^{11} particles/m^3 there is at least one particle per 4 x 4 binned pixel and so the error contribution is considered negligible after smoothing (7 x 7).

Using this correction procedure, the sheet profile must not drift between the recording of room temperature normalisation sets and the actual experiment. The vertical pattern visible in the average images of figure 6.17 is attributed to such a drift, but the deviation from the mean temperature is only ± 4.6 K. Vertical profiles of the intensity ratio field were also compared on a shot-to-shot basis, and fluctuations were within the measurement noise and could not be distinguished. Shot-to-shot beam profiling is therefore not considered necessary using this particular laser.

For the experiments performed here, fluctuations in the laser pulse energy are approximately 10 %. Unaccounted for, the predicted error contribution is 6.2 K, which corresponds well to the measured shot-to-shot standard deviation of the average temperature (5.0 K). In these experiments pulse energies were measured on a shot-to-shot basis and after correction this error is reduced to 2.7 K.

Using this laser, it is anticipated that running at higher lamp energies and reducing the output energy with, for example, a half-wave plate, would improve both pulse-to-pulse stability and drift of the beam profile. Frame referencing can be used to remove these artefacts, by using a region or vertical strip of the image at a known temperature (a procedure that is often employed for Rayleigh imaging e.g. [136]) to correct images on a shot-to-shot or average basis.

Calibration Error

Figure 6.16 indicates that the maximum error stemming from the use of a calibration curve recorded at 20 mJ/cm^2 to process ratio images recorded at 5 mJ/cm^2 would be 7.2 K. In the same way, even though the laser fluence is accounted for where possible, the assumption that the curves collapse perfectly retains a calibration error. For example, in this experiment the light sheet optics formed a sheet that was diverging across the field of view, corresponding to to fluence variations of 50 and 5 % in the horizontal and vertical directions. Using a similar approach to determining the maximum error as illustrated in figure 6.16, this leads to possible calibration errors of 2.2 and 0.2 K respectively. Using a longer focal length lens or forming a uniform beam waist using a different combination of lenses will effectively remove these calibration errors. Alternatively, a beam homogeniser could be used [49].

6.5 Laser Fluence and Power Density Effects

In this section some trends observed in the preceding characterisation study are explored with additional measurements. Two reasons are proposed for the observed increase of the intensity ratio with excitation fluence.

Firstly, the laser could heat the particles. This would originate from non-radiative transitions, where excess energy is dissipated into the material as heat. This could be caused by the difference between the excitation and Stokes-shifted emission frequencies, which corresponds to an energy difference which will contribute to a heating effect; or non-radiative relaxation between the exciton states and valence band.

The calibration data of figure 6.16 at 5 mJ/cm^2 was used to interpret the evolution of intensity ratio with fluence in figure 6.13 in terms of temperature. Assuming the ratio increase is only due to a temperature increase of the particles, changing the fluence between 5 and 60 mJ/cm^2 leads to an observed temperature rise of $\sim$ 100 K as shown in figure 6.19.

Based on the measurements of the signal per particle for ZnO, and using the known camera specifications and collection efficiency, the number of photons emitted by a particle can be calculated. Assuming that, based on the SEM images, a probed particle consists of 100 agglomerated primary particles (200 nm diameter), and that the quantum efficiency of ZnO is 10% [77], using the known specific heat capacity and density of ZnO the temperature rise is predicted to be 34 K. This

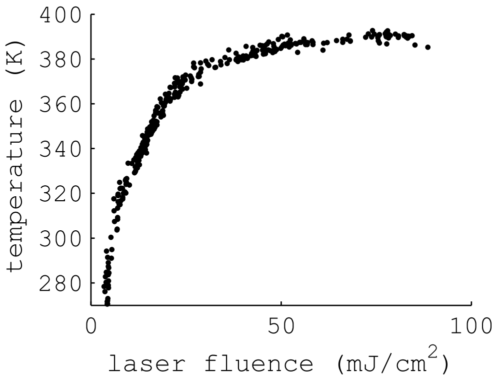

Figure 6.19: Assumed increase in the particle temperature with increasing laser fluence.

calculation indicates that laser-induced heating due to non-radiative relaxation is a plausible explanation for the observed trend in intensity ratio with fluence.

A second reason for the observed trend in the intensity ratio is that the power densities used in these measurements (and in many diagnostic techniques based on pulsed lasers), of the order MW/cm^2, affect the luminescence emission of ZnO. This was investigated using a second pulsed laser with a longer pulse duration. Using two lasers with fixed but different pulse durations allows independent variation of the laser fluence and power density.

Experimental Setup

For this purpose, in addition to the flashlamp-pumped laser used in the measurements described in this chapter, a DPSS laser (Hawk HP, Quantronix) was used. Triggered at 1 kHz, the laser produced 3 W (3 mJ/pulse). Overall power was measured using a thermoelectric power meter (HP 25S, Radiant Dyes).

To determine power densities, the temporal profiles of the excitation pulses were measured using a silicon photodiode (DET10A, Thorlabs) and an OD 1 UV neutral density filter. The pulse duration of the flashlamp-pumped laser was approximately 10 ns (FWHM). For the DPSS laser, attenuation of the radio frequency signal used to control the laser Q-switch was used to adjust the pulse energy almost independently of the pulse duration, which for the fixed drive current used in all measurements was approximately 170 ns.

Slight modifications to the laser sheet formation and camera settings were required. First, to achieve comparable fluences using the two laser systems, different cylindrical lenses were also used to alter the vertical height of the laser sheets. The sheet heights and thicknesses were monitored using the beam profiling system described in section 6.3.1. Second, the minimum repetition rate of the DPSS

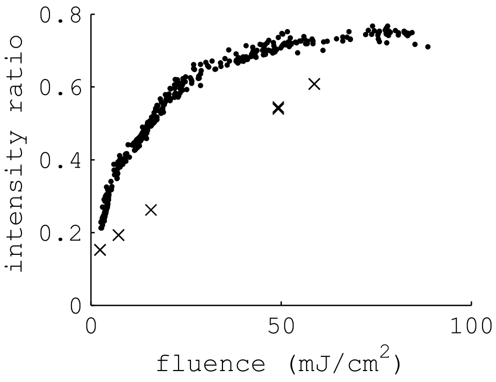

Figure 6.20: Effect of the laser fluence on the intensity ratio for excitation using pulse durations of 10 ns (dots) and 170 ns (crosses).

laser was 1 kHz. Consequently even at 4 x 4 the low extinction ratio (2000:1) of the CCD cameras (section 4.3) was not sufficient to completely attenuate the additional signal integrated by the cameras during readout when operated at the maximum frame rate of 10 Hz. Operation at 8 x 8 for measurements using the DPSS laser reduced the readout time so this contribution was eliminated, which was checked by acquiring images with the laser offset to only integrate pulses outside the exposure. Consistency between ratios measured with different binning was also verified.

Laser Fluence and Power Density

Measurements made with each laser system are shown in figure 6.20. For the same fluence, the difference in the measured intensity ratio using the two systems can be attributed to the difference in power density. This is consistent with an increasing redshift of the emission with power density, due to a decrease of the band gap width with increasing exciton density in the material [77].

Considering a fixed pulse duration, both the fluence and the power density increase with the laser energy. Also, as described above the plot shows that increasing the power density for a fixed fluence increases the intensity ratio. From these two observations, it can be deduced that the real temperature increase of the particles caused by laser excitation must be lower than that assumed in figure 6.19, because part of the intensity ratio increase can be attributed to an increased power density.

Saturation

The redshift of the emission, caused by laser-induced heating and increasing exciton density, ceases to occur beyond 60 mJ/cm^2. This suggests the particle temperature and exciton density stop increasing. A plausible explanation for this is that the particle stops absorbing and becomes transparent to the excitation light. The evolution of the emission intensity with laser fluence (see figure 6.13) displays a similar trend, supporting this explanation.

Since the luminescence lifetime (100's ps) is significantly shorter than the laser pulse duration (10 ns) it is presumed the processes of absorption and emission reach a steady state within the laser pulse. Considering excitation using lower laser energies where the signal increases linearly, increasing the rate of photon arrival (power density) promotes electrons into the conduction band at a faster rate. The rate of emission during the excitation pulse also increases to balance this increase in excitation rate, leading to higher luminescence signal. Further increasing the power density reaches a limit imposed by the finite lifetime of the emitting state and the total number of available emitting centres in the particle. Further increase of the absorption rate cannot occur.

6.6 Summary

A new tracer was characterised for temperature imaging. Direct comparison with 2 μm BAM:Eu phosphor particles indicate similar signal levels per particle and calibration measurements showed improved temperature sensitivity of ZnO. At room temperature a threefold improvement in temperature precision can be achieved for the same particle number density, laser fluence, luminescence collection and spatial resolution. Using a seeding density of 2×10^{11} particles/m^3 and a fluence of 5 mJ/cm^2, a precision of 5.4 K could be achieved. The signal decreases with temperature but the sensitivity increases significantly, leading to improved temperature precision (4.0 K, 1.1%) at 363 K.

A scheme to correct for the dependence of the intensity ratio on the laser fluence was demonstrated. The procedure is the same as an ordinary white field correction used for a typical ratio imaging experiment and requires no additional experimental effort. The errors arising from the laser are specific to the beam profile and pulse-to-pulse stability, and can be reduced or eliminated using corrective procedures. The residual calibration errors were evaluated over a range of fluences (5 to 20 mJ/cm^2), but shrinking this range in experiment and calibration reduces these errors to a negligible level. In terms of accuracy, the nominal 2.2 K accuracy of the type K thermocouple used for calibration must be considered, and for low temperature flows such as these more accurate reference measures could be used e.g. thermistors.

Laser-induced heating of the particles caused by non-radiative heat dissipation was identified as a plausible explanation for the increase in intensity ratio with laser fluence. Independent measurements of the dependence on power density showed that in the tested range of fluences, the high density of electron-hole pairs also causes a redshift of the emission, leading to an intensity ratio increase. Therefore, it is likely that both phenomena are responsible for the observed increase in the intensity ratio with fluence.

In this sense the absolute temperature of the particles is not important: the temperature increase due to the laser is repeatable and independent of heat transfer between the particles and gas during the short excitation times. In summary, for the purpose of practical temperature measurements the combined heating and power density effects are accounted for in the calibration, and the calibrated ratio has a sensitive dependence on absolute gas temperature.

Implications for Temperature Imaging using ZnO Particles

In comparing the demonstration experiments using ZnO with those using BAM:Eu in chapter 5, it is important to remember that the temperature precision depends on the particle number density, the laser fluence (if not operating in the saturated regime), the luminescence collection and the spatial resolution. Therefore the precision attained with each phosphor should only be compared for alike experimental conditions, as in section 6.3.2. From this, ZnO will always offer improved temperature precision over the tested range of temperatures.

SEM images indicate that the particles tested here have a primary size of 200 nm, forming agglomerated structures a few microns in size held together by static forces which may or may not be broken up in the seeder or flow. The relaxation times of these particles, which have a much larger surface area/volume ratio, will be considerably shorter than a spherical particle with the same projected area. This has important diagnostic implications for measurements in flows around room temperature and lower, where the relaxation time increases due to the decrease in gas thermal conductivity.

Regarding the range of investigated laser fluences, for sensitive kHz-rate measurements DPSS lasers must be used, and so the demonstration was performed at 5 mJ/cm^2. This is also true for experiments investigating larger measurement regions. However, the approach was shown to be valid for fluences up to 20 mJ/cm^2. The dependence of the intensity ratio on the fluence ceases beyond 60 mJ/cm^2, but this dependence cannot be avoided by operating in this regime because of laser-induced damage effects.

An important aspect of tracers for flow measurements is sensitivity to other parameters. ZnO:Zn and ZnO:Ga have been tested in oxygen concentrations 0-100% up to pressures of 4.5 bar and temperatures of 400 K with no effect on the emission spectrum [92]. ZnO nanowires have been used as sensors for oxygen concentration [137], but the material structure and size of the ZnO particles used here are similar to the tested ZnO:Zn and ZnO:Ga powders and will likely exhibit the same insensitivity to the surrounding gas.

Notably, signals in the gas using ZnO:Zn were approximately the same as using ZnO, although SEM images indicate that the agglomerated particles were evidently larger. Preliminary measurements show the temperature sensitivity of ZnO:Zn is lower than that reported by other groups [123], and is also lower than the ZnO used in this study. This indicates that testing of samples to evaluate signal and sensitivity is mandatory and there is no immediate justification for using intentionally doped powders. The commercially available, undoped powders used in this study are also cheap (as of 2014, $\sim$ 10's £/kg). However, given the sensitivity of the emission to deliberately added impurities it may be possible to significantly increase the signal and improve the temperature sensitivity of ZnO. Such investigations are essential areas of further work.

7 Conclusions and Future Work

Conclusions of the two main contributions presented in this thesis are summarised, along with immediate prospects for further investigation. Two practical applications are discussed: the study of film cooling flows in gas turbine combustors and in-cylinder flows in internal combustion engines. Motivated in part by the work presented here, focus areas for future development are highlighted.

7.1 Summary and Outlook

Time-Resolved Temperature and Velocity Imaging

Following on from the proof of concept work [15, 16], the measurement technique was developed and applied at kHz repetition rates, increasing the temporal resolution by three orders of magnitude. The experiments show that simultaneous time-resolved imaging of temperature and velocity can be achieved, using commercially available DPSS lasers and non-intensified high-speed CMOS cameras. From measurements in a turbulent heated jet, a temperature precision of better than 5% at 500 K was obtained. The measurements are the first example of sustained high repetition rate planar thermometry in an oxygen-containing environment. Combined with simultaneous velocity measurements, the technique promises to find immediate use for the investigation of transient, coupled heat and mass transfer phenomena.

Thermographic phosphors generally possess broad excitation spectra and emit visible luminescence. This is true for BAM:Eu, and specifically, it has a short luminescence lifetime and a high quantum efficiency. Previous work of our group indicates that neither the emission intensity or intensity ratio response of BAM:Eu are affected by oxygen concentrations of 0-200 mbar in the temperature range 300-900 K [16]. These features make the application of the technique an attractive concept at low repetition rates. At kHz rates, the advantages are more profound and even essential, since high-speed laser and camera technology is very limited. BAM:Eu can be directly excited using the frequency-tripled output of DPSS lasers, producing sufficient signal levels even in oxygen-containing environments. Detection of the luminescence does not require high-speed intensifiers, which avoids a number of issues that would make the quantitative imaging very difficult.

The high-speed CMOS cameras were characterised and found to be suitable for ratio-based imaging. The measurement precision is comparable to results obtained with low-speed, hardware-binned interline-transfer CCD cameras used previously [15]. Simulations indicate that the relative performance depends on the signal level, which in this work was optimised by significantly improving the overall transmission of the beamsplitter/filter combination.

The frame rate of high-speed CMOS cameras is rapidly evolving. As of 2014, the current generation of cameras runs at 20 kHz at 1,024 x 1,024 resolution (40 kHz at 1,024 x 512) [119], and the power output of DPSS lasers at higher repetition rates is also increasing, with lasers producing 50 W at 50 kHz (1 mJ/pulse) commercially available [138]. These advances would increase the sampling rate by more than a factor of ten and combined with large camera memories (64 Gb) measurement sequences covering four orders of magnitude of temporal scales are feasible. Therefore the perspectives for application of these diagnostics at much higher sampling rates, with no sacrifice in measurement precision, are very promising.

Precise Temperature Measurements using ZnO Particles

ZnO was selected and characterised as a temperature tracer. Using a seeding density of 2×10^{11} particles/m^3, a precision of 5.4 K was demonstrated at 296 K. The sensitivity increases with temperature so that at 363 K the temperature precision improves to 4.0 K. The demonstration experiments were performed at laser fluences easily achievable using frequency-tripled DPSS lasers. Therefore, ZnO can be used as a tracer for high precision kHz-rate measurements.

Results were compared to measurements using BAM:Eu particles. The emission per particle is similar for both phosphors and so the same intensity ratio precision can be achieved. Given the improved temperature sensitivity of ZnO, at 300 K a threefold improvement in the temperature precision can be realised. At 500 K, accounting for thermal quenching of the luminescence emission, a temperature precision of 3.0 K (0.6%) using 2×10^{11} particles/m^3 is feasible using ZnO. The sensitivity of BAM:Eu decreases with temperature, and so at 500 K the use of ZnO corresponds to a factor of seven improvement in the precision. In summary, between 300-500 K, for the same seeding density, luminescence collection and spatial resolution the use of ZnO ensures improved temperature precision.

This significantly extends the capabilities of the technique toward the study of flows with small temperature variations, essential for the investigation of natural convection and heat transfer. Also, for applications with diminished signal-to-noise ratios due to e.g. limited optical access or the use of the technique at high sampling rates, the use of ZnO may be necessary to maintain acceptable temperature precision.

The particles investigated here have a primary diameter of 200 nm but form agglomerates of 1-2 μm in size. These particles will have also have improved temperature tracing abilities due to the increase in the ratio of surface area to volume, improving the accuracy of the technique. Heat transfer to agglomerated structures could be investigated to determine the temperature response times, extending the approach presented in [16].

Additional measurements indicated that the intensity ratio dependence on the laser fluence is due to both the excess dissipation of absorbed energy leading to laser-induced heating, and the high power density causing a high concentration of electron-hole pairs in the particles. These results form the basis of further investigations of laser-induced heating of particles.

One of the novelties of this work was the use of semiconductors as a tracer. While doped ZnO was previously used for ratio-based temperature measurements [92], the possibility of using the undoped material was not recognised. Therefore the work represents the use of a completely different 'class' of phosphors (as discussed in chapter 3), all of them previously unused for thermometry. This presents new opportunities for further development, discussed below.

7.2 Future Work

7.2.1 Applications

Film Cooling Flows

Reduction of pollutant emissions, particularly NO_x, in gas turbine combustors is achieved using lean combustion. This increases the demand for fresh air in the combustor and reduces the amount of air available for cooling. One technique for more efficient cooling of combustor walls in modern gas turbine designs is angled effusion cooling, where a flow of air ('coolant') is directed through holes drilled at an angle in the combustor liner which then (ideally) spreads to form a protective film. Different configurations, e.g. trenched cooling holes (see figure 7.1), can be used to reduce mixing between coolant and combustion gases and encourage lateral spread of the coolant, reducing the cooling air requirement [139]. Currently, there is a lack of experimental investigation of the flow fields for even the simplest hole configurations, with most experimental studies based on cooling effectiveness measurements at the surface [140].

With the aim of improving the fundamental understanding the flow physics and the effects on the cooling performance, collaborative work with Universität der Bundeswehr München is currently being undertaken to obtain time-resolved temperature-velocity measurements. Different cylindrical and trenched hole geometries are being studied in a closed-loop wind tunnel. A cross-sectional view of the test section is shown in figure 7.1. Optical access into the section is from the side and through windows in the top panel, which can be seen from the pho-

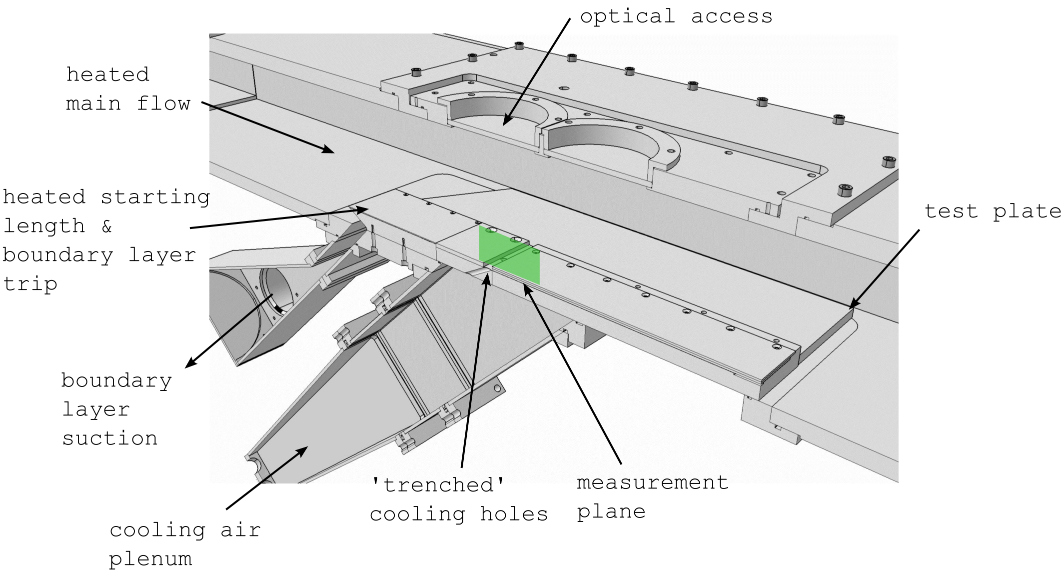

Figure 7.1: Streamwise cross-sectional view of the wind tunnel test section. Optical access is from above through windows in the top panel and the side (not shown).

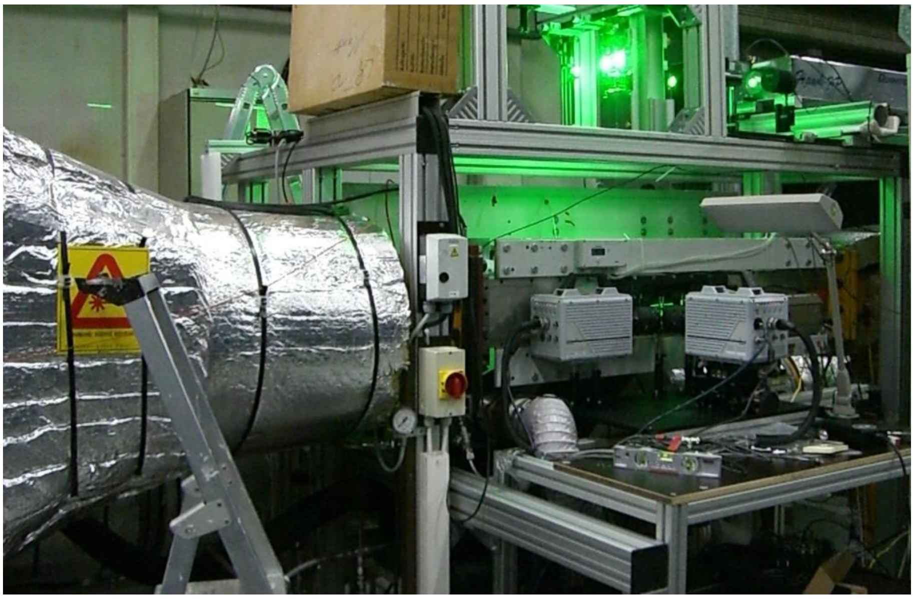

Figure 7.2: Photograph of the test section. The wind tunnel settling chamber is visible on the left (upstream) side. The three high-speed cameras are in the foreground; the two lasers are mounted above the test section.

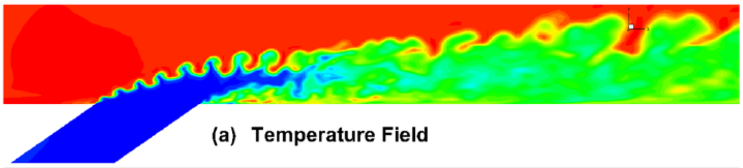
(a) Temperature Field

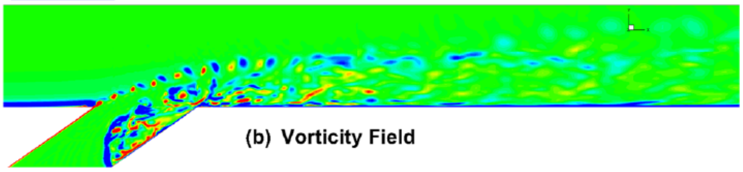
(b) Vorticity Field

Figure 7.3: Large eddy simulations of (a) temperature and (b) spanwise vorticity in an angled jet cooling flow. Kelvin-Helmholtz instabilities in the shear layer at the top of the jet are visible. From [141].

tograph (figure 7.2). The main flow can be heated to 370 K and the cooling air flow cryogenically cooled to 200 K to maintain representative dimensionless fluid parameters such as the density and momentum ratio between each gas stream. The phosphor ZnO will be used as a tracer, seeded into the main flow and cooling stream. The high-speed diagnostics are similar to those described in chapter 5, using two high-speed cameras and a frequency-tripled DPSS laser for phosphor excitation, in conjunction with a high-speed PIV system.

The large eddy simulation shown in figure 7.3 gives an indication of the temperature field in a similar flow. Kelvin-Helmholtz instabilities, amplified by the density difference between the two flows, are visible in the shear layer at the top of the jet. These instabilities are thought to lead to counter-rotating vortices aligned in the streamwise direction, which are considered detrimental to the cooling performance [141].

Measurements will be made on the central jet axis and in the symmetry planes between two cooling holes at a sampling rate of 6 kHz. The correlation of temperature and velocity which characterises the mixing of the coolant and hot gas in the shear layer will be studied. Measurements of the flow temperature and velocity adjacent to the surface will be used to investigate heat transfer and how this is affected by the mixing of cold and hot gas. From time-resolved datasets, the characteristic frequencies of the Kelvin-Helmholtz instabilities in the shear layer and of the coherent structures in the wake of the jet can be extracted. The results will also serve as validation data for future LES calculations performed at Universität der Bundeswehr München.

ZnO is sensitive at temperatures below 300 K, and is therefore suitable for measurements directly at the jet exit where the jet is unmixed. At these low temperatures, gaseous tracers such as toluene could not be used due to the low vapour pressure. This challenging application is a good example where the technique at kHz rates provides completely new measurement capabilities.

IC Engine Studies

In order to improve efficiency and maximise fuel efficiency, modern combustion concepts in IC engines usually involve operation near limits of stable combustion. In HCCI engines, fuel is injected early in the compression stroke and the lean mixture is compressed to autoignition. The combustion occurs at low temperatures, leading to very low NO_x emissions [4]. However control of the combustion phasing and high pressure rise rates are difficulties that must be overcome to bring an engine to market that runs effectively in HCCI mode for all or part of the operating range.

If the reaction takes place simultaneously everywhere in the combustion chamber, the resulting rapid pressure rise leads to pressure oscillations and possibly engine damage. Inhomogenities in the bulk gas temperature distribution have a favourable effect, by staggering ignition and moderating the rate of heat release [4]. These inhomogenities arise from the turbulent flow affecting the fuel and temperature stratification in the cylinder [142] and wall heat transfer effects [4, 143], but they vary from cycle to cycle. A better understanding of these fluctuating in-cylinder processes is necessary to improve engine design and operating strategies to minimise cycle to cycle variations [142]. Time-resolved measurements of the evolution of the temperature and velocity fields prior to combustion are required to determine how processes that are detrimental to engine performance occur.

Currently time-resolved imaging studies are limited to motored operation due to the requirement to run with nitrogen for toluene LIF, and only measurements up to 550 K have been demonstrated due to the strong quenching with temperature. The tracer will also be consumed during combustion. Phosphor particles could be used for such investigations in fired operation, allowing measurement much later in the compression cycle and into the low-temperature chemistry regime, and even after combustion. This may also be useful for the investigation of operating conditions with significant exhaust gas recirculation.

Solid phosphor particles have been used previously for low-speed engine measurements [68, 88, 144], with measurements locked to a particular crank angle. The evolving temperature and velocity fields during compression cannot be investigated on a cycle-to-cycle basis using low-speed measurements. Also for time-resolved studies, short measurement durations of just a few seconds can be used to measure multiple cycles, and particle deposition problems during these short times are not expected to be an issue. There have been no reports of significant damage to, for example, the valve seats or quartz ring/piston in optical engines. Most importantly, the pressure in the cylinder leads to higher particle number density even for low seeding at the intake, counteracting the effects of thermal quenching of the luminescence emission, and leading to high signal levels.

7.2.2 Technique Development

Semiconductors

ZnO with no deliberately added impurities was deliberately chosen for this work since it emits luminescence that can be used for thermometry. Preliminary measurements indicate that it is more sensitive than the ZnO deliberately fired to contain excess zinc, which is done to increase the intensity of the green luminescence for display applications. The amount of excess zinc is as low as 5-15 ppm [70]. However, the chemical assay of the ZnO used in this work has a purity just $> 99\%$, with many of the listed elements appearing at the 5-10 ppm range. Therefore it may possible to increase the emission intensity or increase the shift of the emission with temperature by changing the level or type of impurities. For example, introducing $\sim$ 1000 ppm gallium into ZnO (ZnO:Ga) was reported to increase the intensity of the edge luminescence by a factor of 17 [76]. Addition of indium and magnesium also leads to an increase in the emission intensity. Other direct gap semiconductors, e.g. gallium nitride (GaN), might offer benefits in terms of signal or sensitivity. Using these materials therefore provides exciting prospects for further improvements in the measurement technique.

Particles of a size similar to those used in this work were reported to be insensitive to the gas oxygen content [92]. However, previous applications for oxygen sensing using the electrical response of ZnO nanowires [137] (a cylindrical structure a few μm in length but only 10's nm in diameter) suggest nanoparticles of this scale could be seeded into flows for optical detection of oxygen and even other species. At low and intermediate temperatures (300-700 K) these diagnostics would be useful for the chemical processing industry. Samples consisting of needle-like micron-sized particles (Grillo Zinkoxid GmbH) have already been obtained. Further investigation is needed to determine whether there is sufficient signal and test the sensitivity of the luminescence emission to the gas composition.

Thermal quenching decreases the emission intensity of ZnO, but the increase in sensitivity with temperature leads to improved measurement precision at higher temperatures. Previous studies of aggregated powder demonstrated a spectral response up to 950 K, before the signal strength became too low to detect [92]. Characterisation of ZnO in the gas beyond 500 K is required to determine the upper temperature limit for this phosphor for flow measurements.

Alternative Phosphors

As measured by our group, the current tested range of BAM:Eu is 900 K [16]. Particularly for the study of high temperature reacting flows, means to increase the measurable temperature are needed.

There are two parallel strategies for this. One approach is to investigate other phosphors. Given there is an almost infinite range of phosphors, and the vast majority of them are completely investigated for any use let alone thermometry, this is a promising avenue of exploration. In general, phosphors useful for surface measurements at temperatures beyond 1000 K have a long luminescence lifetime, but short (μs) lifetimes seems to be a prerequisite for application in turbulent flows. However, the onset of thermal quenching usually occurs at a higher temperature for long lifetime phosphors, and so there may be a range where such a phosphor might perform better. Different combinations of host and dopant can produce marked differences in the emission and potentially increased signal, for example doping divalent europium in different hosts. The dopant concentration can also be varied. It should be noted that for most commercially available phosphors this may be optimised for the lighting industry, for different excitation wavelengths or even completely different means of excitation e.g. electron beams.

A second approach is to change the laser excitation. Similar to this work, where power density effects were investigated for ZnO, and in earlier work by our group using BAM:Eu where the excitation wavelength and linewidth were varied to investigate the effect on the luminescence intensity [16], there are good prospects for a substantial gain in signal. Changing the laser pulse wavelength, linewidth and duration may increase the limit of the saturation behaviour identified for these two phosphors.

These two approaches are complementary, and the systematic testing of new and existing phosphors for different excitation conditions will be the focus of further research.

Understanding which luminescence properties are favourable for phosphors suitable for flow temperature measurements, and how a typical experiment should be set up to ensure success, has taken the initial concept to a working measurement technique. The developments presented in this thesis are representative of significant progress in both these areas. By choosing a different phosphor, and characterising and implementing appropriate instrumentation, major advances in the capabilities of the technique can be made. The technique is now sufficiently mature to apply to several demanding applications. Exploring the vast range of phosphors and different ways to probe them will surely lead to further novel developments in the utility of the technique for flow measurements.

References

[1] A.C. Eckbreth. *Laser Diagnostics for Combustion Temperature and Species.* Gordon and Breach, second edition, 1996.

[2] R.S. Barlow. Laser diagnostics and their interplay with computations to understand turbulent combustion. *Proc. Combust. Inst.*, 31:49–75, 2007.

[3] K.N.C. Bray. The challenge of turbulent combustion. *Proc. Combust. Inst.*, 26:1–26, 1996.

[4] J.E. Dec. Advanced compression-ignition engines - understanding the in-cylinder processes. *Proc. Combust. Inst.*, 32:2727–2742, 2009.

[5] R.K. Hanson. Combustion diagnostics: planar imaging techniques. *Proc. Combust. Inst.*, 21:1677–1691, 1986.

[6] B. Böhm, C. Heeger, R.L. Gordon, and A. Dreizler. New perspectives on turbulent combustion: multi-parameter high-speed planar laser diagnostics. *Flow Turb. Combust.*, 86:313–341, 2011.

[7] V. Sick. High speed imaging in fundamental and applied combustion research. *Proc. Combust Inst.*, 34:3509–3530, 2013.

[8] B. Thurow, N. Jiang, and W. Lempert. Review of ultra-high repetition rate laser diagnostics for fluid dynamic measurements. *Meas. Sci. Technol.*, 24:22pp, 2013.

[9] B. Böhm, J. Brübach, C. Ertem, and A. Dreizler. Experiments for combustion LES validation. *Flow Turb. Combust.*, 80:507–529, 2008.

[10] E.D. Siggia. High Rayleigh number convection. *Annu. Rev. Fluid Mech.*, 26:137–168, 1994.

[11] S.K. Robinson. Coherent motions in the turbulent boundary layer. *Annu. Rev. Fluid Mech.*, 23:601–639, 1991.

[12] R. du Puits, L. Li, C. Resagk, A. Thess, and C. Willert. Turbulent Boundary Layer in High Rayleigh Number Convection in Air. *Phys. Rev. Lett.*, 112:1–5, 2014.

[13] P.A. Libby and F.A. Williams. *Turbulent Reacting Flows.* Springer-Verlag, Topics in Applied Physics vol. 44, 1980.

[14] J. Warnatz, U. Mass, and R.W. Dibble. *Combustion.* Springer, second edition, 1999.

[15] B. Fond, C. Abram, A.L. Heyes, A.M. Kempf, and F. Beyrau. Simultaneous temperature, mixture fraction and velocity imaging in turbulent flows using thermographic phosphor tracer particles. *Opt. Express*, 20:22118–22133, 2012.

[16] B. Fond. *Simultaneous Temperature and Velocity Measurements in Turbulent Flows using Thermographic Phosphor Tracer Particles.* PhD thesis, Imperial College, UK, 2014.

[17] D. Most and A. Leipertz. Simultaneous two-dimensional flow velocity and gas temperature measurements by use of a combined particle image velocimetry and filtered Rayleigh scattering technique. *Appl. Opt.*, 40:5379–5387, 2001.

[18] I. Boxx, C. Heeger, R. Gordon, B. Böhm, M. Aigner, A. Dreizler, and W. Meier. Simultaneous three-component PIV / OH-PLIF measurements of a turbulent lifted, C_3H_8-Argon jet diffusion flame at 1.5 kHz repetition rate. *Proc. Combust. Inst.*, 32:905–912, 2009.

[19] M. Stöhr, I. Boxx, C. Carter, and W. Meier. Dynamics of lean blowout of a swirl-stabilized flame in a gas turbine model combustor. *Proc. Combust. Inst.*, 33:2953–2960, 2011.

[20] A. Johchi, M. Tanahashi, M. Shimura, G. Choi, and T. Miyauchi. High Repetition Rate Simultaneous CH / OH PLIF in Turbulent Jet Flame. *16th Int. Symp. on Applications of Laser Techniques to Fluid Mechanics*, 2012.

[21] P.J. Trunk, I. Boxx, C. Heeger, W. Meier, B. Böhm, and A. Dreizler. Premixed flame propagation in turbulent flow by means of stereoscopic PIV and dual-plane OH-PLIF at sustained kHz repetition rates. *Proc. Combust. Inst.*, 34:3565–3572, 2013.

[22] C.M. Fajardo, J.D. Smith, and V. Sick. Sustained simultaneous high-speed imaging of scalar and velocity fields using a single laser. *Appl. Phys. B-Lasers O*, 85:25–31, 2006.

[23] J.D. Smith and V. Sick. Quantitative, dynamic fuel distribution measurements in combustion-related devices using laser-induced fluorescence imaging of biacetyl in iso-octane. *Proc. Combust. Inst.*, 31:747–755, 2007.

[24] B. Peterson and V. Sick. Simultaneous flow field and fuel concentration imaging at 4.8 kHz in an operating engine. *Appl. Phys. B-Lasers O*, 97:887–895, 2009.

[25] R.L Gordon, C. Heeger, and A. Dreizler. High-speed mixture fraction imaging. *Appl. Phys. B-Lasers O*, 96:745–748, 2009.

[26] M. Gamba and R.K. Hanson. Cinematographic PLIF Imaging of Toluene Using CW Excitation. *16th Int. Symp. on Applications of Laser Techniques to Fluid Mechanics*, 2012.

[27] V.A. Miller, V.A. Troutman, and R.K. Hanson. Near-kHz 3D tracer-based LIF imaging of a co-flow jet using toluene. *Meas. Sci. Technol.*, 25:1–10, 2014.

[28] I. Boxx, O. Heinold, and K.P. Geigle. Laser-induced incandescence measurements in a fired Diesel engine at 3 kHz. *16th Int. Symp. on Applications of Laser Techniques to Fluid Mechanics*, 2014.

[29] A.M. Steinberg, I. Boxx, C.M. Arndt, J. H. Frank, and W. Meier. Experimental study of flame-hole reignition mechanisms in a turbulent non-premixed jet flame using sustained multi-kHz PIV and crossed-plane OH PLIF. *Proc. Combust. Inst.*, 33:1663–1672, 2011.

[30] B. Böhm, C. Heeger, I. Boxx, W. Meier, and A. Dreizler. Time-resolved conditional flow field statistics in extinguishing turbulent opposed jet flames using simultaneous highspeed PIV / OH-PLIF. *Proc. Combust. Inst.*, 32:1647–1654, 2009.

[31] B. Peterson, D.L. Reuss, and V. Sick. On the ignition and flame development in a spray-guided direct-injection spark-ignition engine. *Combust. Flame*, 161:240–255, 2014.

[32] B. Peterson, D.L. Reuss, and V. Sick. High-speed imaging analysis of misfires in a spray-guided direct injection engine. *Proc. Combust. Inst.*, 33:3089–3096, 2011.

[33] A.M. Steinberg, I. Boxx, M. Stöhr, C.D. Carter, and W. Meier. Flow flame interactions causing acoustically coupled heat release fluctuations in a thermo-acoustically unstable gas turbine model combustor. *Combust. Flame*, 157:2250–2266, 2010.

[34] R.A. Patton, K.N. Gabet, N. Jiang, W.R. Lempert, and J.A Sutton. Multi-kHz mixture fraction imaging in turbulent jets using planar Rayleigh scattering. *Appl. Phys. B-Lasers O*, 106:457–471, 2012.

[35] N. Jiang, R.A. Patton, W.R. Lempert, and J.A. Sutton. Development of high-repetition rate CH PLIF imaging in turbulent non-premixed flames. *Proc. Combust. Inst.*, 33:767–774, 2011.

[36] J.B. Michael, P. Venkateswaran, J.D. Miller, M.N. Slipchenko, J.R. Gord, S. Roy, and T.R. Meyer. 100 kHz thousand-frame burst-mode planar imaging in turbulent flames. *Opt. Lett.*, 39:739–742, 2014.

[37] R.A. Patton, K.N. Gabet, N. Jiang, W.R. Lempert, and J.A. Sutton. Multi-kHz temperature imaging in turbulent non-premixed flames using planar Rayleigh scattering. *Appl. Phys. B-Lasers O*, 108:377–392, 2012.

[38] M.J. Papageorge, T.A. McManus, F. Fuest, and J.A. Sutton. Recent advances in high-speed planar Rayleigh scattering in turbulent jets and flames: increased record lengths, acquisition rates, and image quality. *Appl. Phys. B-Lasers O*, 115:197–213, 2014.

[39] C. Schulz and V. Sick. Tracer-LIF diagnostics: quantitative measurement of fuel concentration, temperature and fuel/air ratio in practical combustion systems. *Prog. Energ. Combust.*, 31:75–121, 2005.

[40] R. Devillers, G. Bruneaux, and C. Schulz. Investigation of toluene LIF at high pressure and high temperature in an optical engine. *Appl. Phys B-Lasers O*, 96:735–739, 2009.

[41] W. Koban, J.D. Koch, R.K. Hanson, and C. Schulz. Oxygen quenching of toluene fluorescence at elevated temperatures. *Appl. Phys. B-Lasers O*, 80:777–784, 2005.

[42] M. Luong, R. Zhang, C. Schulz, and V. Sick. Toluene laser-induced fluorescence for in-cylinder temperature imaging in internal combustion engines. *Appl. Phys. B-Lasers O*, 91:669–675, 2008.

[43] M. Cundy, P. Trunk, A. Dreizler, and V. Sick. Gas-phase toluene LIF temperature imaging near surfaces at 10 kHz. *Exp. Fluids*, 1:1169–1176, 2011.

[44] B. Peterson, E. Baum, B. Böhm, V. Sick, and A. Dreizler. High-speed PIV and LIF imaging of temperature stratification in an internal combustion engine. *Proc. Combust. Inst.*, 34:3653–3660, 2013.

[45] B. Peterson, E. Baum, B. Böhm, V. Sick, and A. Dreizler. Spray-induced temperature stratification dynamics in a gasoline direct-injection engine. *Proc. Combust. Inst.*, In press: http://dx.doi.org/10.1016/j.proci.2014.06.103:1–9, 2014.

[46] S.A. Kaiser, M. Schild, and C. Schulz. Thermal stratification in an internal combustion engine due to wall heat transfer measured by laser-induced fluorescence. *Proc. Combust. Inst.*, 34:2911–2919, 2013.

[47] B. Peterson, E. Baum, B. Böhm, V. Sick, and A. Dreizler. Evaluation of toluene LIF thermometry detection strategies applied in an internal combustion engine. *Appl. Phys. B-Lasers O*, 117:115–175, 2014.

[48] V. Weber, J. Brübach, R.L. Gordon, and A. Dreizler. Pixel-based characterisation of CMOS high-speed camera systems. *Appl. Phys. B-Lasers O*, 103:421–433, 2011.

[49] S. Pfadler, F. Beyrau, M. Löffler, and A. Leipertz. Application of a beam homogenizer to planar laser diagnostics. *Opt. Express*, 14:10171–10180, 2006.

[50] M.C. Thurber, F. Grisch, and R.K. Hanson. Temperature imaging with single- and dual-wavelength acetone planar laser-induced fluorescence. *Opt. Lett.*, 22:251–253, 1997.

[51] S. Einecke, C. Schulz, and V. Sick. Measurement of temperature, fuel concentration and equivalence ratio fields using tracer LIF in IC engine combustion. *Appl. Phys. B-Lasers O*, 71:717–723, 2000.

[52] M.C. Thurber, F. Grisch, B.J. Kirby, M. Votsmeier, and R.K. Hanson. Measurements and modeling of acetone laser-induced fluorescence with implications for temperature-imaging diagnostics. *Appl. Opt.*, 37:4963–4978, 1997.

[53] M. Löffler, F. Beyrau, and A. Leipertz. Acetone laser-induced fluorescence behavior for the simultaneous quantification of temperature and residual gas distribution in fired spark-ignition engines. *Appl. Opt.*, 49:37–49, 2009.

[54] P.R. Medwell, Q.N. Chan, B.B. Dally, T. Alwahabi, S. Mahmoud, G.F. Metha, and G.J. Nathan. Flow seeding with elemental metal species via an optical method. *Appl. Phys. B-Lasers O.*, 107:665–668, 2012.

[55] S.M. Mahmoud, G.J. Nathan, P.R. Medwell, B.B. Dally, and Z.T. Alwahabi. Simultaneous planar measurements of temperature and soot volume fraction in a turbulent non-premixed jet flame. *Proc. Combust. Inst.*, In press: http://dx.doi.org/10.1016/j.proci.2014.06.122, 2014.

[56] C.F. Kaminski, J. Engström, and M. Aldén. Quasi-instantaneous two-dimensional temperature measurements in a spark ignition engine using 2-line atomic fluorescence. *Proc. Combust. Inst.*, 27:85–93, 1998.

[57] P.R. Medwell, Q.N. Chan, P.A.M. Kalt, T. Alwahabi, B.B. Dally, and G.J. Nathan. Development of temperature imaging using two-line atomic fluorescence. *Appl. Opt.*, 48:1237–1248, 2009.

[58] M. Aldén, P. Grafström, H. Lundberg, and S. Svanberg. Spatially resolved temperature measurements in a flame using laser-excited two-line atomic fluorescence and diode-array detection. *Opt. Lett.*, 8:241–243, 1983.

[59] J. Dec and J.O. Keller. High speed thermometry using two-line atomic fluorescence. *Proc. Combust. Inst.*, 21:1737–1745, 1986.

[60] B.K. McMillin, J.L. Palmer, and R.K. Hanson. Temporally resolved, two-line fluorescence imaging of NO temperature in a transverse jet in a supersonic cross flow. *Appl. Opt.*, 32:7532–7545, 1993.

[61] J.M. Seitzmann and R.K. Hanson. Two-Line Planar Fluorescence for Temporally Resolved Temperature Imaging in a Reacting Supersonic Flow over a Body. *Appl. Phys. B-Lasers O.*, 57:385–391, 1993.

[62] R. Giezendanner-Thoben, U. Meier, W. Meier, J. Heinze, and M. Aigner. Phase-locked two-line OH planar laser-induced fluorescence thermometry in a pulsating gas turbine model combustor at atmospheric pressure. *Appl. Opt.*, 44:6505–6577, 2005.

[63] S.W. Allison and G.T. Gillies. Remote thermometry with thermographic phosphors: Instrumentation and applications. *Rev. Sci. Instrum.*, 68:2615–2649, 1997.

[64] D.L. Beshears, G.J. Capps, M.R. Cates, C.M. Simmons, and S.W. Schwenterly. Laser-induced fluorescence of phosphors for remote cryogenic thermometry. Technical report, ORNL, 1990.

[65] M.R. Cates, S.W. Allison, S.L. Jaiswal, and D.L. Beshears. YAG:Dy and YAG:Tm Fluorescence Above 1400°C. Technical report, ORNL, 2003.

[66] J. Brübach, A. Dreizler, and J. Janicka. Gas compositional and pressure effects on thermographic phosphor thermometry. *Meas. Sci. Technol.*, 18:764–770, 2007.

[67] J.P. Feist, A.L. Heyes, and S. Seefeldt. Oxygen quenching of phosphorescence from thermographic phosphors. *Meas. Sci. Technol.*, 14:17–20, 2003.

[68] R. Hasegawa, J. Sakata, H. Yanagihara, B. Johansson, A. Omrane, and M. Aldén. Two-dimensional gas-phase temperature measurements using phosphor thermometry. *Appl. Phys. B-Lasers O*, 88:291–296, 2007.

[69] A. Omrane, P. Petersson, M. Aldén, and M.A. Linne. Simultaneous 2D flow velocity and gas temperature measurements using thermographic phosphors. *Appl. Phys. B-Lasers O*, 92:99–102, 2008.

[70] W.M. Yen, S. Shionoya, and H. Yamamoto. *Phosphor Handbook.* CRC Press, second edition, 2007.

[71] C. Ronda. *Luminescence: From Theory to Applications.* Wiley VCH, first edition, 2008.

[72] E.F. Gurnee. Fundamental principles of semiconductors. *J. Chem. Educ.*, 46:80–85, 1969.

[73] B. Henderson and G.F. Imbusch. *Optical Spectroscopy of Inorganic Solids.* Oxford Science Publications, first edition, 1989.

[74] G. Blasse and B.C. Grabmaier. *Luminescent Materials.* Springer, second edition, 1994.

[75] H. Morkoç and Ü. Özgür. *Zinc oxide: Fundamentals, materials and Device Technology.* Wiley-VCH, first edition, 2009.

[76] P.A. Rodnyi and I.V. Khodyuk. Optical and luminescence properties of zinc oxide: a review. *Opt. Spectrosc.*, 111:776–785, 2011.

[77] C. Klingshirn. ZnO: Material, Physics and Applications. *Chem. Phys. Chem.*, 8:782 – 803, 2007.

[78] H.L. Heys. *Physical Chemistry.* Harrap London, fourth edition, 1980.

[79] A.R. West. *Solid State Chemistry and its Applications.* Wiley, second edition, 2014.

[80] J. Brübach, J.P. Feist, and A. Dreizler. Characterization of manganese-activated magnesium fluorogermanate with regards to thermographic phosphor thermometry. *Meas. Sci. Technol.*, 19:11pp, 2008.

[81] S.D. Alaruri, A.J. Brewington, M.A. Thomas, and J.A. Miller. High-temperature remote thermometry using laser-induced fluorescence decay lifetime measurements of Y_2O_3:Eu and YAG:Tb thermographic phosphors. *IEEE T. Instrum. Meas.*, 42:735–739, 1993.

[82] J. Brübach, M. Hage, J. Janicka, and A. Dreizler. Simultaneous phosphor and CARS thermometry at the wall-gas interface within a combustor. *Proc. Combust. Inst.*, 32:855–861, 2009.

[83] A. Omrane, G. Juhlin, F. Ossler, and M. Aldén. Temperature measurements of single droplets by use of laser-induced phosphorescence. *Appl. Opt.*, 43:3523–3529, 2004.

[84] A. Omrane, G. Särner, and M. Aldén. 2D-temperature imaging of single droplets and sprays using thermographic phosphors. *Appl. Phys. B-Lasers O*, 79:431–434, 2004.

[85] A. Omrane, F. Ossler, and M. Aldén. Two-dimensional surface temperature measurements of burning materials. *Proc. Combust. Inst*, 29:2653–2659, 2002.

[86] J. Brübach, T. Kissel, and A. Dreizler. Phosphor thermometry in an optically accessible internal combustion engine. Technical report, FG Energie und Kraftwerkstechnik, TU Darmstadt, 2010.

[87] N. Fuhrmann, M. Schild, D. Bensing, S.A. Kaiser, C. Schulz, J Brübach, and A. Dreizler. Two-dimensional cycle-resolved exhaust valve temperature measurements in an optically accessible internal combustion engine using thermographic phosphors. *Appl. Phys. B-Lasers O*, 106:945–951, 2012.

[88] S. Someya, Y. Okura, M. Uchida, Y. Sato, and K. Okamoto. Combined velocity and temperature imaging of gas flow in an engine cylinder. *Opt. Lett.*, 37:4964–4966, 2012.

[89] G. Särner, A. Omrane, H. Seyfried, M. Richter, H. Schmidt, and M. Aldén. Laser diagnostics applied to a full-size fighter-jet afterburner. Technical report, Division of Combustion Physics, Lund Institute of Technology and Volvo Aero Corporation, 2005.

[90] A.L. Heyes, S. Seefeldt, and J.P. Feist. Two-colour phosphor thermometry for surface temperature measurement. *Optics Laser Technol.*, 39:257–265, 2006.

[91] J. Brübach, A. Patt, and A. Dreizler. Spray thermometry using thermographic phosphors. *Appl. Phys. B-Lasers O*, 83:499–502, 2006.

[92] G. Särner, M. Richter, and M. Aldén. Two-dimensional thermometry using temperature-induced line-shifts of ZnO:Zn and ZnO:Ga fluorescence. *Opt. Lett.*, 33:1327–1329, 2008.

[93] M. Lawrence, H. Zhao, and L. Ganippa. Gas phase thermometry of hot turbulent jets using laser induced phosphorescence. *Opt. Express*, 21:12260–12281, 2013.

[94] J.P.J. van Lipzig, M. Yu, N.J. Dam, C. C. M. Luijten, and L. P. H. de Goey. Gas-phase thermometry in a high-pressure cell using $BaMgAl_{10}O_{17}$:Eu as a thermographic phosphor. *Appl. Phys. B -Lasers O*, 111:469–481, 2013.

[95] D.A. Rothamer and J. Jordan. Planar imaging thermometry in gaseous flows using upconversion excitation of thermographic phosphors. *Appl. Phys. B-Lasers O*, 106:435–444, 2012.

[96] J. Jordan and D.A. Rothamer. Pr:YAG temperature imaging in gas-phase flows. *Appl. Phys. B-Lasers O*, 110:285–291, 2012.

[97] C. Abram, B. Fond, A.L. Heyes, and F. Beyrau. High-speed planar thermometry and velocimetry using thermographic phosphor particles. *Appl. Phys. B-Lasers O*, 111:155–160, 2013.

[98] C.T. Bohren and D.R. Huffman. *Absorption and scattering of light by small particles*. Wiley, first edition, 1983.

[99] Oregon Medical Laser Center. http://omlc.org/calc/miecalc.html. Accessed July 2014.

[100] M. Raffel, C.E. Willert, S.T. Wereley, and J. Kompenhans. *Particle Image Velocimetry: A Practical Guide*. Springer, second edition, 2007.

[101] F. Durst, A. Melling, and J.H. Whitelaw. *Principles and practice of laser doppler anemometry*. Academic Press, second edition, 1981.

[102] A. Melling. Tracer particles and seeding for particle image velocimetry. *Meas. Sci. Technol.*, 8:1406–1416, 1997.

[103] P.H. Klein and W.J. Croft. Thermal Conductivity, Diffusivity, and Expansion of Y_2O_3, $Y_3Al_5O_{12}$, and LaF_3 in the Range 77°-300 °K. *J. Appl. Phys.*, 38:1603–1607, 1967.

[104] F.P. Incropera, D.P. deWitt, T.L. Bergman, and A.S. Lavine. *Introduction to Heat Transfer*. Wiley, sixth edition, 2007.

[105] N. Konopliv and E.M. Sparrow. Transient heat conduction in nonhomogeneous spherical systems. *J. Heat Mass Transfer*, 3:197–210, 1970.

[106] J. Brübach, C. Pflitsch, A. Dreizler, and B. Atakan. On surface temperature measurements with thermographic phosphors: A review. *Prog. Energ. Combust.*, 39:37–60, 2013.

[107] J. Brübach, T. Kissel, M. Frotscher, M. Euler, B. Albert, and A. Dreizler. A survey of phosphors novel for thermography. *J. Lumin.*, 131:559–564, 2011.

[108] M. Rhodes. *Introduction to Particle Technology*. Wiley, first edition, 1998.

[109] M. Glass and I.M. Kennedy. An improved seeding method for high temperature laser doppler velocimetry. *Combust. Flame*, 29:333–335, 1977.

[110] B. Fond, C. Abram, and F. Beyrau. On the characterisation of tracer particles for thermographic particle image velocimetry. *Appl. Phys. B-Lasers O*, DOI 10.1007/s00340-014-5997-5, 2015.

[111] C.F. Kaminski, J. Hult, and M. Aldén. High repetition rate planar laser induced fluorescence of OH in a turbulent non-premixed flame. *Appl. Phys. B-Lasers O*, 68:757–760, 1999.

[112] Spectral Energies LLC. http://spectralenergies.com/products/pulse-burst-laser-system/. Accessed August 2014.

[113] M.N. Slipchenko, J.D. Miller, S. Roy, T.R. Meyer, J.G. Mance, and J.R. Gord. 100 kHz, 100 ms, 400 J burst-mode laser with dual-wavelength diode-pumped amplifiers. *Opt. Lett.*, 39:4735–4738, 2014.

[114] D.W. Hughes and J.R.M. Barr. Laser diode pumped solid state lasers. *J. Phys. D: Appl. Phys.*, 25:563–586, 1992.

[115] C. Kittler and A. Dreizler. Cinematographic imaging of hydroxyl radicals in turbulent flames by planar laser-induced fluorescence up to 5 kHz repetition rate. *Appl. Phys. B-Lasers O*, 89:163–166, 2007.

[116] M. Cundy and V. Sick. Hydroxyl radical imaging at kHz rates using a frequency-quadrupled Nd:YLF laser. *Appl. Phys. B-Lasers O*, 96:241–245, 2009.

[117] Tech Imaging. http://www.techimaging.com/hadland-imaging/uhsi-ultra-high-speed-framing-camera. Accessed September 2014.

[118] Shimadzu Scientific Instruments. http://www.ssi.shimadzu.com/products/. Accessed September 2014.

[119] Photron Ltd. http://photron.com. Accessed September 2014.

[120] G.C. Holst and T.S. Lomheim. *CMOS/CCD sensors and camera systems.* SPIE Press, second edition, 2011.

[121] D. Dussault and P. Hoess. Noise performance comparison of ICCD with CCD and EMCCD cameras. Technical report, Stanford Computer Optics, 2004.

[122] LaVision GmbH. High-speed IRO manual, 1004690 HS-IRO Controller D81.

[123] G. Särner, M Richter, and M. Aldén. Investigations of blue emitting phosphors for thermometry. *Meas. Sci. Technol.*, 19:1–10, 2008.

[124] S.M. Soloff, R.J. Adrian, and Z.C. Liu. Distortion compensation for generalised stereoscopic particle image velocimetry. *Meas. Sci. Technol.*, 8:1441–1454, 1997.

[125] G.H. Wang and N.T. Clemens. Effects of imaging system blur on measurements of flow scalars and scalar gradients. *Exp. Fluids*, 37:194–205, 2004.

[126] S.A. Kaiser and J.H. Frank. The effects of laser-sheet thickness on dissipation measurements in turbulent non-reacting jets and jet flames. *Meas. Sci. Technol.*, 22:15pp, 2011.

[127] C.H.K. Williamson. Three-Dimensional Vortex Dynamics in Bluff Body Wakes. *Exp. Therm. Fluid Sci.*, 12:150–168, 1996.

[128] C.H.K. Williamson. Vortex dynamics in the cylinder wake. *Annu. Rev. Fluid Mech.*, 28:477–539, 1996.

[129] B. Li, J. Lindén, Z.S. Li, A.A. Konnov, M. Aldén, and L.P.H. de Goey. Accurate measurements of laminar burning velocity using the Heat Flux method and thermographic phosphor technique. *Proc. Combust. Inst.*, 33:939–946, 2010.

[130] Z. Fan and G.L. Jia. Zinc oxide nanostructures: synthesis and properties. *J. Nanosci. Nanotech*, 5:1561–1573, 2005.

[131] L. Schneider, S. Halm, G. Bacher, A. Roy, and F.E. Kruis. Photoluminescence spectroscopy of single crystalline ZnO-nanoparticles from the gas phase. *Phys. Stat. Sol. C*, 3:1014–1017, 2006.

[132] Z.S. Liu, X.P. Jing, H.W. Song, and L.B. Fan. The relationships between UV emission and green emission in ZnO phosphor. *Acta. Phys. Chim. Sin.*, 22:1383–1387, 2006.

[133] V.M. Markushev, M.V. Ryzhkov, C.M. Briskina, H. Cao, L.A. Zadorozhnaya, L.E. Li, E.I. Gevargizov, and L.N. Demianets. UV radiation of powdered ZnO pumped by nanosecond pulses. *Proc. SPIE*, 5924:1–8, 2005.

[134] D. Anglos, A. Stassinopoulos, R.N. Das, G. Zacharakis, M. Psyllaki, R. Jakubiak, R.A. Vaia, E.P. Giannelis, and S.H. Anastsiadis. Random laser action in organic-inorganic nanocomposites. *J. Opt. Soc. Am. B*, 21:208–213, 2004.

[135] S. Pfadler, F. Dinkelacker, F. Beyrau, and A. Leipertz. High resolution dual-plane stereo-PIV for validation of subgrid scale models in large-eddy simulations of turbulent premixed flames. *Combust. Flame*, 56:1552–1564, 2009.

[136] J.H. Frank, S.A. Kaiser, and M.B. Long. Multiscalar imaging in partially premixed jet flames with argon dilution. *Combust. Flame*, 143:507–523, 2005.

[137] M. Jeoing, B. Oh, O. Nam, T. Kim, and J. Myoung. Three-dimensional ZnO hybrid nanostructures for oxygen sensing application. *Nanotechnology*, 1:526–530, 2006.

[138] Lee Laser Inc. http://leelaser.com/category/Series-LDP—UV-Industrial-Lasers. Accessed September 2014.

[139] A.H. Lefebvre and D.R. Ballal. *Gas Turbine Combustion: Alternative Fuels and Emissions*. CRC Press, first edition, 2010.

[140] P. Schreivogel, B. Kröss, and M. Pfitzner. Density ratio effects on the flow field emanating from cylindrical effusion and trenched film cooling holes. *Proceedings of ASME Turbo Expo 2014: Turbine Technical Conference and Exposition 2014*, 2014.

[141] P. Kalghatgi and S. Acharya. Modal analysis of inclined film cooling jet flow. *J. Turbomech.*, 136:11pp, 2014.

[142] W. Eckerle and C. Rutland. A Workshop to Identify Research Needs and Impacts in Predictive Simulation for Internal Combustion Engines (PreSICE). Technical report, US Department of Energy, 2011.

[143] C. Jainski, L. Lu, A. Dreizler, and V. Sick. High-speed micro particle image velocimetry studies of boundary-layer flows in a direct-injection engine. *Int. J. Engine Res.*, 2013.

[144] N.J. Neal, J. Jordan, and D. Rothamer. Simultaneous Measurements of In-Cylinder Temperature and Velocity Distribution in a Small-Bore Diesel Engine Using Thermographic Phosphors. *SAE Int. J. Engines*, 6:19pp, 2013.

List of Publications and Conference Proceedings

C. Abram, B. Fond and F. Beyrau, *Characterisation of zinc oxide thermographic phosphor particles for combined temperature and velocity measurements in turbulent flows*, to be submitted to Optics Express

B. Fond, C. Abram and F. Beyrau, *Quantitative study of seeded micron-sized BAM:Eu^{2+} particles for gas-phase temperature measurements*, to be submitted to Applied Physics B - Lasers and Optics

B. Fond, C. Abram and F. Beyrau, *On the characterisation of tracer particles for thermographic particle image velocimetry*, Applied Physics B - Lasers and Optics, DOI 10.1007/s00340-014-5997-5 (2015) [110]

C. Abram, B. Fond and F. Beyrau, *High-precision flow temperature imaging using ZnO thermographic phosphor tracer particles*, 7th European Combustion Meeting, Budapest, Hungary (2015)

B. Fond, C. Abram and F. Beyrau, *Investigations of BAM:Eu as a tracer material for thermographic particle image velocimetry*, 7th European Combustion Meeting, Budapest, Hungary (2015)

C. Abram, B. Fond, A.L. Heyes and F. Beyrau, *High-speed thermographic particle image velocimetry*, 17th International Symposium on the Application of Laser Techniques to Fluid Mechanics, Lisbon, Portugal (2014)

B. Fond, C. Abram and F. Beyrau, *Characterisation of BAM:Eu^{2+} tracer particles for thermographic particle image velocimetry*, 17th International Symposium on the Application of Laser Techniques to Fluid Mechanics, Lisbon, Portugal (2014)

C. Abram, B. Fond, A.L. Heyes and F. Beyrau, *Experimental considerations for simultaneous gas-phase thermometry and velocimetry using thermographic phosphors*, 6th European Combustion Meeting, Lund, Sweden (2013)

B. Fond, C. Abram, A.L. Heyes, A.M. Kempf and F. Beyrau, *Use of thermographic phosphors for simultaneous velocity, temperature and mixture fraction imaging*, 6th European Combustion Meeting, Lund, Sweden (2013)

C. Abram, B. Fond, A.L. Heyes and F. Beyrau, *High-speed planar thermometry and velocimetry using thermographic phosphor particles*, Applied Physics B - Lasers and Optics, 111:155-160 (2013) [97]

B. Fond, C. Abram, A.L. Heyes, A.M. Kempf and F. Beyrau, *Simultaneous temperature, velocity and mixture fraction imaging in turbulent flows using thermographic phosphor tracer particles*, Optics Express, 20:22118-22133 (2012) [15]

B. Fond, C. Abram, A.L. Heyes, A.M. Kempf and F. Beyrau, *Thermographic phosphor particles as tracers for simultaneous vector-scalar measurements in turbulent flows*, 16th International Symposium on the Application of Laser Techniques to Fluid Mechanics, Lisbon, Portugal (2012)

Permission Documents

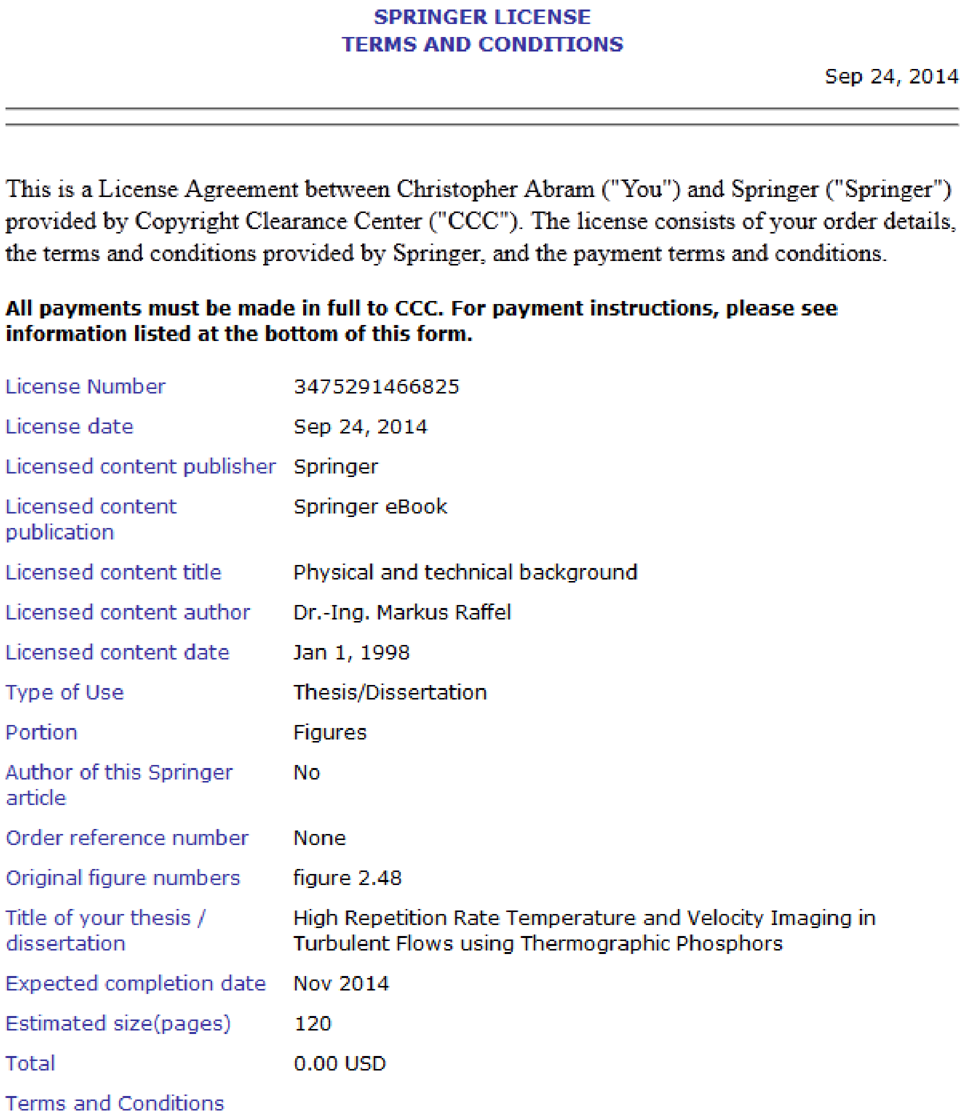

SPRINGER LICENSE
TERMS AND CONDITIONS

Sep 24, 2014

This is a License Agreement between Christopher Abram ("You") and Springer ("Springer") provided by Copyright Clearance Center ("CCC"). The license consists of your order details, the terms and conditions provided by Springer, and the payment terms and conditions.

All payments must be made in full to CCC. For payment instructions, please see information listed at the bottom of this form.

License Number	3475291466825
License date	Sep 24, 2014
Licensed content publisher	Springer
Licensed content publication	Springer eBook
Licensed content title	Physical and technical background
Licensed content author	Dr.-Ing. Markus Raffel
Licensed content date	Jan 1, 1998
Type of Use	Thesis/Dissertation
Portion	Figures
Author of this Springer article	No
Order reference number	None
Original figure numbers	figure 2.48
Title of your thesis / dissertation	High Repetition Rate Temperature and Velocity Imaging in Turbulent Flows using Thermographic Phosphors
Expected completion date	Nov 2014
Estimated size(pages)	120
Total	0.00 USD
Terms and Conditions	

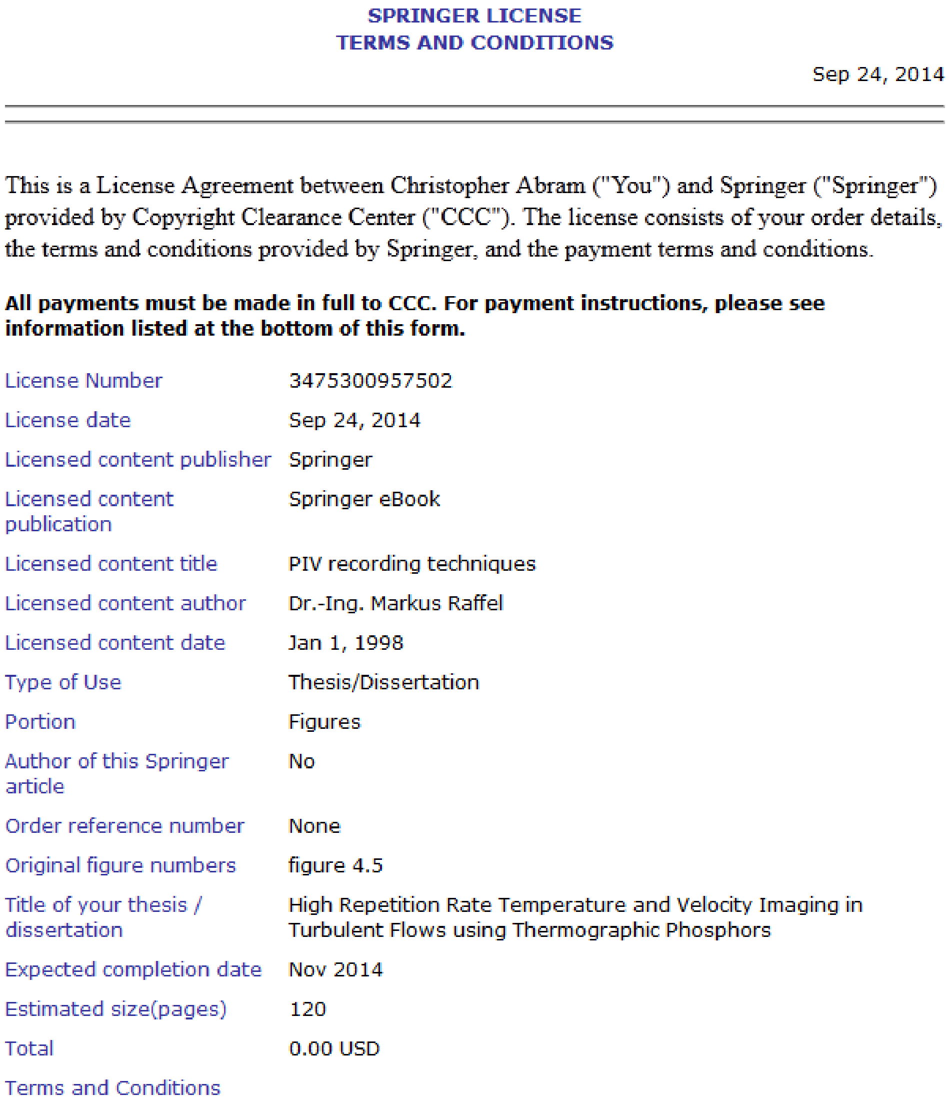

SPRINGER LICENSE
TERMS AND CONDITIONS

Sep 24, 2014

This is a License Agreement between Christopher Abram ("You") and Springer ("Springer") provided by Copyright Clearance Center ("CCC"). The license consists of your order details, the terms and conditions provided by Springer, and the payment terms and conditions.

All payments must be made in full to CCC. For payment instructions, please see information listed at the bottom of this form.

License Number	3475300957502
License date	Sep 24, 2014
Licensed content publisher	Springer
Licensed content publication	Springer eBook
Licensed content title	PIV recording techniques
Licensed content author	Dr.-Ing. Markus Raffel
Licensed content date	Jan 1, 1998
Type of Use	Thesis/Dissertation
Portion	Figures
Author of this Springer article	No
Order reference number	None
Original figure numbers	figure 4.5
Title of your thesis / dissertation	High Repetition Rate Temperature and Velocity Imaging in Turbulent Flows using Thermographic Phosphors
Expected completion date	Nov 2014
Estimated size(pages)	120
Total	0.00 USD
Terms and Conditions	

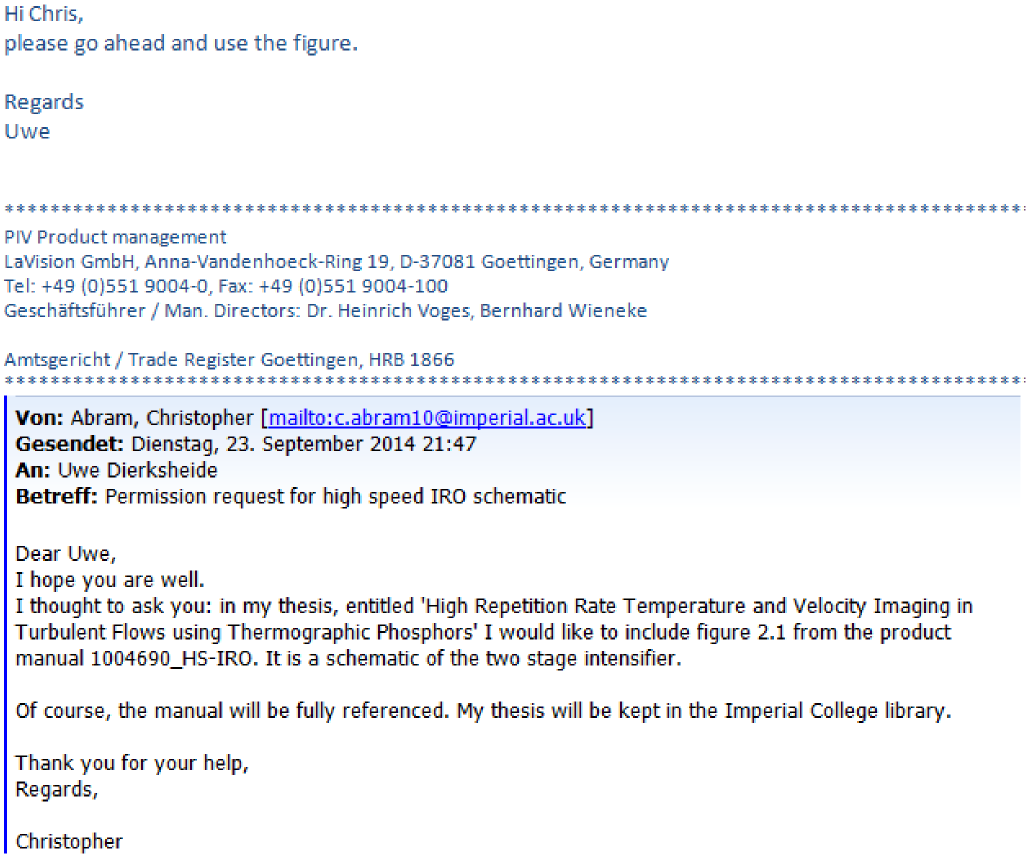

Hi Chris,
please go ahead and use the figure.

Regards
Uwe

****

PIV Product management
LaVision GmbH, Anna-Vandenhoeck-Ring 19, D-37081 Goettingen, Germany
Tel: +49 (0)551 9004-0, Fax: +49 (0)551 9004-100
Geschäftsführer / Man. Directors: Dr. Heinrich Voges, Bernhard Wieneke

Amtsgericht / Trade Register Goettingen, HRB 1866

****

Von: Abram, Christopher [mailto:c.abram10@imperial.ac.uk]
Gesendet: Dienstag, 23. September 2014 21:47
An: Uwe Dierksheide
Betreff: Permission request for high speed IRO schematic

Dear Uwe,
I hope you are well.
I thought to ask you: in my thesis, entitled 'High Repetition Rate Temperature and Velocity Imaging in Turbulent Flows using Thermographic Phosphors' I would like to include figure 2.1 from the product manual 1004690_HS-IRO. It is a schematic of the two stage intensifier.

Of course, the manual will be fully referenced. My thesis will be kept in the Imperial College library.

Thank you for your help,
Regards,

Christopher

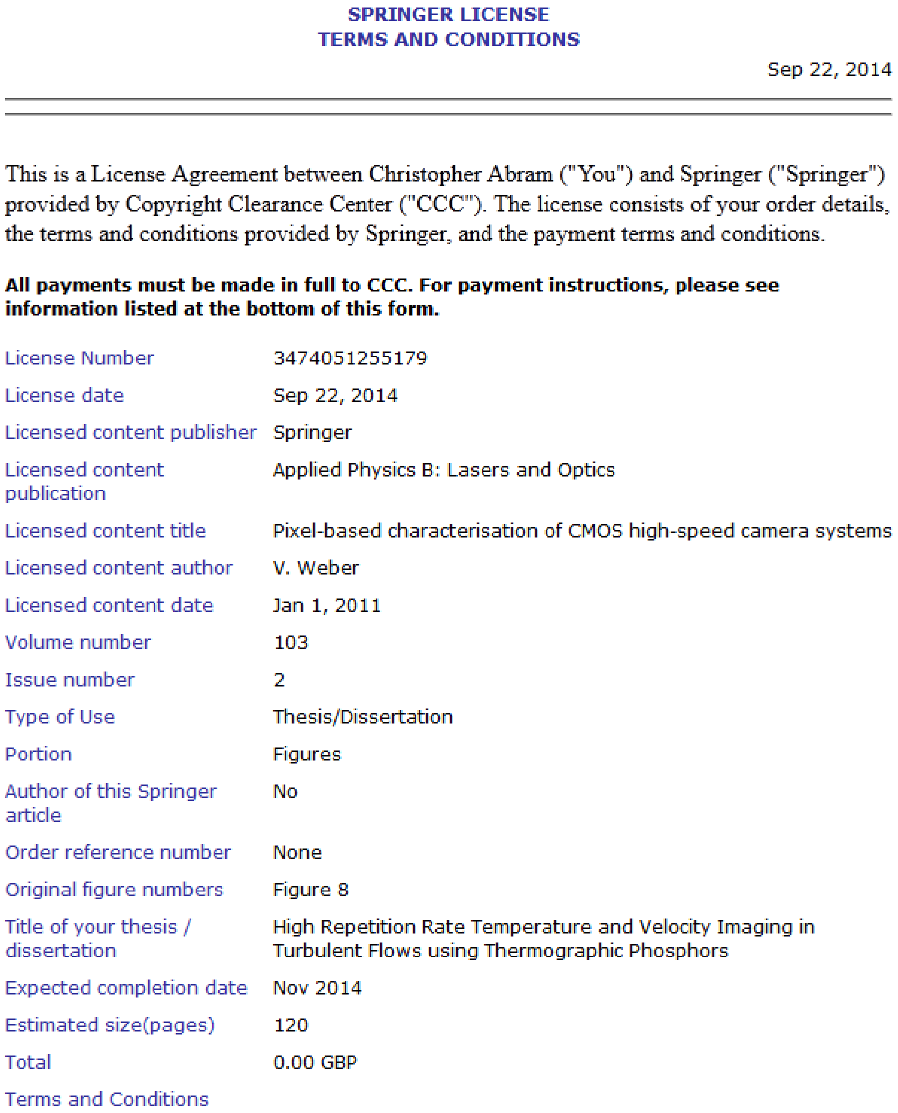

SPRINGER LICENSE
TERMS AND CONDITIONS

Sep 22, 2014

This is a License Agreement between Christopher Abram ("You") and Springer ("Springer") provided by Copyright Clearance Center ("CCC"). The license consists of your order details, the terms and conditions provided by Springer, and the payment terms and conditions.

All payments must be made in full to CCC. For payment instructions, please see information listed at the bottom of this form.

License Number	3474051255179
License date	Sep 22, 2014
Licensed content publisher	Springer
Licensed content publication	Applied Physics B: Lasers and Optics
Licensed content title	Pixel-based characterisation of CMOS high-speed camera systems
Licensed content author	V. Weber
Licensed content date	Jan 1, 2011
Volume number	103
Issue number	2
Type of Use	Thesis/Dissertation
Portion	Figures
Author of this Springer article	No
Order reference number	None
Original figure numbers	Figure 8
Title of your thesis / dissertation	High Repetition Rate Temperature and Velocity Imaging in Turbulent Flows using Thermographic Phosphors
Expected completion date	Nov 2014
Estimated size(pages)	120
Total	0.00 GBP
Terms and Conditions	

Three Park Avenue
New York, NY
10016-5990 U.S.A.
tel 1.212.591.7000
fax 1.212.591.7674
www.asme.org

ASME CONFERENCE/JOURNAL /BOOKS PUBLICATIONS PERMISSION REQUEST FORM:

Please be sure to fill out all in order to complete the form, then email the form to permissions@asme.org.

*Please type in all required text.

ASME Publication Title Conference/Journal/Book)*: Journal of Turbomachinery

Complete List of Authors*: Prasad Kalghatgi and Sumanta Acharya

Paper Title (Conference/Journal) *: Modal Analysis of Inclined Film Cooling Jet Flow

Paper Number Conference)*: 081007
Volume Number (Journal) *: 136
Indicate Page(s) in the ASME publication: 1-11
Year of Publication*: 2014
List Figure Numbers: 8
List Table Numbers: -
Number of Copies: -

Usage (Please check box): **Print** [✓ **Academic**] **Online** **Intranet**

Title of outside publication*: High Repetition Rate Temperature and Velocity Imaging in Turbulent Flows ising Thermographic Phosphors
Publisher*: Imperial College

Explanation of Usage: The figure will be included in the printed examination copy of my thesis and the electronic version uploaded on Imperial College's online repository. It will be made available to the public under a Creative Commons Attribution-Non-Commercial No Derivatives Licence

First Name*: Christopher
Last Name*: Abram
Address Line 1*: 139 Lansdowne Way

Address Line 2: Stockwell

City*: London
State*: London
Zip*: SW8 2NP
Phone: 0044 7776423373
Fax:
Email*: c.abram10@imperial.ac.uk